LEWIS-ACID BEHAVIOUR OF TUNGSTEN HEXAFLUORIDE TOWARDS MIXED LIGAND SYSTEMS, PHOSPHINE OXIDES AND TRIDENTATE TERPYRIDINE

TAYLOR PETER KARL ADAMITZ
Bachelor of Science, University of Lethbridge, 2022

A thesis submitted
in partial fulfilment of the requirements for the degree of

MASTER OF SCIENCE

in

CHEMISTRY

Department of Chemistry and Biochemistry
University of Lethbridge
LETHBRIDGE, ALBERTA, CANADA

LEWIS-ACID BEHAVIOR OF TUNGSTEN HEXAFLUORIDE TOWARDS MIXED LIGAND SYSTEMS, PHOSPHINE OXIDES AND TRIDENTATE TERPYRIDINE

TAYLOR PETER KARL ADAMITZ

Date of Defense: June 27th, 2024

Dr. Michael Gerken Thesis Supervisor	Professor	Ph. D.
Dr. Paul G. Hayes Thesis Examination Committee Member	Professor	Ph. D.
Dr. Jean-Denys Hamel Thesis Examination Committee Member	Assistant Professor	Ph. D.
Dr. René Boeré Chair, Thesis Examination Committee	Professor	Ph. D.

Abstract

The Lewis-acid behavior of WF_6 towards mixed ligand systems, phosphine oxides, and tridentate terpyridine has been investigated. Because of the known stability of 1 : 2 adducts of WF_6 with main-group-donor ligands, the reaction of WF_6 with stoichiometric amounts of the two bases pyridine and $P(CH_3)_3$ was studied, resulting in crystal growth of $WF_6(py)\{P(CH_3)_3\}\bullet CH_2Cl_2$. The $WF_6(py)\{P(CH_3)_3\}$ adduct adopts a capped trigonal prismatic geometry, prevalent for WF_6 adducts. However, alongside the presence of the desired adduct, numerous side products were identified by NMR spectroscopy. Reactions of WF_6 with $OP(C_2H_5)_3$ and $OP(C_6H_5)_3$ were conducted at both ambient temperatures and at –80 ºC invariably led to deoxofluorination with the formation of F_2PR_3 and $[FPR_3]^+$, R = C_2H_2, C_6H_5, being identified by NMR spectroscopy. Additionally, evidence for the new $WOF_4\{OP(C_2H_5)\}_2$ adduct was obtained by NMR spectroscopy. Lastly, the ability of WF_6 to relinquish a fluoride when stabilized by nitrogen bases, alongside its ability to act as a fluoride acceptor, has been exploited to yield the $[WF_5(terpy)][WF_7]$ salt as an autoionization product. This salt was fully characterized by multinuclear NMR and Raman spectroscopy, as well as X-ray crystallography and further studied computationally. The octacoordinated $[WF_5(terpy)]^+$ cation in $[WF_5(terpy)][WF_7]\bullet SO_2$ has a bicapped trigonal prismatic geometry as verified by the τ_8 geometry index. Tungsten hexafluoride in the $[WF_7]^-$ anion was displaced upon reacting the salt with $SbF_5\bullet SO_2$, yielding $[WF_5(terpy)][SbF_6]$.

Contribution of Authors

I am responsible for all of the experimental research reported herein. All computations, as well as the crystal selection and mounting of the $WF_6(py)\{P(CH_3)_3\}\bullet CH_2Cl_2$ crystal were carried out by Felix O'Donnell. I performed the analysis and interpretation of the computational data.

Acknowledgements

First and foremost, I would like to thank Prof. Michael Gerken, for his mentorship during my time as both an undergraduate and graduate student. His knowledge, patience, kindness, and enthusiasm have helped me grow as a student, chemist and as a person both inside and outside of the lab. I am ever grateful for the outings he has taken the group on which allowed me to gain a better appreciation of Lethbridge and the many other places we have been to together. Words cannot convey my gratitude.

I also thank my committee members, Assistant Prof. Jean-Denys Hamel, and Prof. Paul Hayes, for their advice and insight during my degree and for the small talk they provided during their oft busy schedule. I would also like to thank Prof. René Boeré for chairing my defense and generously sharing his knowledge of X-ray crystallography.

I would like to thank Mr. Vincent Weiler and Mr. Tony Montina for sharing their expertise in NMR spectroscopy and aid in solving many instrumental, and sometimes user, issues. I would also like to thank Mr. Kris Fischer for his invaluable help in providing custom glassware and repairing the labs' Pyrex vacuum lines.

I have had the honour and pleasure of working alongside numerous students during my time at the University of Lethbridge, some graduate and, at the time, undergraduate. I wish to thank Craig Sommer for his assistance in the lab, specifically with tungsten oxides, and listening to my speeches on our shared hobbies. I would also like to thank Miriam van Hoeve, being both contemporary and mentor in the lab, and her enduring optimism during my research. I would also like to thank Nathan Hill and Nolan Hahn for being my instructors during my undergrad, for engaging in philosophical debates, and the many

lessons learned during late night gaming. I'd also like to thank Stacie Nelson and Taylor Semeniuk for their advice related to organic chemistry, the hockey nights we have shared together, and their aid in bolstering my confidence. I'd also like to thank the German exchange students Merlin Bohn, Malte Herfurth, and Bastian Steinert for their camaraderie and showing me parts of their culture. Furthermore, I'd like to thank Makay Murray, Daisy Cruiz-Milette, Sam Dresher, Shaune Palidwar, and the countless other students I had the pleasure of working beside for their comradery during my studies. Lastly, I acknowledge Felix O'Donnell for being an amazing mentor both in the lab and in my personal life, for answering my endless questions as an undergraduate, providing me the computational data used in this thesis, and trouble shooting during my research. Also for enduring my quirks, as well as tirades and speeches on numerous topics, shared music, and provided sincere advice that helped to shape me as a person.

Finally, I would like to thank my parents Paulla Anne Adamitz, St. Sgt. Lorne Herman Adamitz, and my sister Sahara Elizabeth Adamitz for their love, confidence and support of me and my work. I would not be here nor who I am without any of you – I thank you for being there for me during both the tough times and the good times.

I love you all.

Table of Contents

Chapter 1. Introduction. 1

1.1. Transition-Metal Hexafluorides. 1
1.2. Synthesis and Properties. 1
1.3. Lewis Acid Chemistry. 5
1.3.1. Neutral Adducts. 5
1.3.2. Ionic Derivatives of WF_6. 7
1.4. Ligand Substitution Chemistry. 10
1.5. Objectives and Impact of Research. 16
1.6. References. 18

Chapter 2. Experimental. 31

2.1. General Methods. 31
2.1.1. Standard Techniques. 31
2.1.2. Raman Spectroscopy. 38
2.1.3. NMR Spectroscopy. 40
2.1.4. X-ray Crystallography. 40
2.1.4.1. Crystal Growth and Mounting. 40
2.1.4.2. Data Collection and Reduction. 43
2.1.4.3. Structure Solution and Refinement. 44
2.2. Preparation and Purification of Reagents. 45
2.2.1. Fluorine and Binary Fluorides. 45
2.2.2. Common Solvents. 45
2.2.3. Volatile Bases. 46
2.2.4. Solid Bases. 46
2.2.5. Main-Group and Transition Metal Fluoride Adducts. 46
2.3. Synthesis and Crystal Growth. 46
2.3.1. Lewis Acid Behaviour of WF_6 Towards Mixed Ligand Systems. 46
2.3.1.1. Reaction of $WF_6(NC_5H_5)$ with $P(CH_3)_3$ in CH_2Cl_2. . . . 46
2.3.1.2. $WF_6(NC_5H_5)\{P(CH_3)_3\}\bullet CH_2Cl_2$ Crystal Growth. 47
2.3.2. Exploration of Phosphine Oxides as Ligands to WF_6. 47
2.3.2.1. Reaction of WF_6 with $OP(C_2H_5)$ in CH_2Cl_2. 47
2.3.2.2. Reaction of WF_6 with $OP(C_6H_5)$ in CH_3CN. 48
2.3.2.3. $F_2P(C_6H_5)$ Crystal Growth. 48
2.3.3. Lewis Acidity of WF_6 Towards Tridentate Terpyridine. 48
2.3.3.1. $[WF_5(terpy)][WF_7]$ 48
2.3.3.2. $[WF_5(terpy)][WF_7]\bullet SO_2$ Crystal Growth. 49
2.3.3.3. $[WF_5(terpy)][SbF_6]$ 50
2.4. Computational Methods. 51
2.5. References. 52

Chapter 3. Lewis-Acid Behaviour of WF_6 Towards Mixed Ligand Systems. 54

3.1. Introduction. 54
3.2. Results and Discussion. 55
3.2.1. Syntheses and Properties of $WF_6(py)\{P(CH_3)_3\}$. 55
3.2.2. X-Ray Crystal Structure of $WF_6(py)\{P(CH_3)_3\}\bullet CH_2Cl_2$. 57
3.2.3. Multinuclear NMR Spectroscopy. 60
3.2.4. Raman Spectrometry. 70
3.2.5. Computational Results. 76
3.3. Conclusions. 79
3.4. References. 81

Chapter 4. Exploration of Phosphine Oxides as Ligands to WF_6. 83

4.1. Introduction. 83
4.2. Results and Discussion. 84
4.2.1. Synthesis. 84
4.2.2. Multinuclear NMR Spectroscopy. 86
4.2.3. X-ray Crystallography. 100
4.3. Conclusions. 103
4.4. References. 104

Chapter 5. Lewis Acidity of WF_6 Towards Tridentate Terpyridine. 106

5.1. Introduction. 106
5.2. Results and Discussion. 108
5.2.1. Synthesis and Properties of $[WF_5(terpy)][WF_7]$ and $[WF_5(terpy)][SbF_6]$. 108
5.2.2. Crystal Structure of $[WF_5(terpy)][WF_7]\cdot SO_2$. 109
5.2.3. Raman Spectroscopy of $[WF_5(terpy)][X]$ ($X = WF_7, SbF_6$). 114
5.2.4. Multinuclear NMR Spectrometry of $[WF_5(terpy)][WF_7]$. 120
5.2.5. Computational Analysis. 130
5.3. Conclusion. 132
5.4. References. 133

Chapter 6. Conclusions and Future Work. 136

6.1. Conclusions. 136
6.2. Future Work. 138
6.3. References. 141

List of Tables

Table 1.1. Selected Physical and Chemical Properties of the Transition-Metal Hexafluorides. 3

Table 2.1. Elucidated crystal structures with their corresponding internal code. 45

Table 3.1. Crystallographic Data Collection and Refinement Parameters for $WF_6(py)\{P(CH_3)_3\}\bullet CH_2Cl_2$. 58

Table 3.2. Experimental and Calculated[a] [given in square brackets] Bond Lengths (Å) and Angles (º) of Select Fluoridotungsten(VI) Complexes. 60

Table 3.3. Calculated Vibrational Frequencies (cm^{-1}) of $WF_6(py)\{P(CH_3)_3\}$ and Experimental Raman Frequencies for the orange solid recover from the addition of $P(CH_3)_3$ to $WF_6(py)$. 72

Table 3.4. Natural–Population–Analysis Charges of Select Fluoridotungsten(VI) Complexes[a]. 77

Table 3.5. Wiberg Bond Indices of Various Select Fluoridotungsten(VI) Complexes[a]. . 78

Table 4.1. Crystallographic Data Collection and Refinement Parameters for $F_2P(C_5H_6)_3$. 101

Table 5.1. Crystallographic Data Collection and Refinement Parameters for $[WF_5(terpy)][WF_7]\bullet SO_2$. 110

Table 5.2. Selected experimental and Calculated Bond Lengths [given in square brackets] in (Å) and Angles (º) of $[WF_5(terpy)][WF_7]\bullet SO_2$. 111

Table 5.3. Ranges of select experimental bond lengths of various W(VI) fluorido species with pyridine-based ligands. 113

Table 5.4. Observed Raman and calculated vibrational frequencies (cm^{-1}) of free terpy and $[WF_5(terpy)][X]$ (X = WF_7, SbF_6). 116

Table 5.5. Natural-Population-Analysis Charges and Wiberg Valences of Select Cationic Fluoridotungsten(VI) Complexes. 131

Table 5.6. Wiberg Bond Indices of Various Select Fluoridotungsten(VI) Complexes. . 131

List of Figures

Figure 2.1. A 316-stainless steel (Swagelok SS-1KF2) valve with a flared ¼”-o.d. FEP tube with nut and sleeve (top) and equipment used to fuse thick-walled ¼” to 4-mm FEP and create the flare (bottom). 32

Figure 2.2. Pyrex vacuum line attached to a liquid-N_2-cooled (–196 ºC) Pyrex (top). Schematic of the vacuum line adapted from Jared Nieboer’s M.Sc. thesis (2007, University of Lethbridge, bottom). 34

Figure 2.3. Ultra-Torr vacuum fittings (Swagelok) (top) PTFE vacuum fittings (Swagelok) (bottom) partially disassembled. 35

Figure 2.4. Nickel/316-stainless-steel (Autoclave Engineers) vacuum line, equipped with absolute capacitance manometers (MKS Baratron, type 626, 0–10 or 0–1000 Torr)(top). Schematic of the vacuum line adapted from Jared Nieboer’s M.Sc. thesis (2007, University of Lethbridge, bottom). 36

Figure 2.5. OmniLab, Vacuum Atmospheres dry box filled with N_2 atmosphere and equipped with cold well filled with Cu BBs. 37

Figure 2.6. Thermo NESLAB, CC-100 cryopump (left) and attached C_2H_5OH bath (right). 38

Figure 2.7. Bruker RFS-100 Raman spectrometer outfitted with a quartz beam splitter and liquid-N_2 cooled germanium detector. 39

Figure 2.8. The 10.5-L Dewar is equipped with a glass N_2 inlet, mirrored-glass Dewar sleeve, and aluminium trough (top). Schematic of the low-temperature crystal-mounting apparatus adapted from Jared Nieboer’s M.Sc. thesis (2007, University of Lethbridge) . 42

Figure 2.9. Rigaku SuperNova diffractometer equipped with a Dectris Pilatus 3R 200K-A hybrid-pixel-array detector, a four-circle κ goniometer, an Oxford Cryostream 800, and sealed MoKα and CuKα X-ray sources. 44

Figure 2.10. Numeric classification of proton (left) and carbon (right) for terpy. 49

Figure 3.1. Thermal ellipsoid plots (50% probability level) of $WF_6(py)\{P(CH_3)_3\}\bullet CH_2Cl_2$. 59

Figure 3.2. ^{19}F NMR spectrum of the isolated products from the reaction of $WF_6(py)$ + $P(CH_3)_3$, dissolved in CH_3CN at 22 °C. The asterisk (*) denotes a trace amount of $WOF_4(py)$. 61

Figure 3.3. ^{19}F NMR spectrum of the isolated products from the reaction of $WF_6(py)$ + $P(CH_3)_3$, dissolved in CH_3CN at –35 °C. # and * denote trace amounts of $WOF_4\{P(CH_3)_3\}$ and $WOF_4(py)$, respectively. 64

Figure 3.4. $^{31}P\{^{1}H\}$ NMR spectrum of the isolated products from the reaction of $WF_6(py)$ + $P(CH_3)_3$, dissolved in CH_3CN at –35 °C. 64

Figure 3.5. ^{19}F NMR spectrum of the reaction mixture of $WF_6(py)$ + $P(CH_3)_3$ in CH_2Cl_2 at –40 °C. 67

Figure 3.6. Raman spectrum of the orange solid recovered from the addition of $P(CH_3)_3$ to $WF_6(py)$, recorded at ambient temperature in an FEP sample tube. Asterisks (*) denote FEP bands. 71

Figure 3.7. Raman spectrum of the brown-orange solid, recorded at ambient temperature in a glass m.p. capillary. 76

Figure 4.1. ^{1}H NMR spectrum of the isolated products from the reaction of WF_6 + $OP(C_6H_5)_3$, dissolved in CH_2Cl_2 at 22 °C. 87

Figure 4.2. ^{19}F NMR spectrum of the isolated products from the reaction of WF_6 + $OP(C_6H_5)_3$, dissolved in CH_2Cl_2 at 22 °C. 87

Figure 4.3. $^{31}P\{^{1}H\}$ NMR spectrum of the isolated products from the reaction of WF_6 + $OP(C_6H_5)_3$, dissolved in CH_2Cl_2 at 22 °C. 88

Figure 4.4. ^{19}F NMR spectrum of the isolated products from the reaction of WF_6 + $OP(C_6H_5)_3$, dissolved in CH_2Cl_2 at 22 °C after leaving the solution for 2 days at ambient temperatures. 89

Figure 4.5. ^{1}H NMR spectrum of the isolated products from the reaction of WF_6 + $OP(C_2H_5)_3$, dissolved in CH_2Cl_2 at 22 °C. Asterisk (*) denotes traces of ethanol on the outside of the sample tube. 92

Figure 4.6. ^{19}F NMR spectrum of the isolated products from the reaction of WF_6 + $OP(C_2H_5)_3$, dissolved in CH_2Cl_2 at 22 °C. 92

Figure 4.7. $^{31}P\{^{1}H\}$ NMR spectrum of the isolated products from the reaction of WF_6 + $OP(C_2H_5)_3$, dissolved in CH_2Cl_2 at 22 °C. 93

Figure 4.8. ^{1}H NMR spectrum of the reaction of WF_6 with $OP(C_6H_5)_3$ in CH_2Cl_2 at –80 °C. 94

Figure 4.9. ^{19}F NMR spectrum of the products from the reaction of WF_6 with $OP(C_6H_5)_3$ in CH_2Cl_2 at –80 °C. 95

Figure 4.10. $^{31}P\{^{1}H\}$ NMR spectrum of the products from the reaction of WF_6 with $OP(C_6H_5)_3$ in CH_2Cl_2 at –80 °C. 95

Figure 4.11. ^{1}H NMR spectrum of the reaction of WF_6 with $OP(C_2H_5)_3$ in CH_2Cl_2 at –80 °C. The asterisk (*) denotes traces of ethanol on the outside of the sample tube. 97

Figure 4.12. ^{19}F NMR spectrum of the reaction of WF_6 with $OP(C_2H_5)_3$ in CH_2Cl_2 at –80 °C. 98

Figure 4.13. Fluorine-19 resonances assigned to the proposed $WOF_4\{OP(C_2H_5)_3\}_2$ adduct in the ^{19}F NMR spectrum of WF_6 with $OP(C_2H_5)_3$ in CH_2Cl_2 at –80 °C. 99

Figure 4.14. Lewis diagram of the proposed $WOF_4\{OP(C_2H_5)_3\}_2$ adduct. 99

Figure 4.15. $^{31}P\{^1H\}$ NMR spectrum of the products from the reaction of WF_6 with $OP(C_2H_5)_3$ in CH_2Cl_2 at –80 °C. 100

Figure 4.16. Thermal ellipsoid plot (50% probability level) of $F_2P(C_5H_6)_3$. 101

Figure 4.17. Crystal packing diagram of $F_2P(C_6H_5)_3$ viewed down the *a* axis. 102

Figure 5.1. Thermal ellipsoid plot (50% probability level) hydrogens omitted for clarity (left) of the asymmetric unit of $[WF_5(terpy)][WF_7]\bullet SO_2$ and B3LYP/def2-TZVPPD optimized gas-phase structure of $[WF_5(terpy)]^+$ (right). 110

Figure 5.2 Raman spectrum of $[WF_5(terpy)][WF_7]$ at ambient temperature. FEP bands (*) observed at 735 and 385 cm^{-1} and $[WF_7]^-$ band (†) is observed at 705 cm^{-1}. 115

Figure 5.3 Raman spectrum of $[WF_5(terpy)][SbF_6]$ at ambient temperature. FEP bands (*) observed at 1380, 735 and 385 cm^{-1} $[SbF_6]^-$ band (†) are observed at 645, 573 and 280 cm^{-1}. 115

Figure 5.4. Numeric classification of proton (left) and carbon (right) for terpy. 121

Figure 5.5. ^1H NMR spectrum of free terpy at 22 °C in acetonitrile. 122

Figure 5.6. $^{13}C\{^1H\}$ NMR spectrum of free terpy at –35 °C in acetonitrile. 122

Figure 5.7. ^1H NMR spectrum of $[WF_5(terpy)][WF_7]$ at 22 °C in SO_2. 124

Figure 5.8. $^{13}C\{^1H\}$ NMR spectrum of $[WF_5(terpy)][WF_7]$ at 22 °C in SO_2. 124

Figure 5.9. ^{19}F NMR spectrum of $[WF_5(terpy)][WF_7]$ at 22 °C in SO_2. 125

Figure 5.10. ^{19}F NMR spectrum of $[WF_5(terpy)][WF_7]$ at –60 °C in SO_2. 126

Figure 5.11. ^{19}F NMR spectrum of $[WF_5(terpy)][SbF_6]$ at 22 °C in SO_2. 127

Figure 5.12. ^1H NMR spectrum of $[WF_5(terpy)][SbF_6]$ at 22 °C in SO_2. Asterisks (*) denote traces of $[Hterpy]^+$. 128

Figure 5.13. $^{13}C\{^1H\}$ NMR spectrum of $[WF_5(terpy)][SbF_6]$ at –35 °C in SO_2. Asterisks (*) denote traces of $[Hterpy]^+$. 128

Figure 5.14. ^{19}F NMR spectrum of $2WF_6(py)$ + terpy at 22 °C in SO_2. 129

Figure 5.15. ^{19}F NMR spectrum of $[WF_5(terpy)][WF_7]$ at 22 °C in py. 130

Figure 6.1. 1,4,7-trimethyl-1,4,7-triazacyclononane (Me_3TACN). 139

Figure 6.2. Quaterpyridine (qupy). 139

List of Abbreviations

General

Å	angstrom
aHF	anhydrous hydrogen fluoride
ax.	axial
BB	ball bearing
BCU	bay control unit
b.p.	boiling point
br.	bridging
BBFO	broad band fluorine observe
cm	centimeter
DFT	density functional theory
E_{ea}	electron affinity
E½	half-wave potential
Eq.	equation
eq.	equatorial
FEP	tetrafluoroethene-hexafluoropropene copolymer
FIA	fluoride-ion affinity
GPa	gigapascal
IR	infrared
Kel-F	poly(chlorotrifluoroethene)
kJ	kilojoule
LT	low temperature
m.p.	melting point
mer	meridional
mm	millimetre
mmol	millimole
mW	milliwatt
NBO	natural bond orbital

NPA	Natural Population Analysis
Nd:YAG	neodymium-doped yttrium aluminum garnet
o.d.	outer diameter
ref.	reference
term.	terminal
UV/Vis	ultraviolet-visible light
WBI	Wiberg bond index
°C	degree Celsius
σ	standard deviation
θ	dihedral angle
″	inch
π	pi

Ligands

bipy	2,2′-bipyridine
Cp	η^5-cyclopentadienyl
Cp*	η^5-pentamethylcyclopentadienyl
Et	Ethyl
F-py	2-fluoropyridine
Ph	Phenyl
phen	1,10-phenanthroline
py	pyridine
terpy	2,2′:6′,2″-terpyridine

NMR Spectroscopy

br d	broad doublet
d	doublet
dd	doublet of doublets
ddd	doublet of doublets of doublets
dt	doublet of triplets
Hz	hertz
J	scalar coupling constant

m	multiplet
NMR	nuclear magnetic resonance
ppm	part per million
q	quartet
qn	quintet
s	singlet
sept	septet
t	triplet
td	triplet of doublets
δ	chemical shift
$\Delta\nu_{½}$	width at half height of the peak in Hz

X-ray Crystallography

a, *b*, *c*, *α*, *β*, *γ*	cell dimensions
F(000)	electrons per unit cell
GooF	goodness of fit
R_1	R-factor (agreement index)
T	temperature
V	cell volume
wR_2	weighted R-factor
Z	number of molecules per unit cell
λ	wavelength
μ	absorption coefficient
ρ_{calc}	calculated density

Chapter 1 – Introduction

1.1. Transition-Metal Hexafluorides

Currently, the syntheses of nine transition-metal hexafluorides MF_6 (M = Mo, W, Tc, Re, Ru, Os, Rh, Ir, and Pt) have been confirmed, which represent a unique class of compounds with the metal centre in the +6 oxidation state. The electron-withdrawing nature of the fluorido ligand results in these compounds being highly Lewis-acidic as well as strong oxidizers. This in turn allows for the fundamental exploration of these metal centres at elevated oxidation states, particularly noteworthy for the group 9-10 hexafluorides where this oxidation state is rather uncommon. Despite possessing similar physical properties, these compounds display a large variance in chemical properties.[1-2] While hexafluorides of the later groups 8-10 have displayed immense oxidizing behavior, the oxidizing capabilities of the early transition metal hexafluorides are significantly weaker in comparison. This has allowed for the exploration of adduct formation and ligand-substitution chemistry particularly with WF_6 as will be discussed in this chapter.

1.2 Synthesis and Properties

The first metal hexafluoride to be synthesized was MoF_6 in 1907 by Ruff and Eisner and was prepared by subjecting the metal to a stream of elemental fluorine gas. In addition, WF_6 was later isolated in a similar manner, however, synthesizing IrF_6 and OsF_6 required additional heating in an autoclave.[1] PtF_6 was synthesised by Weinstock *et al.* in 1957. Unlike its predecessors, this synthesis required passing an electrical current through a platinum wire in the presence of 300 Torr of F_2 surrounded by a surface cooled by liquid nitrogen.[3] Later, Malm *et al.* were able to produce ReF_6 by subjecting the metal to

elemental fluorine at elevated temperatures.[4] However, due to the process also generating ReF_7, there is doubt if this could be classified as the first isolation of the compound. Lastly, TcF_6, RuF_6, and RhF_6 were finally isolated by Claassen *et al.* in 1961. The first of these three metal hexafluorides was synthesised in an autoclave akin to the Ir and Os analogues, however, the latter two have various routes of synthesis ranging from the method used to generate PtF_6, to the fluorination of their pentafluoro variants at elevated temperatures.[5-7] Advancements are still ongoing in the field with Kraus *et al.* reporting an alternate synthetic route to MF_6 (M = Ru, Rh, Pt). Herein, the group reacted the respective metal powders in a fluorine plasma with NF_3 as the feed gas under argon atmosphere by utilizing a laser as a heat source (Eq. 1.1). While the MF_6 species were generally obtained in high yields, further optimization is required as lower metal fluorides or species stemming from decomposition of organic components where detected.[8]

$$M + 2NF_3 \rightarrow MF_6 + N_2, \quad (M = Ru, Rh, Pt) \tag{1.1}$$

The first-row transition metals have been explored as preparative targets to expand the available metal hexafluorides. However, due to their instability and proposed oxidative strengths, they have been met with their own challenges. Glemser *et al.* reported to have synthesized CrF_6 in 1963 using an autoclave and F_2 gas.[9] However, subsequent attempts at synthesis have been unable to recreate the compound even under matrix conditions.[1,10] Recently, computational studies by Yang *et al.* have suggested a possible synthetic route to MF_6 (M = Cr, Mn, Fe) alongside other unreported lower metal fluorides using extreme pressure (300 GPa) to stabilize these compounds.[11] The synthesis of PdF_6 was attempted by Riedel *et al.* under matrix isolation, but the group was unable to conclusively determine if the compound was formed.[11] To date, no successful attempts at preparing AuF_6 have

been reported, however, computations by Yang *et al.* have predicted a possible route via the compression of AuF_5 with fluorine gas at extreme pressures (300 GPa).[13] It is believed that these hexafluorides would be extremely unstable and aggressive if synthesised, surpassing the reactivity of PtF_6.[1,14-16]

As mentioned above, the transition metal hexafluorides display similar physical properties (Table 1.1). The W–F bond lengths, for instance, are similar across their respective row with slight elongations present in the group 9 and 10 transition metals attributed to the more populated t_{2g} orbitals.[17] Another similarity of these compounds is their geometries at both lower and higher temperatures. X-ray crystallography of the compounds revealed octahedral geometries with an ordered orthorhombic crystal phase at lower temperatures, changing to a disordered liquid-crystalline cubic phase past 0 °C.[2,18-19] Counterintuitively, both the melting and boiling points of these compounds decrease going from the second to third row as well as across a given row. Furthermore, the unit cell of the transition metal hexafluorides also decreases across a given row.[18] As such, it has been posited that the later transition metals must have stronger F···F interactions to account for this phenomenon.[2]

Table 1.1. Selected Physical and Chemical Properties of the Transition Metal Hexafluorides.

	MoF_6	TcF_6	RuF_6	RhF_6	
Configuration	[Kr]$4f^{14}$	[Kr]$4f^{14}4d^1$	[Kr]$4f^{14}4d^2$	[Kr]$4f^{14}4d^3$	
m.p. (°C)[a]	17.4	37.4	54.0	70.0	
b.p. (°C)[a]	35.0	55.3	~70	~70	
M–F_{av} (Å)[a]	1.813	1.812	1.816	1.821	
FIA (kJ/mol)[b]	310 [82]	320 [232]	347 [366]	264 [316]	
E_{ea} (eV)[b]	4.23	5.89	7.01	6.80	
	WF_6	ReF_6	OsF_6	IrF_6	PtF_6
Configuration	[Xe]$4f^{14}$	[Xe]$4f^{14}5d^1$	[Xe]$4f^{14}5d^2$	[Xe]$4f^{14}5d^3$	[Xe]$4f^{14}5d^4$
m.p. (°C)[a]	1.9	18.5	33.2	44.4	61.3
b.p. (°C)[a]	17.5	33.7	45.9	53.0	69.1
M–F_{av} (Å)[a]	1.823	1.824	1.825	1.835	1.845
FIA (kJ/mol)[c]	350 [–33]	338 [112]	345 [262]	293 [132]	331 [353]
E_{ea} (eV)[c]	3.16	4.58	5.92	5.99	7.09

[a] From reference 1. [b] From reference 18. [c] From reference 14. Square brackets denote the fluoride ion affinity (FIA) of the compounds under "non-classical" formation obtained from reference 19.

Despite the physical similarities, the transition metal hexafluorides display vastly different chemical properties. Some of these compounds are calculated to be immense oxidizing agents with E_{ea} values rivalling or surpassing that of F_2 (Table 1.1).[14,18,22] PtF_6 is undoubtedly the strongest oxidizing agent capable of oxidizing NOF and NO_2F to form $[NO]^+$ and $[NO_2]^+$ salt and releasing F_2.[23] Indeed, very few compounds are known to be stronger oxidizers with $[KrF]^+$, solutions of AgF_3 or NiF_4 being among them.[24-26] PtF_6 is also capable of oxidizing both Xe to $[XeF]^+$ and O_2 to $[O_2]^+$, with the former being instrumental in establishing the field of noble-gas chemistry.[27-28] RuF_6 and RhF_6 have both been calculated to be of similar oxidation strength to PtF_6, with $[O_2][MF_6]$ (M = Ru, Rh) salts also being obtained.[18,30] IrF_6 has also been shown to oxidize Xe, however better yields are obtained using HF and SbF_5, as well as to oxidize Cl_2 to $[Cl_4]^+$.[31-32] In contrast, there has been no report of the other transition metal hexafluoride oxidizing O_2. Despite having a similar calculated electron affinity, OsF_6 has not been shown to oxidize either Xe

or Cl_2 but has been shown to oxidize Br_2.[31,33] Meanwhile, the chemistry of TcF_6 has not been extensively investigated, presumably due its radioactivity.

Rhenium, molybdenum and tungsten hexafluoride are comparatively much weaker oxidizing agents, with the latter two species being incapable of oxidizing bromine and no literature surrounding that of the former.(34) Reactions with I_2 have resulted in reversible oxidation with ReF_6 in IF_5, however, with the addition of WF_6, the reaction no longer proceeds.(35) Meanwhile, MoF_6 is also capable of oxidizing I_2 in acetonitrile, forming a $[I(NCCH_3)_2]^+$ salt.(36) WF_6, meanwhile, has been shown to be capable of oxidizing a variety of metallocenes.(37-40) Nevertheless, this metal hexafluoride is considered to be the weakest oxidizing agent due to its inability to oxidize either NO or Si.(23,41)

1.3 Lewis Acid Chemistry

1.3.1 Neutral Adducts

Due to the weak oxidizing capabilities of WF_6, numerous derivatives with organic Lewis bases have been characterized and/or isolated. Tebbe and Muetterties were the first to isolate and characterize $WF_6\{N(CH_3)_3\}$, $WF_6\{P(CH_3)_3\}$, as well as $WF_6(py)_n$ (py = pyridine, n = 1,2) in 1968 by their chemical shifts. The ^{19}F NMR spectra of these species revealed broad resonances due to rapid exchange of the fluorine environments and separate signals could not be fully resolved at lower temperatures.(42) The ^{19}F NMR spectrum of $WF_6\{P(CH_3)_3\}$, however, showed a doublet splitting due to the $^2J_{F\text{-}P}$ coupling. Similarly, the adducts of $WF_6\{S(CH_3)_2\}_n$ (n = 1,2) have been reported by Steigel and Brownstein in 1974, with these compounds having been characterized by low-temperature ^{19}F NMR spectroscopy. The 1 : 1 adduct of $WF_6\{S(CH_3)_2\}$ was found to have a broad resonance at

160 ppm at –75 °C with the compound being insoluble in CH_2CHCl at lower temperatures. The 1 : 2 adduct $WF_6\{S(CH_3)_2\}_2$, meanwhile, showed resolved fluorine environments at –160 °C with a triplet at 118.4 ppm and a quintet at 36.8 ppm, consistent with a bicapped trigonal prismatic geometry (although not stated in the paper), which is in agreement with other WF_6L_2 adducts.[43] In 1992, Bougon *et al.* were able to isolate and characterize WF_6(F-py) (F-py = 2-fluoropyridine) by X-ray crystallography, showing a monocapped trigonal prismatic geometry. The group also prepared WF_6(bipy) (bipy = 2,2′-bipyridine) which was characterized by Raman and IR spectroscopy.[44-45] The group was able to obtain the crystal structure of $WF_6(py)_2$ in 1995, determining the structure to possess a bicapped trigonal prismatic geometry.[46] Crystal structures of WF_6(L) adducts with substituted pyridines (L = 4-NC_5H_4R, R = H, CH_3, $N(CH_3)_2$) were obtained by Gerken *et al.* in 2018 and were uniformly found to adopt monocapped trigonal prismatic geometries. Computational studies of these compounds, alongside the 2-NC_5H_4F adduct, revealed that the monocapped trigonal prismatic geometry is the minimum-energy structure in the gas phase.[47] Finally, Levason *et al.* were able to isolate $WF_6\{As(R)_3\}$ (R = CH_3, CH_2CH_3) characterizing them with IR, UV/Vis and multinuclear NMR spectroscopy.[48]

Meanwhile, back in 2010, Seppelt *et al.* were able to isolate and characterize $WF_6\{P(C_6H_5)(CH_3)_2\}$ as well as obtaining its crystal structure alongside $WF_6\{P(CH_3)_3\}$. While the latter retained the capped trigonal prismatic geometry observed for other adducts, the former adduct was shown to adopt a capped octahedral geometry.[49] These findings provided experimental proof to the initial claims that predict different hepta-coordinate geometries (monocapped octahedron, monocapped trigonal prism, and pentagonal bipyramid) to be similar in energy and validate previous computational findings conducted

with $[XF_7]^-$ (X = W, Mo, Xe, I, Te, Xe) anions.[50-51] In a similar manner, octa-coordinate species can adopt three high-symmetry geometries, *i.e.*, the square antiprismatic, bicapped trigonal prismatic or trigonal dodecahedral geometries. Careful control of stoichiometry allowed for the isolation of neutral $WF_6(L)$ (L = 1,10-phenanthroline (phen), bipy). While these compounds were insoluble in all attempted solvents, computational studies found that they possess distorted trigonal dodecahedral geometries as opposed to the observed bicapped trigonal prismatic geometry of $WF_6(py)_2$, further supporting the above claim.[44,52]

1.3.2 Ionic Derivatives of WF_6

As alluded above, another difference separating the group 6-7 hexafluorides from those of the later transition metal hexafluorides is the capability of forming $[MF_7]^-$ and $[MF_8]^{2-}$ complex fluorido metallate anions.[1] Ab initio studies where performed on the later $[MF_7]^-$ (M = Ru, Rh, Pt) anions and showed that they possess non-classical structures, consisting of an octahedral $[MF_6]^-$ anion with a weak F–F interaction to a F atom outside of the metal coordination sphere.[14,18] This geometry is in contrast to classical hepta-coordinate $[MF_7]^-$ anions and was shown to be unstable, being prone to decomposition forming $[MF_6]^-$ and a fluorine radical (Eq 1.2).[14,18]

$$[MF_7]^- \rightarrow [MF_6]^- + F \qquad \text{(Eq 1.2)}$$

The non-classical structure has been postulated to be either a result of the lower charge of the metal centres or their partially filled *d* orbitals inhibiting M–F bond formation.[1] $[MF_7]^-$ (M = Mo, W, Re) salts can be obtained by the direct reaction of the respective hexafluoride with RbF or CsF.[53-55] Crystallographic studies of these anions show that the $[Cs][MF_7]$ (M = Mo, W) salts contain ideal monocapped octahedral anions,

whereas the $[ReF_7]^-$ anion possesses a distorted pentagonal bipyramidal geometry.[56-57] Meanwhile, the $[MF_8]^{2-}$ salts can be obtained from the pyrolysis of the respective $[MF_7]^-$ anion.[57-58] Crystallographic studies of these $[MF_8]^{2-}$ (M = Mo, W, Re) anions reveal square antiprismatic geometries.[59-60] However, to date, there has been no reported literature about adducts of $[MF_7]^-$ with neutral bases, suggesting insufficient Lewis acidity of the $[MF_7]^-$ anions, preventing coordination of neutral bases.

Whereas free WF_6 does not exhibit any evidence of fluoride ion donation, with $[WF_5]^+$ being extremely electrophilic, WF_6 has been shown to relinquish a fluoride when stabilized with organic bases in the presence of a sufficiently strong fluoride-ion acceptor. The ability of the transition metal hexafluoride to both accept and donate fluoride ions under certain conditions has led to the isolation of numerous cationic species. The first of which was isolated and characterized in 1992 by Bougon *et al.* Herein, the group reacted bipy with a slight excess of WF_6, resulting in the formation of the $[WF_4(bipy)_2]^{2+}$ dication and the $[WF_7]^-$ or $[W_2O_2F_9]^-$ anions via autoionization. The dication was found to possess a trigonal dodecahedral geometry (Eq 1.3).[45,61]

$$3WF_6 + 2bipy \rightarrow [WF_4(bipy)_2][WF_7]_2 \qquad \text{(Eq. 1.3)}$$

In 2018, Levason *et al.* explored the reactivity of WF_6 towards the softer ligands *o*-$C_6H_4(E)_2$ (X = $P(CH_3)_2$, $As(CH_3)_2$). Unlike the previously observed pyridine-based species, stoichiometric amounts of the transition metal hexafluoride and ligand still resulted in the formation of the $[WF_4\{o\text{-}C_6H_4(E(CH_3)_2)_2\}_2]^{2+}$ (E = P, As) dications. Crystal structures of these species were also observed to adopt distorted trigonal decahedral geometries. The diphosphine $(CH_3)_2PCH_2CH_2P(CH_3)_2$ was another ligand the group explored; however, this resulted in a mixture of $[WF_4\{(CH_3)_2PCH_2CH_2P(CH_3)_2\}][WF_7]_2$ and

$F_6W(CH_3)_2PCH_2CH_2P(CH_3)_2WF_6$.[48] In 2019, Gerken *et al.* found that $WF_6(L)$ (L = bipy, phen) could donate F^- to SbF_5 to form the $[WF_5(L)]^+$ (L = bipy, phen) cations (Eq. 1.4).

$$WF_6(L) + SbF_5 \bullet SO_2 \rightarrow [WF_5(L)][SbF_6] + SO_2 \text{ (L = bipy, phen)} \quad \text{(Eq. 1.4)}$$

The geometries of these cations were best described as 4 : 3 polyhedra, a rare hepta-coordinate geometry, based on closer structural analysis.[52] Monodentate ligands where also shown to be capable of causing WF_6 to relinquish a fluoride ion. In 2020, Gerken *et al.* were able to isolate and characterize $[WF_5(py)_3][O_3SCF_3]$ via the reaction of $WF_6(py)_2$ and $[(CH_3)_3Si(py)][O_3SCF_3]$ which was found to have a trigonal dodecahedral cation structure based on ^{19}F NMR spectroscopy and DFT calculations. However, $[WF_5(py)_2]^+$ was non-isolable and readily decomposes in pyridine, eventually producing $W^VF_5(py)_2$.[62] The group was able to further abstract a fluoride from this W(V) species in the presence of excess pyridine to form $[W^VF_4(py)_4][O_3SCF_3]$. Finally, reacting WF_6 with $(CH_3)_3SiO_3SCF_3$ and excess $P(CH_3)_3$ resulted in the formation of $[W^VF_4\{P(CH_3)_3\}][O_3SCF_3]$ with $P(CH_3)_3$ serving as both a ligand and a reducing agent.[63] Crystal structures of these two ionic W^V compounds served to develop the τ_8 and τ_8' geometry indices, with the group determining both aforementioned d^1 tungsten species to adopt square antiprismatic structures.

1.4 Ligand Substitution Chemistry

Tungsten hexafluoride has been observed to undergo reactions with many other species, resulting in the substitution of one or more fluorines for the respective ligand. Transition metal hexafluorides MF_6 (M = Mo, W) have been reacted with $Zn(CH_3)_2$ yielding $M(CH_3)_6$ (M = Mo, W) and were shown to adopt distorted C_{3v} trigonal-prismatic geometries.[64-66] Intermediate $WF_x(CH_3)_{6-x}$ species have been observed in the ^{19}F NMR

spectrum, however, only $WF_5(CH_3)$ could be assigned. Additionally, $Re(CH_3)_6$ has also been synthesized, instead being prepared from rhenium oxides, and was shown to adopt a trigonal prismatic geometry with an approximately D_{3h} symmetry.[64,66-67] Tungsten hexafluoride was able to react with pentamethylcyclopentadiene to form $W^V(Cp^*)F_4$. However, further oxidation in air resulted in the formation of $W(Cp^*)F_5$. X-ray crystallography of the compound revealed η^5-coordination of the $[Cp^*]^-$ ligand with the overall structure adopting an octahedral geometry.[68]

Numerous tungsten fluoride species have been isolated and/or characterized with W≡NR imido groups. Reactions of WF_6 with primary amines have resulted in the formation of ammonium tungsten imido salts of $[RNH_3][W(NR)F_5]$ (R = CH_3, C_2H_5, C_4H_9,).[69-70] These reactions were believed to arise from an initial adduction formation of the amine to WF_6 (Eq 1.5) followed by a subsequent elimination of HF to form a $WF_5(NHR)$ intermediate (Eq. 1.6). The latter intermediate would then react with the previous $WF_6(NH_2R)$ adduct to form the alkylammonium tungsten imido salts (Eq 1.7).[17,69]

$$WF_6 + RNH_2 \rightarrow WF_6(NH_2R) \quad (1.5)$$

$$WF_6(NH_2R) \rightarrow W(NHR)F_5 + HF \quad (1.6)$$

$$WF_6(NH_2R) + W(NHR)F_5 \rightarrow [RNH_3][W(NR)F_5] + WF_6 \quad (Eq.\ 1.7)$$

This was further supported by the findings of Seppelt and Huppman in 1985 via the reaction of MF_6 (M = Mo, W) with $TeF_5N(H)Si(CH_3)_3$. Herein, they observed equimolar amounts of $M(NTeF_5)F_4$ (M = Mo, W) and TeF_5NH_2 as products as opposed to the presumed ionic products.[71-72] Reactions with the silazane derivative, $RN\{Si(CH_3)_3\}_2$, have also resulted in the formation of these imido complexes via the elimination of $(CH_3)_3SiF$.

The addition of small, controlled amounts of RNH_2 (R = H, C_4H_9) to WF_6 in CH_3CN was found to instead afford $W(NR)F_4(NCCH_3)$ upon elimination of HF.[73] Meanwhile, the reaction of WF_6 with $C_6F_5NH_2$ resulted in an mixture of $[C_6F_5NH_3]^+$ with $[W(NC_6F_5)F_5]^-$, $[W_2(NC_6F_5)_2F_9]^-$, and F^- anions.[74] This is due to the $[W(NC_6F_5)F_5]^-$ anion existing in equilibrium with HF (Eq 1.8).[75]

$$2[W(NC_6F_5)F_5]^- + HF \rightleftharpoons [W_2(NC_6F_5)_2F_9]^- + [HF_2]^- \quad \text{(Eq 1.8)}$$

More recently, Gerken *et al.* have found that $WF_6(py)$ and $[N(CH_3)_4][WF_7]$ could react with $C_6F_5NH_2$ to form $[W(NC_6F_5)F_5]^-$ stabilized by $[C_5H_5NH]^+$ or $[N(CH_3)_4]^+$. The group also studied various $[W(NR)F_5]^-$ (R = H, F, CH_3, CF_3, C_6H_5, C_6F_5) anions using DFT calculations, revealing that the R group has substantial impact on structural properties such as the W≡N and W–F bond lengths as well as electronic properties.[75] Fluoride abstraction of $[C_5H_5NH][W(NC_6F_5)F_5]$ was found to be possible with AsF_5 giving rise to oligomeric $[W(NC_6F_5)F_4]_x$ with the group believing it to aggregate by asymmetric fluorine bridges.[76] In the presence of excess ligand, $[W(NC_6F_5)F_4]_x$ was found to also form stable adducts with $NCCH_3$ and NC_5H_5. Finally, computational studies of $W(NR)F_4$ (R = H, F, CH_3,CF_3, C_6F_5), performed by the group predicted them to be Lewis acidic with varying acidities depending the R group.[76] An alternative route to $W(NCH_3)F_4$ adducts stabilized by N-donor (NCH_3, $NCCH_3$, NC_5H_5) or O-donor ligands could be carried out by the reaction of WF_6 with $CH_3N\{Si(CH_3)_3\}_2$ in the presence of excess ligand.[70-71] Multinuclear NMR spectroscopic studies of these complexes suggested linear R–N–W–X (X = N, F) moieties based on both $J(^{14}N–^{1}H)$ and $^{2}J(^{19}F–^{14}N)$ coupling and thus significant W≡N triple bond character from the imido ligand.[77] This was confirm by Gerken *et al.* in 2017 through single-crystal X-

ray diffraction of $[C_5H_5NH][W(NC_6F_5)F_5]$ and $[C_5H_5NH][W_2(NC_6F_5)_2F_9]$ showing the linearity of the W≡N–C groups.[75]

Reactions with secondary amines or their silazane derivatives instead have resulted in $WF_5\{NR_2\}$ containing W–N single bonds.[78-80] When excess $(CF_3CH_2)_2NH$ was reacted with WF_6, $[(CF_3CH_2)_2NH_2][WF_5\{\eta^2\text{-}CH(CF_3)N(CH_2CF_3)\}]$ was observed as opposed to the anticipated $W(N(CF_3CH_2)_2)_2F_4$ species.[80] $WF_5\{NS(O)(CH_3)_2\}$ and *cis*-$WF_4\{NS(O)(CH_3)_2\}_2$ could be obtained via the reaction of WF_6 and $(CH_3)_3SiNS(O)(CH_3)_2$, with *mer*-$WF_3\{NS(O)(CH_3)_2\}_3$ being obtained with the use of $Li[NS(O)(CH_3)_2]$.[81] Homoleptic $M(N_3)_6$ (M = Mo, W) were prepared via a reaction of WF_6 with $(CH_3)_3SiN_3$, whereas $WF_5(N_3)$ is obtainable using a molar deficiency of the silazide. These transition metal azides were found to be explosive in the solid state.[82-83] Finally, while various anionic molybdenum fluoride species with terminal nitrides have been reported, only WNF_3 has been reported and has only been observed via IR spectroscopy in noble-gas matrices.[84-86]

Another well-explored group of fluorido tungsten derivatives are those containing bonds to sulfur. Derivatives containing M=S double bonds have been explored for the sulfide tetrafluorides of tungsten, molybdenum and rhenium. These species can be obtained via the reaction of their respective hexafluoride with elemental sulfur, or inorganic sulfides, such as B_2S_3 and Sb_2S_3, with selenide tetrafluoride synthesized in a similar manner utilizing Sb_2Se_3.[87-89] Much akin to WOF_4, WSF_4 has also shown to form neutral adducts with $WSF_4(NCCH_3)$ and $WSF_4(NC_5H_5)_n$ (n = 1, 2) having been identified.[90-92] Tungsten sulfide tetrafluoride has also been shown to act as a F^- acceptor with $[WSF_5]^-$ and $[W_2S_2F_9]^-$ salts reported.[93-94] All aforementioned species are known to be moisture-sensitive resulting, in

hydrolysis to form $[W_2O_2S_2F_6]^{2-}$ or $[W_2OSF_9]^-$.[94-95] Finally, the only experimental singly-bonded W–S derivatives that have been reported originate from the reaction of WF_6 with $S_2(CH_3)_2$ in CH_3CN. However, this led to a mixture of products with tentative assignments of $WF_5(SCH_3)$, $WF_4(SCH_3)_2$, $WSF_3(SCH_3)(NCCH_3)$, as well as $WSF_3(SCH_3)\{S_2(CH)_2\}$ in the ^{19}F NMR spectrum.[73]

Perhaps the most prolific derivatives of WF_6 are those containing oxygen ligands, such as those with M–O single bonds (M = W, Mo). Numerous synthetic pathways to $WF_5(OCH_3)$ have been reported using a variety of $[OCH_3]^-$ sources with higher substitutions of $MF_n(OCH_3)_{6-n}$ (n = 1-4) being prepared with $Si(CH_3)_x(OCH_3)_{4-x}$ (x = 0-3).[94-100] However, $W(OCH_3)_6$ was best prepared by further reacting $WF_5(OCH_3)$ with $Na[OCH_3]$ as the reaction with the aforementioned silane resulted in a mixture.[101] While molybdenum equivalents exist in the form of $MoF_n(OCH_3)_{6-n}$ (n = 0-2), $MoF_5(OCH_3)$ has not been observed, with the reaction of MoF_6 with $Si(CH_3)_x(OCH_3)_{4-x}$ (x = 0-3) found to be explosive if warmed too hastily.[102] Derivatives of $WF_5(OC_2H_5)$ and $WF_5(OC_6H_5)$ have been prepared in a similar manner to the methoxy variant, however, no molybdenum analogues have been reported.[98-99] Utilizing more electron-withdrawing ligands, $MF_5(OC_6H_5)$, $MF_5(OC_6F_5)$, and *cis*-$MF_4(OCH_2CF_3)_4$ (M = W, Mo) have been prepared, with $MoF_n(OCH_2CF_3)_{6-n}$ (n = 0-3) also being reported.[80,102-103] However, only $WF_5(OCH_2CF_3)$ has been reported to act as a F^- acceptor, reacting with CsF to form $[Cs][WF_6(OCH_2CF_3)]$.[75] Interestingly, the reaction with WF_6 and $Li[OC(CF_3)_3]$ instead lead to the formation of $WF_5\{OC(CF_3)_3\}$.[102] The series of $WF_n(OTeF_5)_{6-n}$ (n = 1-5) have been prepared by reacting WF_6 with $B(OTeF_5)_3$. Attempts to do the same with MoF_6 instead

lead to the evolution of TeF_6 and $MoOF_3(OTeF_5)$ before leading to further decomposition.[104-105]

Perhaps the most well-known metal oxide derivatives are those containing M=O (M = Cr, Mo, W, Re) bonds often formed by the intentional or accidental exposure to traces of water. The reaction of H_2O with MoF_6 resulted in the formation of $MoOF_4$, whereas the same reaction with WF_6 resulted in the formation of $[H_3O][W_2O_2F_9]$, and for ReF_6 in a mixture of the neutral and ionic products.[106-107] Ligand-substitution reactions of MF_6 (M = Mo, W, Re) with B_2O_3, or SiO_2/HF have also resulted in formation of their respective MOF_4.[108-110] Of note, $CrOF_4$ has also been prepared, however, via the oxidation of CrO_2F_2 with KrF_2 as CrF_6 has yet to be synthesized.[111] As gas-phase MOF_4 species are pentacoordinate, they are instead found as polymeric zig-zag chains, with the exception of WOF_4 which forms tetramers in the solid state to achieve hexacoordination.[112-115] Neutral adducts of MOF_4 (M = Mo, W) with various neutral main-group donor ligands have been isolated.[44,116-118] Unlike with WF_6, WOF_4, when reacted with bidentate phosphorus ligands, yields neutral $WOF_4(L)$ adducts as opposed to autoionization or bridged species.[119] Due to WOF_4 being a weaker oxidizing agent, it has also been found to coordinate to oxygen-based donor ligands, a feat unreported by WF_6.[117] When reacted with NgF_2 (Ng = Kr, Xe), MOF_4 (M = Mo, W) resulted in the formation of chain adducts of $NgF_2\cdot(MOF_4)_n$ (n = 1–4), with increasing $[NgF][M_nO_nF_{4n+1}]$ character proportional to n.[120-122] The chromium variants $NgF_2\cdot(CrOF_4)_n$ (n = 1, 2), have also been reported and represent the first neutral adducts of $CrOF_4$.[114] The transition metal oxide tetrafluorides, MOF_4 (M = Cr, Mo, W, Re), have also been shown to act as fluoride acceptors to form various $[MOF_5]^-$ (M = Cr, Mo, W, Re)[123-128], $[M_2O_2F_9]^-$ (M = Mo, W)[110,125,129-130], and

$[MOF_6]^{2-}$ (M = Mo, W)[125,131] salts. Crystal structures of $[WOF_5]^-$ have often exhibited disorder in oxido and fluorido ligands.[48,132-134] More recently, however, ordered examples of $[MOF_5]^-$ (M = Cr, Mo, W) have been reported.[135-136] Conversely, $[M_2O_2F_9]^-$ (M = Mo, W) has not been reported to be disordered as the oxido ligands preferred to be *trans* to the bridging fluoride ligand.[61,106,134-136] Finally, ^{19}F NMR spectroscopy of the $[WOF_6]^{2-}$ anion revealed a pentagonal-bipyramidal geometry with an axial oxido ligand.[137]

Transition-metal dioxide difluorides, MO_2F_2 (M = Cr, Mo, W) have been reported as adducted species or in rare cases as the pure compound. Pure samples of MoO_2F_2 and CrO_2F_2 have been prepared by different means. The former requires pyrolysis of $Na_2[MoO_2F_4]\bullet 2H_2O$, with the latter prepared by fluorination of CrO_3 or CrO_2Cl_2.[138-140] Reactions of MF_6 (M = Mo, W) with $\{(CH_3)_3Si\}_2O$ or H_2O alongside N or O-donor ligands have allowed for facile synthetic routes to adducted MoO_2F_2 and WO_2F_2 species.[117-118] Numerous salts of *cis*-$[MO_2F_4]^{2-}$ (M = Cr, Mo, W) have been prepared, and crystal structures of both molybdenum and tungsten compounds have displayed both static and dynamic disorder of the oxido and fluorido ligands.[141-142] Finally, Green and Gard have obtained the IR spectra of $[NO_{1-2}][CrO_2F_3]$ and have assumed *cis*-dioxo arrangements and polymeric, *cis*-fluorine-bridged structures.[143] Meanwhile, attempts to synthesize $[MO_2F_3]^-$ (M = Mo, W) have instead resulted in the dimerized $[M_2O_4F_6]^{2-}$.[95,127,144]

1.5 Objectives and Impact of Research

Transition-metal hexafluoride chemistry is still in relative naissance with much of its studies still focused on fundamental chemistry. As mentioned above, tungsten hexafluoride has long been established to act as a Lewis acid, base and oxidizing agent.

The primary objective of this research will be to further expand the chemical behaviour of WF_6 towards novel ligands and to examine the effect of mixing ligands.

Tungsten hexafluoride has been known to form adducts with both nitrogen and phosphorus ligands. However, despite possessing some physical similarity, numerous chemical differences exist between the two families. For example, while $[WF_5]^+$ species exist stabilized by nitrogen donors, no literature precedence is reported for $[WF_5]^+$ cations stabilized by phosphine ligands.[52,62] Presumably, this may be due to potential phosphine ligands being oxidized to P(V) fluoride species with concomitant reduction of W(VI) to W(V) as observed in the synthesis of $[W^VF_4\{P(CH_3)_3\}][O_3SCF_3]$.[63] However, bidentate phosphorus species have induced autoionization of WF_6 without ligand oxidation.[48] To date, no adducts have been prepared with mixed P/N adducts. In Chapter 3, the reaction of WF_6 towards molar equivalents of pyridine and $P(CH_3)_3$ will be studied.

Tungsten oxide tetrafluoride has been shown to form many adducts with nitrogen, and of note, oxygen-based ligands. While WF_6 is indeed a stronger oxidizer than WOF_4, a few of these oxygen-based donors possess BF_3 affinities that are stronger than that of trimethyl phosphine, which is known to adduct to WF_6.[145] Additionally, $O{=}PX_3$ species are already in the +5 oxidation state, making further oxidation impossible. However, coordination to the metal centre could result in further polarization of the P=O bond, which may result in fluorine/oxygen exchange as the phosphorus atom takes on a more positive charge. In Chapter 4, reactions of WF_6 with OPX_3 (X = C_2H_5, Ph) will be studied.

Lastly, exploration of WF_6 towards ligands of higher denticity are of interest. No instances of tungsten forming species with a coordination number of nine or higher have been reported. However, the reaction of bipy with excess WF_6 led to autoionization.[45] This

in turn could be exploited to allow for higher denticity ligands such as the tridentate 2,2′:6′,2′′-terpyridine (terpy) to be coordinated to the metal centre. This would mark the first conclusive W(VI) fluorido species with multidentate ligands as $[WF(terpy)_2][PF_6]$ was proposed in multiple oxidation states due to the redox non-innocence of terpy.[146] In Chapter 5, reactions of WF_6 with tridentate terpy will be studied.

1.6 References

1. Molski, M. J.; Seppelt, K. The Transition Metal Hexafluorides. *Dalton Trans.* **2009**, *18*, 3379–3383. DOI: 10.1039/b821121c

2. Seppelt, K. Molecular Hexafluorides. *Chem. Rev.* **2015**, *115* (2), 1296–1306. DOI: 10.1021/cr5001783

3. Weinstock, B.; Claassen, H. H.; Malm, J. G. Platinum Hexafluoride[1]. *J. Am. Chem. Soc.* **1957**, *79* (21), 5832. DOI: 10.1021/ja01578a073

4. Malm, J. G.; Selig H.; Fried, S. The Preparation and Properties of ReF_7[1]. *J. Am. Chem. Soc.* **1960**, *82* (6), 1510. DOI: 10.1021/ja01491a065

5. Selig, H.; Chernick, L. C.; Malm, J. G. The preparation and properties of TcF_6. *J. Inorg. Nucl. Chem.* **1961**, *19* (3-4), 377. DOI: 10.1016/0022-1902(61)80132-2

6. Claassen, H. H.; Selig, H. Malm, J. G. Ruthenium Hexafluoride[1] *J. Am. Chem. Soc.* **1961**, *83* (10), 2390–2391. DOI: 10.1021/ja01471a039

7. Chernick, C. L.; Claassen, H. H.;Weinstock, B. Rhodium Hexafluoride[1]. *J. Am. Chem. Soc.* **1961**, *83* (14), 3165–3166. DOI: 10.1021/ja01475a046

8. Chemnitz, T.; Koch, B. N.; Buchner, M. R.; Petry, W.; Kraus F. Plasmachemical syntheses of RuF_6, RhF_6, and PtF_6. *Inorg. Chem.* **2023**, *62* (40), 16263-16273. DOI: 10.1021/acs.inorgchem.3c02452.

9. Glemser, O.; Roesky, H.; Hellberg, K. H. Darstellung von Chrompentafluorid und chromhexafluorid. *Angew. Chem.* **1963**, *75* (7), 346–347. DOI: 10.1002/ange.19630750711

10. Jacobs, J.; Mueller, H. S. P; Willner, H.; Buerger, H. Vibrational and Electronic Spectra of Molecular Chromium Tetrafluoride, CrF_4, and Chromium Pentafluoride, CrF_5. Comments on the Existence of Chromium Hexafluoride, CrF_6. *Inorg. Chem.* **1992**, *31* (26), 5357–5363. DOI: 10.1021/ic00052a008

11. Lin, J.; Yang, Q.; Li, X.; Zhang, X.; Li, F.; Yang, G. Pressure-Stabilized Hexafluorides of First-Row Transition Metals. *Phys. Chem. Chem. Phys.* **2022,** *24* (3)*,* 1736-1742. DOI: 10.1039/d1cp04446j

12. Wilson, A. V.; Nguyen, T.; Brosi, F.; Wang, X.; Andrews, L.; Riedel S.; Bridgeman, A. J.; Young, N. A. A Matrix Isolation and Computational Study of Molecular Palladium Fluorides: Does PdF_6 Exist? *Inorg. Chem.* **2016**, *55* (3) 1108–1123. DOI: 10.1021/acs.inorgchem.5b02273

13. Lin, J.; Zhang, S.; Guan, W.; Yang, G.; Ma, Y. Gold with +4 and +6 Oxidation States in AuF_4 and AuF_6. *J. Am. Chem. Soc.* **2018**, *140* (30) 9545–9550. DOI: 10.1021/jacs.8b04563

14. Craciun, R.; Picone, D.; Long, R. T.; Li, S.; Dixon, D. A.; Peterson, K. A.; Christe, K. O. Third Row Transition Metal Hexafluorides, Extraordinary Oxidizers, and Lewis Acids: Electron Affinities, Fluoride Affinities, and Heats of Formation of WF_6, ReF_6, OsF_6, IrF_6, PtF_6, and AuF_6. *Inorg. Chem.* **2010**, *49* (3), 1056–1070. DOI: 10.1021/ic901967h

15. Aullon, G.; Alvarez, S. On the Existence of Molecular Palladium(VI) Compounds: Palladium Hexafluoride. *Inorg. Chem.* **2007**, *46* (7), 2700–2703. DOI: 10.1021/ic0623819

16. Miyoshi, E.; Sakai, Y. Theoretical Study on Electronic Structures of AuF_6 and Its Anions. *J. Chem. Phys.* **1988**, *89* (12), 7363–7366. DOI: 10.1063/1.455267

17. Riedel, S.; Kaupp, M. Has AuF_7 Been Made? *Inorg. Chem.* **2006**, *45* (3), 1228–1234 DOI: 10.1021/ic051944y

18. Craciun, R.; Long, R. T.; Dixon, D. A.; Christe, K. O. Electron Affinities, Fluoride Affinities, and Heats of Formation of the Second Row Transition Metal Hexafluorides: MF_6 (M = Mo, Tc, Ru, Rh, Pd, Ag). *J. Phys. Chem. A.*, **2010,** *114* (28), 7571–7582. DOI: 10.1021/jp1022949

19. D. Turnbull, *Lewis–Acid Behaviour of Neutral and Cationic Fluoridotungsten(V) and (VI) Complexes*, Ph.D. Thesis, University of Lethbridge, Lethbridge, AB, **2020**.

20. Drews, T.; Supeł, J.; Hagenbach, A. and Seppelt, K. Solid State Molecular Structures of Transition Metal Hexafluorides. *Inorg. Chem.* **2006**, *45* (9), 3782–3788. DOI: 10.1021/ic052029f

21. Siegel, S.; Northrop, D. A. X-ray Diffraction Studies of Some Transition Metal Hexafluorides. *Inorg. Chem.* **1966**, *5* (12), 2187–2188. DOI: 10.1021/ic50046a025

22. Blondel, C.; Cacciani, P.; Delsart, C.; Trainham, R. High-Resolution Determination of the Electron Affinity of Fluorine and Bromine Using Crossed Ion and Laser Beams. *Phys. Rev. A.* **1989**, *40* (7), 3698– 3701. DOI: 10.1103/PhysRevA.40.3698

23. Bartlett, N. The Oxidizing Properties of the Third Transition Series Hexafluorides and Related Compounds. *Angew. Chem., Int. Ed. Engl.* **1968**, *7* (6), 433–439. DOI: 10.1002/anie.196804331

24. Lucier, G.; Shen, C.; Casteel, W. J.; Chacón, L.; Bartlett, N. Some Chemistry of High Oxidation State Transition Metal Fluorides in Anhydrous HF. *J. Fluorine Chem.* **1995**, *72* (2), 157–163. DOI: 10.1016/0022-1139(94)00401-z.

25. Christe, K. O.; Wilson, W. W.; Wilson, R. D. Coordinatively Saturated Fluoro Cations. Oxidative Fluorination Reactions with Fluorokrypton(1+) Salts and Platinum Hexafluoride (PtF_6). *Inorg. Chem.* **1984**, *23* (14), 2058–2063. DOI: 10.1021/ic00182a016.

26. Bartlett, N. Low Temperature Preparation and Uses of Potent Oxidizers. *J. Fluorine Chem.* **2006**, *127* (10), 1285–1288. DOI: 10.1016/j.jfluchem.2006.05.021

27. Bartlett, N.; Lohmann, D. H. 1005. Fluorides of the Noble Metals. Part II. Dioxygenyl Hexafluoroplatinate(V), $O_2^+[PtF_6]^-$. *J. Chem. Soc.* **1962**, 5253–5261. DOI: 10.1039/jr9620005253

28. Bartlett, N. Xenon Hexafluoroplatinate(v) $Xe^+[PtF,]^-$ *Proc. Chem. Soc.* **1962**, 218. DOI: 10.1039/PS9620000197

29. Graham, L.; Graudejus, O.; Jha, N. K.; Bartlett, N. Concerning the nature of $XePtF_6$. *Coord. Chem. Rev.* **2000**, *197* (1), 321–334. DOI: 10.1016/S0010-8545(99)00190-3.

30. Botkovitz, P.; Lucier, G. M.; Rao, R. P.; Bartlett, N. The Crystal Structure of $O_2^+RuF_6^-$ and the Nature of O_2RhF_6. *Acta Chim. Slov.* **1999**, *46* (2), 141–154.

31. Tamadon, F.; Seidel, S.; Seppelt, K. Reactions of Xenon with Iridium and Osmiumhexafluoride. *Acta Chim. Slov.* **2013**, *60* (3), 491–494.

32. Seidel, S.; Seppelt, K. The Cl_4^+ Ion. *Angew. Chem. Int. Ed.* **2000**, *39* (21), 3923–3925. DOI: 10.1002/1521-3773(20001103)39:21<3923::AID-ANIE3923>3.0.CO;2-Y

33. Padma, D. K.; Peacock, R. D. Reactions of Bromine and Chlorine with Osmium Hexafluoride. *J. Fluorine Chem.* **1981**, *17* (6), 539–541. DOI: 10.1016/S0022-1139(00)82260-5

34. McGhee, L.; Rycroft, D. S.; Winfield, J. M. Oxidation of Molecular Bromine by Uranium Hexafluoride in Acetonitrile. Preparation and Properties of Hexafluorouranates(V) Containing Positive Bromine. *J. Fluorine Chem.* **1987**, *36* (3), 351– 359. DOI: 10.1016/S0022-1139(00)82077-1

35. Berry, J. A.; Prescott, A.; Sharp, D. W. A.; Winfield, J. M. Redox Reactions Involving Rhenium and Uranium Hexafluorides, a Convenient Synthesis of β-Uranium Pentafluoride. *J. Fluorine Chem.* **1977**, *10* (3), 247–254. DOI: 10.1016/S0022-1139(00)82138-7

36. Anderson, G. M.; Winfield, J. M. Preparation and Properties of Bis(Acetonitrile)Iodine(I) Hexafluoromolybdate(V) and Hexafluorouranate(V). *J. Chem. Soc., Dalton Trans.* **1986,** *2*, 337–341. DOI: 10.1039/DT9860000337.

37. Moock, K.; Turowsky, L.; Seppelt, K. Ferricenium Hexafluoromolybdate(V) - Tungstate(V) and -Uranate (V) Preparation and Electrochemical Identification. *J. Fluorine Chem.* **1987**, *37* (2), 253–258. DOI: 10.1016/S0022-1139(00)82021-7

38. Moock, K. H.; Rock, M. H. Redox Reactions of Metallocenes with Tungsten and Molybdenum Hexafluoride. *J. Chem. Soc. Dalton Trans.* **1993**, *16*, 2459–2463. DOI: 10.1039/DT9930002459

39. Gowik, P.; Klapötke, T. $Cp_2NbCl_2^+X^-$ ($X = WF_6^-$, $AlCl_4^-$): Synthese, Charakterisierung und Reaktivität Gegenüber $AlCl_3$. *J. Fluorine Chem.* **1990**, *47* (2), 273–281. DOI: 10.1016/S0022-1139(00)82379-9

40. Cameron, T. S.; Klapötke, T. M.; Schulz, A.; Valkonen, J. Preparation and Crystal Structure of $[WCl_2(cp)_2]^+_2[W_4F_{18}]^{2-}$(cp =η-$C_5H_5$) Containing the New Binary Tungsten(IV) Fluoride Anion $[W_4F_{18}]^{2-}$. *J. Chem. Soc. Dalton Trans.* **1993**, *5*, 659–662. DOI: 10.1039/DT9930000659

41. Paine, R. T.; Asprey, L. B.; Graham, L.; Bartlett, N. In *Inorganic Syntheses, Volume XIX*; Shriver, D. F., Ed.; **1979**; pp 137–140.

42. Tebbe, F. N.; Muetterties, E. L. Further Evidence of Stereochemical Nonrigidity in Five- and Seven-Coordinate Structures. *Inorg. Chem.* **1968**, *7* (1), 172–174. DOI: 10.1021/ic50059a040

43. Steigel, A.; Brownstein, S. Fluorine Exchange in Complexes of Tungsten Hexafluoride. *J. Am. Chem. Soc.* **1974**, *96* (19), 6227. DOI: 10.1021/ja00826a069

44. Arnaudet, L.; Bougon, R.; Ban, B.; Lance, M.; Nierlich, M.; Vigner, J. Preparation, Characterization, and Crystal Structure of the Adducts WF_6•F-py and WOF_4•F-py (F-py = 2-Fluoropyridine). *Inorg. Chem.* **1993**, *32* (7), 1142–1146. DOI: 10.1021/ic00059a020

45. Arnaudet, L.; Bougon, R.; Ban, B.; Lance, M.; Navaza, A.; Nierlich, M.; Vigner, J. 2,2'-Bipyridine Fluoro Complexes of Tungsten(VI): Preparation, Characterization and Crystal Structure of $[WF_4(bipy)_2]^{2+}$ • $2[WF_7]^-$ • WF_6 and $[WF_4(bipy)_2]^{2+}$ • $2[WF_7]^-$ • CH_3CN; Preparation and Characterization of WF_6 bipy. *J. Fluorine Chem.* **1994**, *67* (1), 17-25. DOI: 10.1016/0022-1139(93)02926-6

46. Arnaudet, L.; Bougon, R.; Buu, B.; Lance, M.; Nierlich, M.; Thuéry, P.; Vigner, J. Characterization of the adducts WF_6•py and WF_6•2py (py = pyridine): crystal structure of WF_6•2py. *J. Fluorine Chem.* **1995**, *71* (1), 123–129. DOI: 10.1016/0022-1139(94)03160-2

47. Turnbull, D.; Kostiuk, N.; Wetmore, S. D.; Gerken, M. Syntheses, Characterization, and Computational Studies of Tungsten Hexafluoride Adducts with Pyridine and Its Derivatives. *J. Fluorine Chem.* **2018**, *215*, 1–9. DOI: 10.1016/j.jfluchem.2018.08.007

48. Levason, W.; Monzittu, F. M.; Reid, G.; Zhang, W. Neutral and Cationic Tungsten(VI) Fluoride Complexes with Tertiary Phosphine and Arsine Coordination, *Chem. Commun.* **2018**, *54* (83), 11681–11684. DOI: 10.1039/C8CC05598J

49. El-Kurdi, S.; Al-Terkawi, A.-A.; Schmidt, B.; Dimitrov, A.; Seppelt, K. Tungsten(VI) and Tungsten(V) Fluoride Complexes. *Chem. Eur. J.*, **2010**, *16* (2), 595–599. DOI: 10.1002/chem.200902307.

50. Muetterties, E. L.; Wright, C. M. Molecular Polyhedra of High Co-ordination Number. *Quart. Rev. (London).* **1967**, *21* (1), 115. DOI: 10.1039/qr9672100109

51. Lin, Z.; Bytheway, I. Stereochemistry of Seven-Coordinate Main Group and d0 Transition Metal Molecules. *Inorg. Chem.* **1996**, *35* (3), 594–603. DOI: 10.1021/ic950271o

52. Turnbull, D.; Wetmore, S. D., Gerken, M. Stabilization of $[WF_5]^+$ by Bidentate N-Donor Ligands. *Angew. Chem.* **2019**, *58* (37), 13169-13172. DOI: 10.1002/ange.201906600

53. Hargreaves, G. B.; Peacock, R. D. 442. Higher Complex Fluorides of Tungsten. *J. Chem. Soc.* **1958**, 2170–2175. DOI: 10.1039/jr9580002170

54. Hargreaves, G. B.; Peacock, R. D. 890. Higher Complex Fluorides of Molybdenum. *J. Chem. Soc.* **1958**, 4390–4393. DOI: 10.1039/jr9580004390

55. Beuter, A.; Kuhlmann, W.; Sawodny, W. Vibrational Spectra of Hepta- and Octafluorocomplexes of Molybdenum(VI), Tungsten(VI) and Rhenium(VI). *J. Fluorine Chem.* **1975**, *6* (4), 367–378. DOI: 10.1016/s0022-1139(00)85313-0.

56. Giese, S.; Seppelt, K. Structural Principles in Seven-Coordinate Subgroup Compounds: The Complex Anions MoF_7^-, WF_7^-, and $ReOF_6^-$. *Angew. Chem., Int. Ed. Engl.* **1994**, *33* (4), 461–463. DOI:10.1002/anie.199404611.

57. Vogt, T.; Fitch, A. N.; Cockcroft, J. K. Crystal and Molecular Structures of Rhenium Heptafluoride. *Science* **1994**, *263* (5151), 1265–1267. DOI: 10.1126/science.263.5151.1265.

58. Malta, J. G.; Selig, H.; Siegel, S. Complex Compounds of Uranium Hexafluoride with Sodium Fluoride and Potassium Fluoride. *Inorg. Chem.* **1966**, *5* (1), 130–132. DOI: 10.1021/ic50035a031

59. Adam, S.; Ellern, A.; Seppelt, K. Structural Principles of the Coordination Number Eight: WF_8^{2-}, ReF_8^{2-}, and XeF_8^{2-}. *Chem. Eur. J.* **1996**, *2* (4), 398–402, DOI: 10.1002/chem.19960020408

60. Hwang, I. C.; Seppelt, K. The structures of ReF_8^- and UF_8^{2-} *J. Fluorine Chem.* **2000**, *102* (1–2), 69–72. DOI: 10.1016/S0022-1139(99)00248-1

61. Arnaudet, L.; Bougon, R.; Ban, B.; Lance, M.; Navaza, A.; Nierlich, M.; Vigner, J. Structure of the New Fluoro Complex of Tungsten(VI): $[WF_4(bipy)_2]^{2+} \bullet 2[W_2O_2F_9]^- \cdot 0.25HF$ (bipy = 2,2′-bipyridine). *J. Fluorine Chem.* **1992**, *59* (1), 141–152. DOI: 10.1016/S0022-1139(00)80212-2

62. Turnbull, D.; Hazendonk, P.; Wetmore, S. D.; Gerken, M. Stabilisation of $[WF_5]^+$ and WF_4 by Pyridine: Facile Access to $[WF_5(NC_5H_5)_3]^+$ and $WF_5(NC_5H_5)_2$. *Chem. - Eur. J.* **2020**, *26* (30), 6879-6886. DOI: 10.1002/chem.202000424

63. Turnbull, D.; Wetmore, S. D.; Gerken, M. Stabilisation of $[W^{V}F_4]^+$ by N- and P-Donor Ligands: Second-Order Jahn-Teller Effects in Octacoordinate d^1 Complexes. *Chem. - Eur. J.* **2021**, *27* (44), 11335-11343. DOI: 10.1002/chem.202100863

64. Kleinhenz, S.; Pfennig, V.; Seppelt, K. Preparation and Structures of $[W(CH_3)_6]$, $[Re(CH_3)_6]$, $[Nb(CH_3)_6]^-$, and $[Ta(CH_3)_6]^-$. *Chem. Eur. J.* **1998,** *4* (9), 1687–1691. DOI: 10.1002/(SICI)1521-3765(19980904)4:9<1687::AID-CHEM1687>3.0.CO;2-R.

65. Roessler, B.; Seppelt, K. $[Mo(CH_3)_6]$ und $[Mo(CH_3)_7]^-$. *Angew. Chem. Int. Ed.* **2000**, *39* (7), 1259–1261. DOI: 10.1002/(SICI)1521-3757(20000403)112:7<1326::AID-ANGE1326>3.0.CO;2-0.

66. Pfennig, V.; Seppelt, K. Crystal and Molecular Structures of Hexamethyltungsten and Hexamethylrhenium. *Science* **1996**, *271* (5249), 626–628. DOI: 10.1126/science.271.5249.626

67. Galyer, L.; Mertis, K.; Wilkinson, G. New Synthesis of Hexamethyltungsten(vi); Hexamethylrhenium(vi) and Dioxotrimethylrh Enium(VII). *J. Organomet. Chem.* **1975**, *85* (3), C37-C38. DOI: 10.1016/s0022-328x(00)80315-0

68. Köhler, K.; Herzog, A.; Steiner, A.; Roesky, H. W. Synthesis and Structure of the First Cyclopentadienyl(Halogeno)Metal(VI) Complex of the Chromium Triad $[((\eta^5\text{-}C_5Me_5)WF_5)]$ *Angew. Chem. Int. Ed. Engl.* **1996**, *35* (3), 295–297. DOI: 10.1002/anie.199602951

69. Chambers, O. R.; Rycroft, D. S.; Sharp, D. W. A.; Winfield, J. M. Aminolysis Reactions of Tungsten Hexafluoride: N-alkylimidofluorotungstates(VI). *Inorg. Nucl. Chem. Lett.* **1976**, *12* (7), 559–561. DOI: 10.1016/0020-1650(76)80022-0

70. Chambers, O. R.; Harman, M.; Rycroft, D. S.; Sharp, D. W. A.; Winfield, J. M. Aminolysis reactions of tungsten hexafluoride N-alkylimidofluorotungstates(vi). *J. Chem. Res.* **1977**, 1849–1876.

71. Huppmann, P.; Seppelt, K. Übergangsmetallverbindungen Mit Der Gruppe = N-TeF_5. *Chem. Ber.* **1985**, *118* (2), 457–461. DOI: 10.1002/cber.19851180207

72. Seppelt, K. Synthesis and Reactions of Aminotellurium Pentafluoride. *Inorg. Chem.* **1973**, *12* (12), 2837–2839. DOI: 10.1021/ic50130a019.

73. Kokunov, Y. V.; Chubar, Y. D.; Bochkareva, V. A.; Buslaev, Y. A. Iminolysis of Tungsten Hexafluoride. *Koord. Khim.* **1975**, *1* (8), 1100–1105.

74. Fawcett, J.; Griffith, G. A.; Peacock, R. D.; Russell, D. R. The Reaction Between Tungsten Hexafluoride and Pentafluoroaniline. *Polyhedron* **1988**, *7* (19), 2015–2022. DOI: 10.1016/S0277-5387(00)80717-2.

75. Turnbull, D.; Wetmore, S. D.; Gerken, M. Syntheses and Characterization of $W(NC_6F_5)F_5^-$ and $W_2(NC_6F_5)_2F_9^-$ Salts and Computational Studies of the $W(NR)F_5^-$ (R

= H, F, CH_3, CF_3, C_6H_5, C_6F_5) and $W_2(NC_6F_5)_2F_9^-$ Anions. *Inorg. Chem.* **2017**, *56* (20), 12581–12593. DOI: 10.1021/acs.inorgchem.7b02048.

76. Turnbull, D.; Wetmore, S. D.; Gerken, M. Synthesis, Characterization, and Lewis Acid Behavior of $[W(NC_6F_5)F_4]_x$ and Computational Study of $W(NR)F_4$ (R = H, F, CH_3, CF_3, C_6H_5, C_6F_5), $W(NC_6F_5)F_4(NCCH_3)$, and $W(NC_6F_5)F_4(NC_5H_5)_n$ (n = 1, 2) *Inorg. Chem.* **2019**, *58* (9), 6363– 6375. DOI: 10.1021/acs.inorgchem.9b00574.

77. Harman, M.; Sharp, D. W. A.; Winfield, J. M. ^1H ^{14}N spin-spin coupling in methylimidotungsten(VI) tetrafluoride, acetonitrile. *Inorg. Nucl. Chem. Lett.* **1974**, *10* (2), 183–185. DOI: 10.1016/0020-1650(74)80164-9

78. Majid, A.; McLean, R. R.; Ouellette, T. J.; Sharp, D. W. A.; Winfield, J. M. Diethylaminotungsten(VI) fluorides. *Inorg. Nucl. Chem. Lett.* **1971**, *7* (1), 53–56. DOI: 10.1016/0020-1650(71)80122-8

79. Majid, A.; McLean, R. R.; Sharp, D. W. A.; Winfield, J. M. Diethylaminotungsten (V1) Fluorides and Related Compounds, *Z. Anorg. Allg. Chem.* **1971**, *385* (1–2), 85–91. DOI: 10.1002/zaac.19713850112.

80. Dimitrov, A.; Seidel, S.; Seppelt, K. Substituted Tungsten Fluorides. *Eur. J. Inorg. Chem.* **1999**, *1999* (1), 95–99. DOI: 10.1002/(SICI)1099-0682(199901)1999:1<95::AID-EJIC95>3.0.CO;2-2

81. Roesky, H. W.; Scholz, M.; Edelmann, F.; Noltemeyer, M.; Sheldrick, G. M. Reaktionen von Übergangsmetallhalogeniden mit Dimethylsulfoximin- Derivaten – Röntgenstrukturanalyse von $F_5WNS(O)Me_2$ und $F_4W[NS(O)Me_2]_2$. *Chem. Ber.* **1987**, *120* (11), 1881–1884. DOI: 10.1002/cber.19871201117.

82. Haiges, R.; Boatz, J. A.; Bau, R.; Schneider, S.; Schroer, T.; Yousufuddin, M.; Christe, K. O. Polyazide Chemistry: The First Binary Group 6 Azides, $Mo(N_3)_6$, $W(N_3)_6$, $[Mo(N_3)_7]^-$, and $[W(N_3)_7]^-$, and the $[NW(N_3)_4]^-$ and $[NMo(N_3)_4]^-$ Ions‡ *Angew. Chem. Int. Ed.* **2005**, *44* (12), 1860–1865. DOI: 10.1002/ange.200462740.
83. Fawcett, J.; Peacock, R. D.; Russell, D. R. Preparation and Structure of Azidopentafluorotungsten(vi). *J. Chem. Soc., Dalton Trans.* **1980**, *11*, 2294. DOI: 10.1039/dt9800002294

84. Wang, X.; Andrews, L.; Lindh, R.; Veryazov, V.; Roos, B. O. A Combined Theoretical and Experimental Study of Simple Terminal Group 6 Nitride and Phosphide $N{\equiv}MX_3$ and $P{\equiv}MX_3$ Molecules. *J. Phys. Chem. A.* **2008**, *112* (35), 8030–8037. DOI: 10.1021/jp804469a

85. Fenske, D.; Liebelt, W.; Dehnicke, K. $AsPh_4[MoNF_4]$; Darstellung, Kristallstruktur und Schwingungsspektrum. *Z. Anorg. Allg. Chem.* **1980**, *467* (1), 83–88. DOI: 10.1002/zaac.19804670110

86. Völp, K.; Dehnicke, K.; Fenske, D. Synthese und Kristallstruktur des Nitridokomplexes [Na-15-Krone-5]$_2$[MoNF$_4$]$_2$ • 2 CH$_3$CN. *Z. Anorg. Allg. Chem.* **1989**, *572* (1), 26–32. DOI: 10.1002/zaac.19895720104

87. Gerken, M. In *Efficient Preparations of Fluorine Compounds*; Roesky, H. W., Ed.; John Wiley & Sons, Inc.: Hoboken, NJ, USA, **2012**; pp 79–81.

88. Atherton, M. J.; Holloway, J. H. Preparation and Characterization of Tungsten Selenotetrafluoride, WSeF$_4$ *Inorg. Nucl. Chem. Lett.* **1978**, *14* (2–3), 121–123. DOI: 10.1016/0020-1650(78)80044-0

89. Holloway, J. H.; Puddick, D. C. Preparation and Characterization of Molybdenum Thio- and Seleno-Tetrafluorides, MoSF$_4$ and MoSeF$_4$. *Inorg. Nucl. Chem. Lett.* **1979**, *15* (2), 85-87. DOI: 10.1016/0020-1650(79)80064-1

90. Holloway, J. H.; Kaučič, V.; Russell, D. R. Synthesis, Chemistry, and Crystal Structures of High-Valent Transition-Metal Chalcogenide Fluorides and their Derivatives. *J. Chem. Soc., Chem. Commun.* **1983**, *19*, 1079–1081. DOI: 10.1039/C39830001079

91. Nieboer, J.; Hillary, W.; Yu, X.; Mercier, H. P. A.; Gerken, M. Syntheses, Characterization, and Computational Study of WSF$_4$ and WSF$_4$•CH$_3$CN. *Inorg. Chem.* **2009**, *48* (23), 11251–11258. DOI: 10.1021/ic901752w

92. Nieboer, J.; Yu, X.; Chaudhary, P.; Mercier, H. P. A.; Gerken, M. Synthesis, Characterization, and Computational Study of WSF$_4$•NC$_5$H$_5$. *Z. Anorg. Allg. Chem.* **2012**, *638* (3–4), 520–525. DOI: 10.1002/zaac.201100453

93. Hilbers, M.; Läge, M.; Mattes, R. Preparation and structure of (Ph$_3$P)$_2$N[WSF$_5$]. *Inorg. Chim. Acta* **1992**, *201* (1), 1-3. DOI: 10.1016/S0020-1693(00)84992-0

94. Nieboer, J.; Haiges, R.; Hillary, W.; Yu, X.; Richardet, T.; Mercier, H. P. A.; Gerken, M. Fluoride-Ion Acceptor Properties of WSF$_4$: Synthesis, Characterization, and Computational Study of the WSF$_5^-$ and W$_2$S$_2$F$_9^-$ Anions and ^{19}F NMR Spectroscopic Characterization of the W$_2$OSF$_9^-$ Anion. *Inorg. Chem.* **2012**, *51* (11), 6350–6359. DOI: 10.1021/ic3005882.

95. Wollert, R.; Rentschler, E.; Massa, W.; Dehnicke, K. Chalkogeno-Fluoro-Wolframate. Die Kristallstrukturen von [Na-15-Krone-5]$_2$[WO$_2$F$_3$]$_2$ • 2 CH$_3$CN und [Na-15-Krone-5]$_2$[WOSF$_3$]$_2$ • 2 CH$_3$CN. *Z. Anorg. Allg. Chem.* **1991**, *596* (1), 121–132. DOI: 10.1002/zaac.19915960117.

96. Noble, A. M.; Winfield, J. M. Methoxypentafluorotungsten(VI) *J. Chem. Soc.*, Chem. Commun. **1969**, *4*, 151. DOI: 10.1039/c2969000151a

97. Handy, L. B.; Brinckman, F. E. Chemistry of the Methoxyfluorotungsten(vi) Series *J. Chem. Soc., Chem. Commun.* **1970**, *4*, 214–215. DOI: 100214.1039/c2970000214

98. Noble, A. M.; Winfield, J. M. Reactions of Tungsten Hexafluoride with Sulphite Esters and with Trimethyl Phosphite. Preparation and Reactions of Alkoxy- and Phenoxytungsten (VI) Pentafluorides. *J. Chem. Soc. A* **1970**, 501–506. DOI: 10.1039/j19700000501

99. Noble, A. M.; Winfield, J. M. Reactions of Tungsten Hexafluoride with Alkylalkoxy- and Alkylphenoxy-Silanes, Hexamethyldisiloxane, and Dimethyl EThер. *J. Chem. Soc. A* **1970**, *0*, 2574. DOI: 10.1039/j19700002574

100. Walker, D. W.; Winfield, J. M. The Fluorination of Methoxy-Groups by Tungsten Hexafluoride. *J. Inorg. Nucl. Chem.* **1972**, *34* (2), 759–762. DOI: 10.1016/0022-1902(72)80458-5.

101. Jacob, E. Metallhexamethoxide. *Angew. Chem., Int. Ed. Engl.* **1982**, *21* (S2), 317–330. DOI: 10.1002/anie.198203170

102. Walker, D. W.; Winfield, J. M. Reactions of Molybdenum Hexafluoride with Compounds Containing Methoxo Groups. *J. Fluorine Chem.* **1972**, *1* (3), 376–378. DOI: 10.1016/S0022-1139(00)83237-6

103. Quiñones, G. S.; Hägele, G.; Seppelt, K. MoF_6 and WF_6: Nonrigid Molecules? *Chem. Eur. J.* **2004**, *10* (19), 4755–4762. DOI: 10.1002/chem.200400095

104. Leitzke, O.; Sladky, F. Wolfram(VI)-fluorid-pentafluorotellurate(VI): $WF_n(OTeF_5)_{6-n}$. *Z. Anorg. Allg. Chem.* **1981**, *480* (9), 7–12. DOI: 10.1002/zaac.19814800902

105. Schröder, K.; Sladky, F. Molybdän(VI)-Fluorid-Pentafluorotellurate(vi) und Molybdän(vi)-Oxid-Fluorid-Pentafluorotellurate(vi): $MOF_n(OTeF_5)_{6-n}$ und $MoOF_n(OTeF_5)_{4-n}$. *Z. Anorg. Allg. Chem.* **1981**, *477* (6), 95–100. DOI: 10.1002/zaac.19814770611

106. Paine, R. T. Partial Hydrolysis of Rhenium and Osmium Hexafluorides. An Improved Synthesis and Characterization of Rhenium Oxide Tetrafluoride. *Inorg. Chem.* **1973**, *12* (6), 1457–1458. DOI: 10.1021/ic50124a060

107. Hoskins, B. F.; Linden, A.; O'Donnell, T. A. Controlled Hydrolysis of the Hexafluorides of Molybdenum, Tungsten and Rhenium: Structure of Oxonium (.Mu.-Fluoro)Bis(Tetrafluorooxotungstate(vi)). *Inorg. Chem.* **1987**, *26* (14), 2223– 2228. DOI: 10.1021/ic00261a012

108. Burns, R. C.; O'Donnell, T. A.; Waugh, A. B. A Specific Method for the Preparation of Many Transition Metal and Actinide Oxide Tetrafluorides. *J. Fluorine Chem.* **1978**, *12* (6), 505– 517. DOI: 10.1016/S0022-1139(00)81093-3

109. Paine, R. T.; McDowell, R. S. Gas-phase Composition and Structure of Metal Oxide Tetrafluorides. *Inorg. Chem.* **1974**, *13* (10), 2366–2370. DOI: 10.1021/ic50140a014.

110. Paine, R. T.; Ryan, R. R.; Asprey, L. B. Synthesis, Characterization, and Structure of Uranium Oxide Tetrafluoride. *Inorg. Chem.* **1975**, *14* (5), 1113–1117. DOI: 10.1021/ic50147a031

111. Christe, K. O.; Wilson, W. W.; Bougon, R. A. Synthesis and Characterization of CRF_4O, KrF_2•CrF_4O, and $NO^+CrF_5O^-$. *Inorg. Chem.* **1986**, *25* (13), 2163– 2169. DOI: 10.1021/ic00233a013.

112. Edwards, A. J.; Jones, G. R.; Steventon, B. R. The Crystal Structures of Tungsten, Molybdenum, Rhenium and Technetium Oxide Tetrafluorides. *Chem. Commun. (London)* **1967**, *9*, 462–463. DOI: 10.1039/C19670000462.

113. Edwards, A. J.; Jones, G. R. Fluoride crystal structures. Part I. Tungsten oxide tetrafluoride. *J. Chem. Soc. A* **1968**, 2074–2078. DOI: 10.1039/j19680002074

114. Mercier, H. P. A.; Breddemann, U.; Brock, D. S.; Bortolus, M. R.; Schrobilgen, G. Syntheses, Structures, and Bonding of NgF_2•$CrOF_4$, NgF_2•$2CrOF_4$ (Ng=Kr, Xe), and $(CrOF_4)_\infty$ *Chem. Eur. J.* **2019**, *25* (52), 12105–12119. DOI: 10.1002/chem.201902005

115. Edwards, A. J.; Steventon, B. R. Fluoride Crystal Structures. part II. Molybdenum Oxide Tetrafluoride. *J. Chem. Soc. A* **1968**, 2503. DOI: 10.1039/j19680002503

116. Arnaudet, L.; Bougon, R.; Ban, B.; Charpin, P.; Isabey, J.; Lance, M.; Nierlich, M.; Vigner, J. Preparation, Characterization, and Crystal Structure of the Adducts WOF_4•$_nC_5H_5N$ (n = 1, 2). *Inorg. Chem.* **1989**, *28* (2), 257–262. DOI: 10.1021/ic00301a020.

117. Levason, W.; Reid, G.; Zhang, W. Coordination Complexes of the Tungsten(VI) Oxide Fluorides WOF_4 and WO_2F_2 with Neutral Oxygen- and Nitrogen-donor Ligands. *J. Fluorine Chem.* **2016**, *184*, 50–57. DOI: 10.1016/j.jfluchem.2016.02.003

118. Levason, W.; Monzittu, F. M.; Reid, G.; Zhang, W.; Hope, E. G. Complexes of Molybdenum(VI) Oxide Tetrafluoride and Molybdenum(VI) Dioxide Difluoride with neutral N- and O-donor Ligands. *J. Fluorine Chem.* **2017**, *200*, 190–197. DOI: 10.1016/j.jfluchem.2017.06.015

119. Emsley, J. W.; Levason, W.; Reid, G.; Zhang, W.; De Luca, G. Phosphine and Diphosphine Complexes of Tungsten(VI) Oxide Tetrafluoride. *J. Fluorine Chem.* **2017**, *197*, 74–79. DOI: 10.1016/j.jfluchem.2017.02.007

120. Tucker, P. A.; Taylor, P. A.; Holloway, J. H.; Russell, D. R. The Adduct XeF_2•WOF_4 *Acta Crystallogr.* **1975**, *31* (3), 906–908. DOI: 10.1107/s0567740875004074

121. Holloway, J. H.; Schrobilgen, G. Fluorine-19 and Xenon-129 NMR Studies of the XeF_2•nWOF_4 and XeF_2•$MoOF_4$ (n = 1-4) Adducts: Examples of Nonlabile Xenon-Fluorine-Metal Bridges in Solution. *J. Inorg. Chem.* **1980**, *19* (9), 2632–2640. DOI: 10.1021/ic50211a031

122. Holloway, J. H.; Schrobilgen, G. The Preparation and Study by Raman Spectroscopy of KrF_2•MoF_4, XeF_2•MoF_4, and XeF_2•$2MoF_4$ (M = Molybdenum, Tungsten) and a Solution Fluorine-19 NMR Study of KrF_2•$nMoOF_4$ (N = 1-3) and KrF_2•WOF_4 *J. Inorg. Chem.* **1981**, *20* (10), 3363–3368. DOI: 10.1021/ic50224a043

123. Hope, E. G.; Jones, P. J.; Levason, W.; Ogden, J. S.; Tajik, M.; Turff, J. W. Characterization of Chromium(VI) Oxide Tetrafluoride, $CrOF_4$, and Caesium Pentafluoro-Oxochromate(VI) $Cs[CrOF_5]$. *J. Chem. Soc., Dalton Trans.* **1985**, *3*, 529–533. DOI: 10.1039/DT9850000529

124. Goettel, J. T.; Bortolus, M. R.; Stuart, D. G.; Mercier, H. P. A.; Schrobilgen, G. Chromium Oxide Tetrafluoride and Its Reactions with Xenon Hexafluoride; the $[XeF_5]^+$ and $[Xe_2F_{11}]^+$ Salts of the $[Cr^{VI}OF_5]^-$, $[Cr^{V}OF_5]^{2-}$, $[Cr^{V}_2O_2F_8]^{2-}$, and $[Cr^{IV}F_6]^{2-}$ Anions. *J. Chem. Eur. J.* **2019**, *25* (69), 15815–15829. DOI: 10.1002/chem.201903135

125. Bougon, R.; Bui Huy, T.; Charpin, P. Acid Properties of the Oxytetrafluorides of Molybdenum, Tungsten, and Uranium Toward Some Inorganic Fluoride Ion donors. *Inorg. Chem.* **1975**, *14* (8), 1822–1830. DOI: 10.1021/ic50150a016

126. Beuter, A.; Sawodny, W. Die Schwingungsspektren und Kraftkonstanten der Anionen $MoOF_5^-$ $MoOF_5^{2-}$, MoF_6^- und WOF_5^-. *Z. Anorg. Allg. Chem.* **1976**, *427* (1), 37–44. DOI: 10.1002/zaac.654270106

127. Kanatani, T.; Matsumoto, K.; Hagiwara, R. Syntheses and Physicochemical Properties of Low-Melting Salts Based on VOF_4^- and $MoOF_5^-$, and the Molecular Geometries of the Dimeric $(VOF_4^-)_2$ and $Mo_2O_4F_6^{2-}$ Anions. *Eur. J. Inorg. Chem.* **2010**, *2010* (7), 1049–1055. DOI: 10.1002/ejic.200901099

128. Matsumoto, K.; Hagiwara, R. A New Room Temperature Ionic Liquid of Oxyfluorometallate Anion: 1-Ethyl-3-Methylimidazolium Oxypentafluorotungstate ($EMImWOF_5$)' *J. Fluorine Chem.* **2005**, *126* (7), 1095–1100. DOI: 10.1016/j.jfluchem.2005.03.018

129. Kuhlmann, W.; Sawodny, W. The Preparation of Trioxo-Trifluororhenate (VII) and Oxopentafluororhenate (VI). *J. Fluorine Chem.* **1977**, *9* (5), 337–340. DOI: 10.1016/S0022-1139(00)82167-3

130. Massa, W.; Hermann, S.; Dehnicke, K. Reaktionen von Chloronitrenkomplexen des Molybdäns und Wolframs mit Silberfluorid Die Kristallstruktur von $AsPh_4[WOF_5]$ *Z. Anorg. Allg. Chem.* **1982**, *493* (1), 33–40. DOI: 10.1002/zaac.19824930105

131. Nuszhär, D.; Weller, F.; Dehnicke, K.; Hiller, W. Synthesen und Kristallstrukturen von [Na(15-Krone-5)]-$[NbF_5(NPPh_3)]$, $(PPh_3NH_2)[NbF_5(NPPh_3)]$ und $[Cs(15\text{-Krone-}5)_2](WOF_5)$ *J. Alloys Compd.* **1992**, *183*, 30– 44. DOI: 10.1016/0925-8388(92)90728-R

132. Mazej, Z.; Gilewski, T.; Goreshnik, E. A.; Jagličić, Z.; Derzsi, M.; Grochala, W. Canted Antiferromagnetism in Two-Dimensional Silver(II)

Bis[pentafluoridooxidotungstate(VI)] *Inorg. Chem.* **2017**, *56* (1), 224–233. DOI: 10.1021/acs.inorgchem.6b02034

133. Bortolus, M. R.; Mercier, H. P. A.; Schrobilgen, G. Group 6 Oxyfluoro-Anion Salts of $[XeF_5]^+$ and $[Xe_2F_{11}]^+$: Syntheses and Structures of $[XeF_5][M_2O_2F_9]$ (M=Mo, W), $[Xe_2F_{11}][M'OF_5]$ (M′=Cr, Mo, W), $[XeF_5][HF_2]\cdot CrOF_4$, and $[XeF_5][WOF_5]\cdot XeOF_4$ *J. Chem. Eur. J.* **2020**, *26* (41), 8935–8950. DOI: 10.1002/chem.202000826.

134. Turnbull, D.; Gerken, M. Crystal structure of an ordered $[WOF_5]^-$ salt: (1,10-phen-H)$[WOF_5]$ (1,10-phen = 1,10-phenanthroline). *Acta. Crystallogr. E* **2020**, *76* (8), 1345–1348. DOI: 10.1107/S2056989020009767

135. Crossman, M. C.; Fawcett, J.; Hope, E. G.; Russell, D. R. Crystal Structure of μ2-Hydridododecacarbonyltriosmiumdioxooctafluoro-μ2-fluoroditungsten. *J. Organomet. Chem.* **1996**, *514* (1–2), 87–91. DOI: 10.1016/0022-328x(95)06012-l

136. Stene, R. E.; Scheibe, B.; Karttunen, A. J.; Petry, W.; Kraus, F. Synthesis and Characterization of $A[W_2O_2F_9]$ (A = Li – Cs) *Eur. J. Inorg. Chem.* **2020**, *2020* (23), 2260–2269. DOI: 10.1002/ejic.202000289

137. Sakharov, S. G.; Kokunov, Y. V.; Gustyakova, M. P.; Buslaev, Y. A. Formation and structure of the $[WOF_6]^{2-}$ complex. *Dokl. Akad. Nauk SSSR* **1984**, *276* (1), 148–151.

138. Shorafa, H.; Ficicioglu, H.; Tamadon, F.; Girgsdies, F.; Seppelt, K. Molybdenum Difluoride Dioxide, MoO_2F_2. *Inorg. Chem.* **2010**, *49* (9), 4263–4267. DOI: 10.1021/ic1000864

139. Engelbrecht, A.; Grosse, A. V. Pure Chromyl Fluoride. *J. Am. Chem. Soc.* **1952**, *74* (21), 5262–5264. DOI: 10.1021/ja01141a007

140. Green, P. J.; Gard, G. L. Chemistry of Chromyl Fluoride. 5.1 New Preparative Routes to CrO_2F_2. *Inorg. Chem.* **1977**, *16* (5), 1243–1245. DOI: 10.1021/ic50171a055

141. Brown, S. D.; Green, P. J.; Gard, G. L. The Chemistry of Chromyl Fluoride III. Reactions with Inorganic Systems. *J. Fluorine Chem.* **1975**, *5* (3), 203–219. DOI: 10.1016/S0022-1139(00)82482-3

142. Laptash, N. M.; Udovenko, A. A. On the Identification of Oxygen and Fluorine Stoms in Disordered Inorganic Oxyfluoride Compounds. *J. Struct. Chem.* **2016**, *57* (2), 390–398. DOI: 10.1134/S0022476616020219.

143. Green, P. J.; Gard, G. L. The Chemistry of Chromyl Fluoride-6.[1] The Reaction of NO_2F and NOF with CrO_2F_2. *Inorg. Nucl. Chem. Lett.* **1978**, *14* (4–5), 179–182. DOI: 10.1016/0020-1650(78)80104-4

144. Veryasov, G.; Morozov, D.; Goreshnik, E.; Jesih, A. Synthesis and Crystal Structures of $(pyH)_2[Mo_2O_4F_6]$ and $(pipH_2)[Mo_2O_4F_6]$; Vibrational Band Assignment for

$[Mo_2O_4F_6]^{2-}$ Anion. *J. Fluorine Chem.* **2013**, *156*, 240–245. DOI: 10.1016/j.jfluchem.2013.10.012

145. Laurence, C. and Gal, J.–F. The BF_3 Affinity Scale. In *Lewis Basicity and Affinity Scales Data and Measurement*; John Wiley and Sons, Ltd., 2010; pp 85-109.

146. Wang, M.; Weyhermüller, T.; England, J.; Weighardt, K. Molecular and Electronic Structures of Six-Coordinate "Low-Valent" $[M(Mebpy)_3]^0$ (M = Ti, V, Cr, Mo) and $[M(tpy)_2]^0$ (M = Ti, V, Cr), and Seven-Coordinate $[MoF(Mebpy)_3](PF_6)$ and $[MX(tpy)_2](PF_6)$ (M = Mo, X = Cl and M = W, X = F). *Inorg. Chem.* **2013**, *52* (21), 12763-12776. DOI: 10.1021/ic402037e

Chapter 2 - Experimental

2.1. General Methods

2.1.1. Standard Techniques

CAUTION! *Hydrogen fluoride (HF) and F_2 are extremely toxic and corrosive materials. WF_6 releases HF upon exposure to even trace moisture. A rigorously anhydrous work environment and proper safety procedures must be implemented to ensure the safety of the user and their surroundings during the handling of these chemicals.*

The compounds synthesized, as well as many of the reagents used in their preparation, are highly moisture-sensitive and require rigorously anhydrous conditions to properly handle them. The majority of reactions were carried out in heat-sealed ¼"-o.d. FEP tubes were affixed to 316-stainless steel (Swagelok SS-1KF2) valves via flared fittings, sleeves and nuts (Figure 2.1). NMR tube scale reactions were carried out in a similar manner, instead utilizing fused ¼"-o.d./4-mm-o.d. FEP tubing. All reactors were dried under dynamic vacuum for ≥8 h prior to use. When WF_6 was employed as a reagent, the reactor was additionally passivated under ≥100 Torr of F_2 for ≥8 h prior to use.

Figure 2.1. A 316-stainless steel (Swagelok SS-1KF2) valve with a flared ¼"-o.d. FEP tube with nut and sleeve (top) and equipment used to fuse thick-walled ¼" to 4-mm FEP and create the flare (bottom).

Volatile materials that do not react with glass or generate HF upon exposure to moisture were handled on Pyrex vacuum lines equipped with grease-free PTFE stopcocks (J. Young or Chemglass) (Figure 2.2). The vacuum (~10^{-3} Torr) was monitored using thermocouple vacuum gauges (Varian, model 531) and was achieved using high-vacuum

pumps (Edwards RV8 or RV12). This vacuum was verified periodically with a mercury McLeod gauge (Labconco). Internal line pressures (0–1000 Torr) were measured using Be/Cu bourdon-tube pressure gauges (Heise, model CC or Ashcroft, model A4A). Volatile materials were captured in a liquid-N_2-cooled (–196 ºC) Pyrex trap. Reactors and distillation apparati were connected to the vacuum line using Ultra-Torr vacuum fittings (Swagelok) (Figure 2.3).

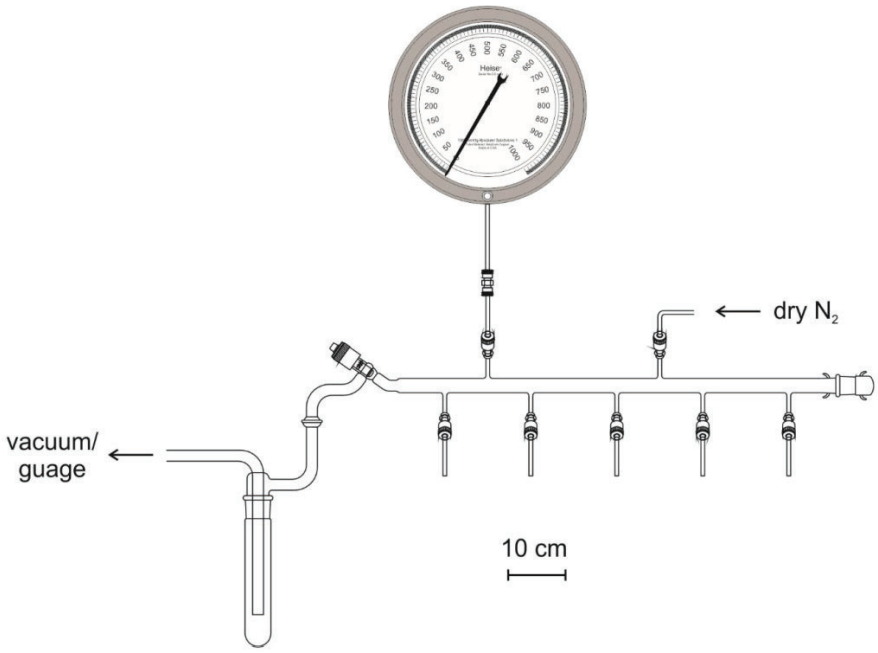

Figure 2.2. Pyrex vacuum line attached to a liquid-N_2-cooled (–196 ºC) Pyrex trap (top). Schematic of the vacuum line adapted from Jared Nieboer's M.Sc. thesis (2007, University of Lethbridge, bottom).

Figure 2.3. Ultra-Torr vacuum fittings (Swagelok) (top) PTFE vacuum fittings (Swagelok) (bottom) partially disassembled.

Elemental F_2 and volatile binary fluorides were handled on a nickel/316-stainless-steel vacuum line equipped with 316-stainless-steel valves and fittings (Autoclave 55 Engineers) (Figure 2.4). Absolute capacitance manometers (MKS Baratron, type 626 , 0–10 or 0–1000 Torr) were used to monitor the vacuum (~10^{-3} Torr) and internal line pressures (0–1000 Torr). Elemental F_2 and HF were passed through a stainless-steel cylinder (75 cm, 17-cm o.d.) containing soda lime (EMD, 4 mesh; labeled "rough vacuum") to scrub the gasses. Traces of these gasses (< 1 Torr) were scrubbed by passing them through a smaller stainless-steel cylinder (30 cm) containing activated charcoal (labeled "fine vacuum"). FEP reactors were connected to the line using PTFE vacuum fittings (Swagelok) (Figure 2.3, above).

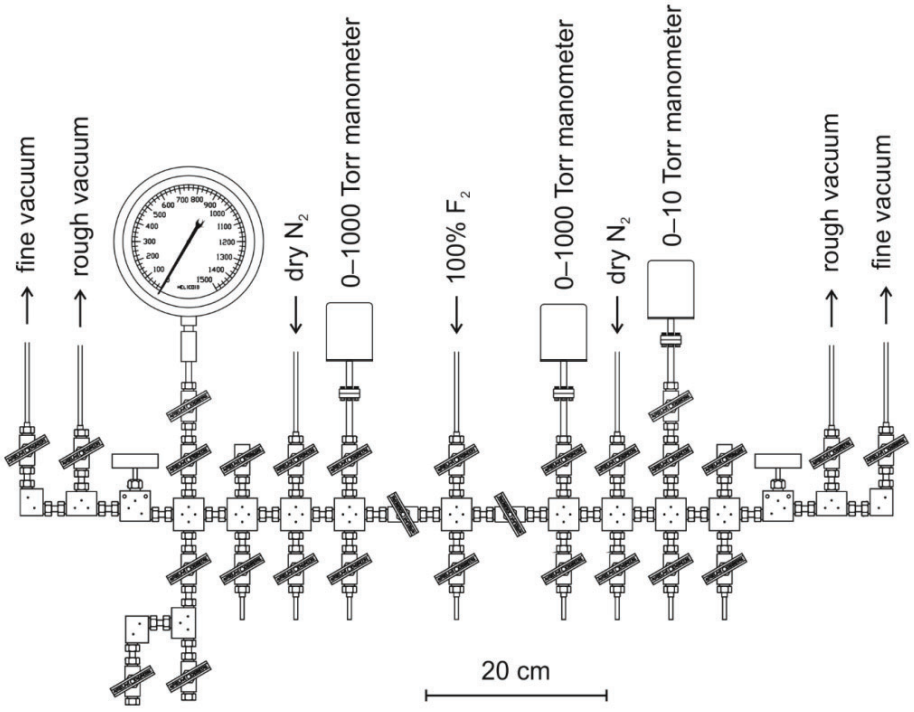

Figure 2.4. Nickel/316-stainless-steel (Autoclave Engineers) vacuum line, equipped with absolute capacitance manometers (MKS Baratron, type 626, 0–10 or 0–1000 Torr) (top). Schematic of the vacuum line adapted from Jared Nieboer's M.Sc. thesis (2007, University of Lethbridge, bottom).

Solid materials were handled in a dry box (OmniLab, Vacuum Atmospheres) under an atmosphere of N_2 (Figure 2.5). Quality of the atmosphere was periodically verified by exposing potassium metal to the dry box atmosphere. Volatile materials were frozen in the dry box using an evacuated cold well containing copper BBs that were cooled externally using liquid N_2 to achieve temperatures $\leq$–100 ºC. The copper BBs would be poured into a stainless steel Dewar wherein a reactor would be placed to be subsequently charged with solid reagents.

Figure 2.5. OmniLab, Vacuum Atmospheres dry box filled with a N_2 atmosphere and equipped with cold well filled with Cu BBs.

Vacuum distillations were enabled by connecting reactors to either the nickel/316-stainless-steel or Pyrex vacuum line, evacuating and cooling the vessels to –196 ºC with liquid N_2 prior to the distillation. Long-term, low-temperature storage (hours to weeks) was achieved using an anhydrous C_2H_5OH bath that was kept between –30 and –80 °C (Thermo NESLAB, CC-100) and verified with a Greisinger electronic digital thermometer (Figure 2.6).

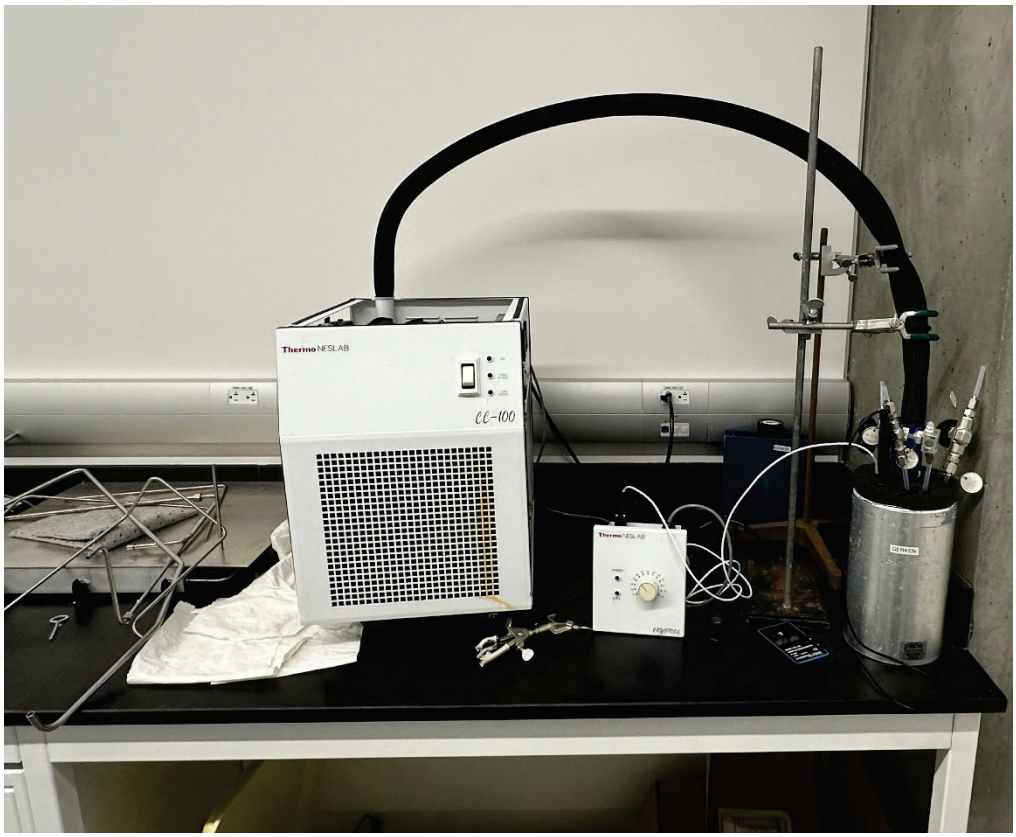

Figure 2.6. Thermo NESLAB, CC-100 immersion cooler (left) and attached C_2H_5OH bath (right).

2.1.2. Raman Spectroscopy

Raman spectra were recorded at ambient temperatures using a Bruker RFS-100 Raman spectrometer with a Nd:YAG laser (1064-nm line) that was used for excitation of

the sample, and backscattered (180°) radiation was sampled. The spectrometer was outfitted with a quartz beam splitter and liquid-N_2 cooled germanium detector (Figure 2.7), the power of which was often 150 mW, with a usable Stokes range of the collected data being 85-3500 cm^{-1} at a spectral resolution of 2 cm^{-1}.

Figure 2.7. Bruker RFS-100 Raman spectrometer outfitted with a quartz beam splitter and liquid-N_2 cooled germanium detector.

Spectra of samples were typically recorded in FEP reactors at ambient temperatures on a low-temperature stage. The apparatus was then covered with a black velveteen cloth to absorb the scattered laser light and block outside light from getting into the sample chamber. Compounds that did not react with glass were also recorded in melting point capillaries at ambient temperatures. The melting point capillaries were dried in an oven at

140 °C for ~16 h and transferred hot into the dry box antechamber which was then immediately evacuated. The samples were prepared by charging the melting point capillaries in the dry box and then sealing them with Kel-F grease before being removed from the dry box. These samples were then flame-sealed under the internal atmosphere of N_2 using a Bunsen burner.

2.1.3. NMR Spectroscopy

Variable temperature NMR spectra were recorded using a Bruker Avance II spectrometer (7.05 T; 300.16 MHz for ^{1}H, 282.43 MHz for ^{19}F, 121.51 MHz for ^{31}P, 75.48 MHz for ^{13}C) equipped with a 5-mm BBFO probe and referenced externally to $CFCl_3$ (^{19}F), $Si(CH_3)_4$ (^{1}H and $^{13}C\{^{1}H\}$), or 85% H_3PO_4 (^{31}P) at 20 °C.

Samples were prepared by heat sealing the fused ¼”-o.d./4-mm-o.d. FEP reactors under dynamic vacuum whose contents were frozen in liquid N_2 at –196 ºC. These samples were then sheathed in 5-mm-o.d. glass tubes and run unlocked between –80 ºC and 22 ºC with a relaxation delay of 5 seconds. Temperatures between 22 ºC and –50 ºC were achieved using a BCU unit. Temperatures below –50 ºC were achieved using a resistive liquid N_2 boiler with the cold N_2 gas passing over the sample.

Spectra were processed using MestreNova (version 6.0)[(1)] and Top Spin (version 2.1, 4.0).[(2)]

2.14. X-ray Crystallography

2.1.4.1. Crystal Growth and Mounting

All crystals were grown from solutions and isolated in their ¼”-o.d. FEP reactors. The reactors were then cut and emptied onto an aluminum trough positioned in a mirrored-

glass Dewar sleeve, the temperature of which was kept between –40 and –80 °C by passing N_2 gas through a 10.5-L Dewar of liquid N_2 (Figure 2.8). The quality of the crystals was evaluated using an Olympus SZ61microscope. The crystals were affixed to a cryoloop before being quickly transferred and affixed to a goniometer head. In the case of $[WF_5(terpy)][WF_7]•SO_2$, the crystals were enclosed in cryotongs that were cooled to –196 ºC prior to being transferred to the goniometer in order to lessen the amount of SO_2 that escaped. In all cases, the goniometer was pre-cooled to –173 ºC.

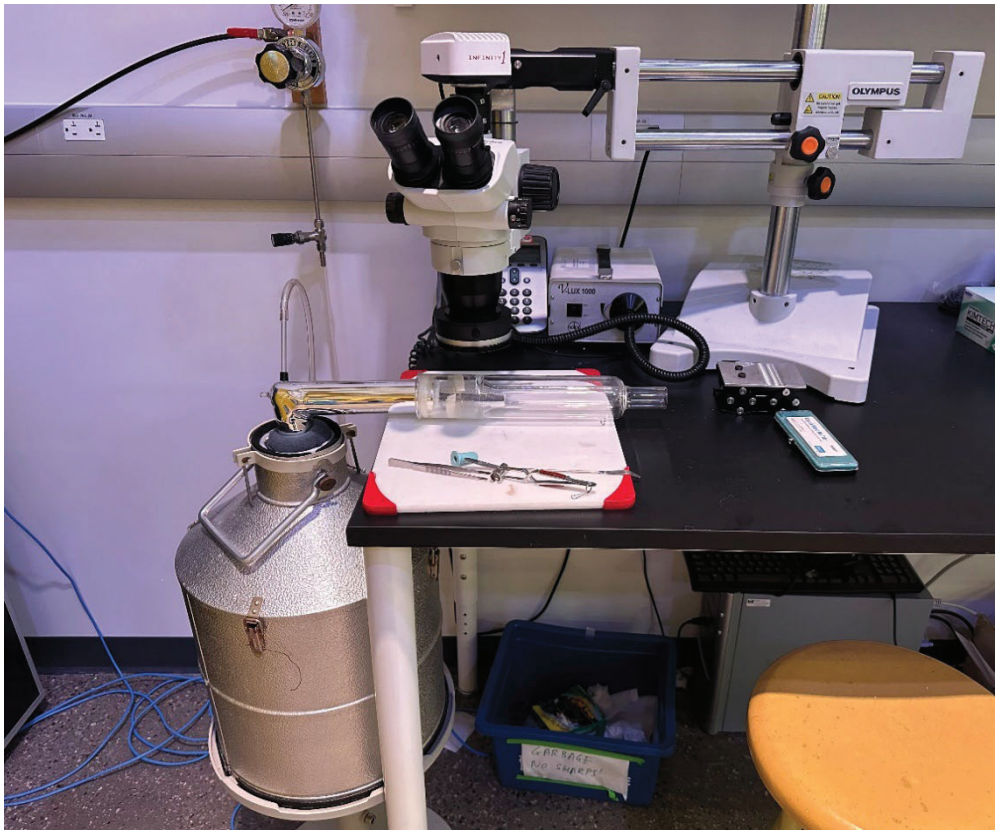

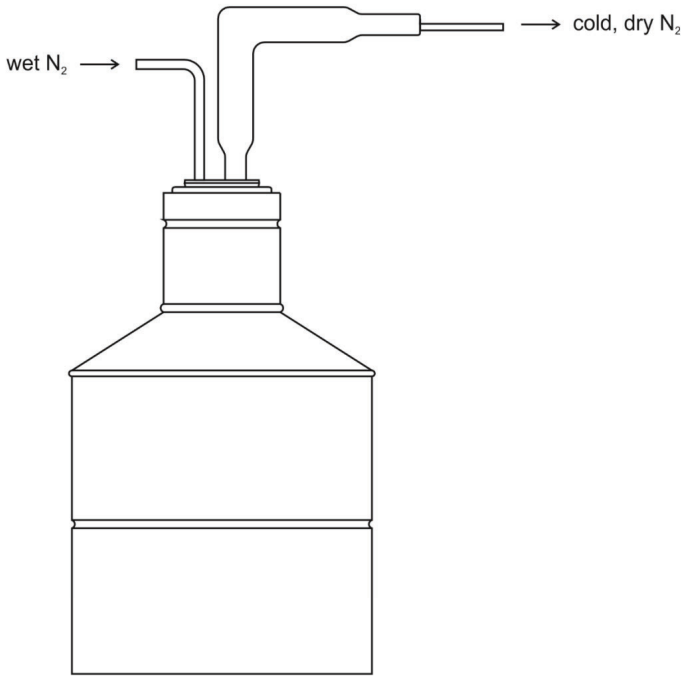

Figure 2.8. The 10.5-L Dewar is equipped with a glass N_2 inlet, mirrored-glass Dewar sleeve, and aluminium trough (top). Schematic of the low-temperature crystal-mounting apparatus adapted from Jared Nieboer's M.Sc. thesis (2007, University of Lethbridge).

2.1.4.2. Data Collection and Reduction.

Crystals were centered on a Rigaku SuperNova diffractometer equipped with a Dectris Pilatus 3R 200K-A hybrid-pixel-array detector, a four-circle κ goniometer, an Oxford Cryostream 800, and sealed MoKα and CuKα X-ray sources (Figure 2.9). Data were collected using a MoKα source (λ = 0.71073 Å) at −173 °C. Crystals were screened once again for quality and underwent a pre-experiment to determine the unit cell, and intensity of the preliminary data to determine a proper data collection strategy. This strategy was optimised to collect five-fold redundant data at a resolution of 0.77 Å. The data were processed using CrysAlisPro[3] to apply the necessary Lorentz and polarisation corrections to the integrated and scaled data. A numerical (Gaussian-grid) absorption correction was generated based upon the indexed faces of the crystal.

Figure 2.9. Rigaku SuperNova diffractometer equipped with a Dectris Pilatus 3R 200K-A hybrid-pixel-array detector, a four-circle κ goniometer, an Oxford Cryostream 800, and sealed MoKα and CuKα X-ray sources.

2.1.4.3. Structure Solution and Refinement

Atom positions were determined using the intrinsic phasing method (ShelXT)[4] and were refined using least-squares refinement method (ShelXL).[5] Non-hydrogen atoms were refined anisotropically and recommended weights for the atoms were determined before hydrogen atoms were introduced using a riding model (HFIX). The maximum and minimum electron density in the difference Fourier maps were located near the tungsten atom in all cases. Structure solution and refinement were performed with the aid of Olex2 (version 1.5).[6] Compounds whose structures have been elucidated and used in this thesis are given in Table 2.1 alongside their internal code.

Table 2.1. Elucidated crystal structures with their corresponding internal code.

Compound	Internal Code
$WF_6(NC_5H_5)\{P(CH_3)_3\}\bullet CH_2Cl_2$	MG 22004
$[WF_5(terpy)][WF_7]\bullet SO_2$	MG 23016b
$F_2P(C_6H_5)_3$	MG 23003

2.2. Preparation and Purification of Reagents

2.2.1. Fluorine and Binary Fluorides

Elemental F_2 (Linde, 100%) was used without further purification. Hydrogen fluoride (Air Products, 99.9%) was dried under an atmosphere of F_2 for ~2 weeks before being distilled onto $K_2[NiF_6]$ (Fluka). Meanwhile, WF_6 (Elf Atochem) and SbF_5 (Ozark-Mahoning) were purified by distillation.

2.2.2. Common Solvents

Sulfur dioxide (Praxair) was purified by a distillation onto CaH_2 before being distilled into another bulb containing fresh CaH_2. A solvent purification system (M. Braun MB-SPS) was used to dry dichloromethane over 3-Å molecular sieves before being distilled into another bulb containing fresh sieves. Acetonitrile, meanwhile, was distilled onto P_4O_{10} and 4-Å molecular sieves.

2.2.3. Volatile Bases

Pyridine (Sigma-Aldrich, 99.8%) was dried over 3-Å molecular sieves and distilled onto fresh sieves. Trimethylphosphine was gifted from Dr. Paul G. Hayes and further purified by distillation onto 3-Å molecular sieves.

2.2.4. Solid Bases

The phosphine oxides $OPPh_3$ (Thermo Scientific, 99%) and $OPEt_3$ (Thermo Scientific, 97%) were used as is after purity was evaluated via multinuclear NMR spectroscopy. Meanwhile, 2,2′:6′,2′′-terpyridine (Sigma Aldrich, 98%) was initially purified by sublimation at 3×10^{-3} Torr and 90 °C for 4 h; however, subsequent chemistry used the unpurified reagent without any adverse effects.

2.2.5. Main-Group and Transition-Metal Fluoride Adducts

The $WF_6(NC_5H_5)$ adduct was prepared by reacting WF_6 with an equimolar amount of C_5H_5N in CH_2Cl_2 as previously described.[7] Meanwhile, the $SbF_5 \bullet SO_2$ adduct was prepared via dissolving SbF_5 in excess SO_2, followed by removal of volatiles at RT under dynamic vacuum.[8]

2.3. Synthesis and Crystal Growth

2.3.1. Lewis Acid Behaviour of WF_6 Towards Mixed Ligand Systems

2.3.1.1. Reaction of $WF_6(NC_5H_5)$ with $P(CH_3)_3$ in CH_2Cl_2

General procedure: A ¼'' o.d. FEP reactor was charged with the $WF_6(NC_5H_5)$ adduct (1 equiv. *e.g.*: 0.032 g, 0.085 mmol). Subsequently, CH_2Cl_2 (*e.g.*: 0.639 g) was added via vacuum distillation, followed by agitation at room temperature to form a clear colourless solution. The base, $P(CH_3)_3$ (~0.94 - 1.26 equiv., *e.g.*: 0.006 g, 0.08 mmol), was distilled then onto the frozen solution at –196 °C. This initially resulting in a clear orange layer at the interface upon melting. Agitation of the reactor resulted in a clear orange solution. The reactor was then left in the cryobath at ~ −40 °C for 16 h. Orange crystals were observed at this time. Volatiles were then removed from the reactor at low temperatures (~−50 °C for 4 h) followed by further removal at ambient temperatures for 30 min to obtain an orange powder in a near stoichiometric yield with respect to $WF_6(NC_5H_5)\{P(CH_3)_3\}$.

2.3.1.2. $WF_6(NC_5H_5)\{P(CH_3)_3\}\bullet CH_2Cl_2$ Crystal Growth

A ¼'' o.d. FEP reactor was charged with $WF_6(NC_5H_5)$ (0.071 g, 0.019 mmol) followed by vacuum distillation of both CH_2Cl_2 (0.545 g) and $P(CH_3)_3$ (0.015 g, 0.012 mmol) onto it. This immediately resulted in an orange solution at the interface and a yellow solution further below. Further agitation resulted in a homogenous orange solution. Orange plates were grown from the mother liquor at −40 °C over 16 h.

2.3.2. Exploration of Phosphine Oxides Ligands to WF_6

2.3.2.1. Reaction of WF_6 with $OP(C_2H_5)_3$ in CH_2Cl_2

A ¼'' o.d. FEP reactor was charged with WF_6 (0.038 g, 0.013 mmol) via vacuum distillation and was subsequently brought into the dry box where it was frozen at −127.5 °C. The reactor was then charged with $OP(C_2H_5)_3$ (0.0160 g, 0.0119 mmol) inside the dry box after which the reactor was brought out and attached to the glass line. Dichloromethane (0.408 g) was vacuum distilled onto the mixture. The reactor was then placed into a cyrobath at −38 °C for 16 h. Volatile materials were initially removed at −75 °C, however, the sample was allowed to gradually warm to −26 °C over the course of 5.5 h. The reactor was then briefly agitated followed by an additional 30 min at ambient temperature to ensure all volatile materials were removed. The clear, colourless oil was recovered at a 97 % yield (0.050 g) based on quantitative $WF_6\{OP(C_2H_5)_3\}$ formation.

2.3.2.2. Reaction of WF_6 with $OP(C_6H_5)_3$ in CH_3CN

A ¼'' o.d. FEP reactor was charged with WF_6 (0.049 g, 0.017 mmol) which was then brought into the dry box and frozen at −125 °C. The reactor was then charged with $OP(C_6H_5)_3$ (0.0424 g, 0.0152 mmol) inside the dry box, and CH_3CN (0.081 g) was vacuum distilled onto it on a vacuum line. Agitation at ambient temperature resulted in a white precipitate crashing out of solution. The reactor was then placed into a cryobath at −40 °C for 16 h. The reactor was cooled to −80 °C and volatile materials were removed under dynamic vacuum allowing the sample to gradually warm to −30 °C over the course of 5 h. The reactor was then warmed to ambient temperatures at which temperatures volatiles were

removed for an additional 30 min. The white powder was recovered at a 111% yield (0.097 g) based on quantitative $WF_6\{OP(C_6H_5)\}$ formation.

2.3.2.3. $F_2P(C_6H_5)$ Crystal Growth

A ¼'' o.d. FEP reactor was charged with 0.010 g of the white powder recovered from the reaction in Chapter 2.3.2.2. and was dissolved in *ca.* 0.050 g (20 Torr of pressure in the glass vacuum line) of CH_2Cl_2, placed in a cryobath at −35 °C for 16 h and stored for an additional 72 h.

2.3.3. Lewis Acidity of WF_6 Towards Tridentate Terpyridine

2.3.3.1. $[WF_5(terpy)][WF_7]$

Inside the dry box, a ¼'' o.d. FEP reactor was charged with 2,2′:6′,2′′-terpyridine (0.0254 g, 0.0109 mmol. After passivating the connection on the metal line for 16 h, WF_6 (0.101 g, 0.0338 mmol) was distilled onto terpy. The reactor was then placed into an ethanol bath at −100 °C and connected to a glass line. The solvent, SO_2 (0.617 g), was then distilled onto the mixture. Warming the reactor to ambient temperature, followed by agitation, resulted in a clear, red solution. The reactor was then placed into a cryobath at −40 °C for 16 h. Volatiles were removed initially at −60 °C, allowing it to warm to −40 °C over a course of 1 h, then at ambient temperature for 30 min, yielding $[WF_5(terpy)][WF_7]$ (0.090 g, 0.011 mmol) as an orange powder in 99.7% yield.

NMR (ppm, SO_2, 22 °C, unlocked): $\delta(^{19}F)$ 148.6 (s, $[WF_7]^-$), 145.3 (s, $[WF_5(terpy)]^+$, $^1J_{W-F}$ = 21 Hz). The sample contained traces of $[W_2O_2F_9]^-$ (F_{term}: (d) 65 ppm, $^2J_{F-F}$ 58 Hz, $^1J_{W-F}$ = 70 Hz; resonance for $F_{br.}$ is not observed because of its expected low intensity) and $[WOF_5]^-$ ($F_{eq.}$: 58 ppm, $^2J_{F-F}$ = 52 Hz, $^1J_{W-F}$ = 71 Hz; resonance for $F_{ax.}$

is not observed because of its expected low intensity). δ(^{1}H) 10.14 (d, H6/H6′′, 5.99 Hz), 9.45 (dd, H4′, 8.00 Hz, 7.87 Hz), 9.28 (d, H3′/H5′ 7.95 Hz), 9.20-9.14 (m, H4/H4′′ and H3/H3′′), 8.76-8.68 (m, H5/H5′′). Atom labels are in accordance to Figure 2.10.

NMR (ppm, SO_2, −35 °C, unlocked): δ(^{13}C{^{1}H}) 156.9 (s, C4′), 150.6 (s, C2/C2′′), 150.3 (s, C2′/C6′), 148.3 (s, C4/C4′′), 145.2 (s, C6/C6′′), 131.0 (s, C3′/C5′), 126.1 (s, C3/C3′′), 125.7 (s, C5/C5′′). Atom labels are in accordance to Figure 2.10.

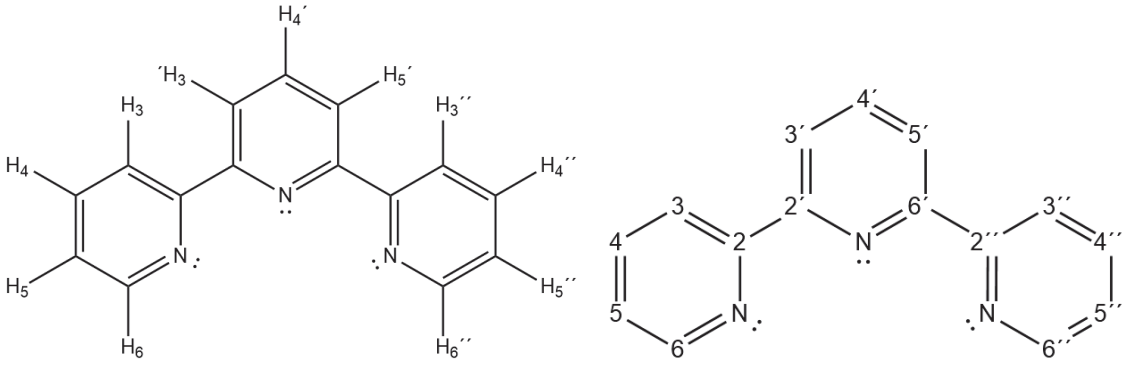

Figure 2.10. Numeric classification of proton (left) and carbon (right) for terpy.

2.3.3.2. [WF_5(terpy)][WF_7]•SO_2 Crystal Growth

A ¼'' o.d. FEP reactor was charged with [WF_5(terpy)][WF_7] (0.0538 g, 0.0649 mmol), followed by vacuum distillation of *ca.* 0.283 g SO_2 (150 Torr of pressure in the glass vacuum line). The reactor was then placed onto the metal line to passivate the connection over 16 h. During this time, red crystals formed above the solvent line. The solvent was removed at −55 °C to reduce to half of its original volume with the crystals then knocked into the solution to act as seeds to further encourage crystal growth. Orange plates were grown at −45 °C over the course of 16 h.

2.3.3.1. $[WF_5(terpy)][SbF_6]$

Inside the dry box, a ¼'' o.d. FEP reactor was charged with $[WF_5(terpy)][WF_7]$ (0.0556 g, 0.0671 mmol) and cooled to −100 °C, followed by addition of SbF_5SO_2 (0.0191 g, 0.0680 mmol). The reactor was maintained at −100 °C and *ca.* 0.283 g of SO_2 (150 Torr of pressure in the glass vacuum line) was vacuum distilled onto the reaction mixture. Upon warming to ambient temperature, a clear, red solution formed, which was placed into a cryobath at −42 °C for 16 h. Volatiles were removed at −60 °C over 3 h, then at ambient temperature for 30 min, to yield $[WF_5(terpy)][SbF_6]$ as an orange powder (0.048 g, 0.059 mmol) in a yield of 95.7%.

NMR (ppm, SO_2, 22 °C, unlocked): $\delta(^{19}F)$ 145.6 (s, $[WF_5(terpy)]^+$). The sample contained trace peaks of free WF_6 at 167 ppm (s, 43 Hz), $WOF_4(OSO)$ (s, 74 ppm), $[W_2O_2F_9]^-$ ($F_{term.}$: 67.0 ppm, $^2J_{F-F}$ = 58 Hz; resonance for $F_{br.}$ is not observed because of its expected low intensity), $[WOF_5]^-$ ($F_{eq.}$: (br. d) 63.0 ppm, $^2J_{F-F}$ = 58 Hz; resonance for $F_{ax.}$ is not observed because of its expected low intensity), and unknown impurity at and 46 ppm. $\delta(^1H)$ 10.22 (d, H6/H6′′, 6.01 Hz), 9.51 (dd, H4′, 8.03 Hz, 7.88 Hz), 9.34 (d, H3′/H5′ 8.05 Hz), 9.26-9.23 (m, H4/H4′′ and H3/H3′′), 8.83-76 (m, H5/H5′′). Trace impurities at 10.49 (br. d, 6.38 Hz), 9.71 (t, 6.35 Hz), 9.46 (s), 9.39 (s), and 8.93-8.86 (m) are present and are presumed to be a $[H_1terpy]^+$ species.

NMR (ppm, SO_2, −35 °C, unlocked): $\delta(^{13}C\{^1H\})$ 157.0 (s, C4′), 150.7 (s, C2/C2′′), 150.3 (s, C2′/C6′), 148.4 (s, C4/C4′′), 145.3 (s, C6/C6′′), 131.1 (s, C3′/C5′), 126.1 (s, C3/C3′′), 125.7 (s, C5/C5′′). Trace impurities at 146.9, 127.2, 126.5, and 126.3 are present and are presumed to be a $[H_{1-3}terpy]^+$ species. Atom labels are in accordance to Figure 2.10.

2.4. Computational Methods

In Chapters 3 and 5, the B3LYP functional, as implemented in Gaussian 22 (revision D.01) was employed.[9] All calculations were performed by Felix O'Donnell.[10] The Stuttgart basis set[11] augmented by one f-type polarisation function ($\alpha f = 0.823$)[12] and associated relativistic pseudopotentials were used for tungsten, whereas the aug-cc-pVTZ basis sets were used for the lighter atoms referred to as aVTZ unless otherwise noted.

Geometries were optimised in the gas phase and vibrational frequencies were calculated on the optimised geometries. In the case of $WF_6(NC_5H_5)\{P(CH_3)_3\}\bullet CH_2Cl_2$, the geometry determined by X-ray crystallography was used as a starting point. Meanwhile, the $[WF_5(terpy)]^+$ cation was optimized using a square antiprismatic geometry as the starting position. Excellent agreement was observed between experimental and calculated geometries and frequencies in all cases. GaussView (version 6.0) was used to visualise vibrational modes and aid in their description with NBO analyses were performed using NBO (version 6.0).[13-14]

2.5. References

1. Forezi, L. S. M.; Castelo-Branco, F. S. Editing NMR spectra with MestReNova software: A practical guide. *Rev. Virtual Quim.* **2017**, *9* (6), 2650-2672.

2. Top spin version 2.1, patch level 8, (©2009 Bruker BioSpin)

3. CrysAlisPro. Agilent Technologies, Ltd.: Yarnton, Oxfordshire, England **2014**.

4. Sheldrick, G. M. SHELXT – Integrated Space-Group and Crystal Structure Determination. *Acta Crystallogr. A* **2015**, *71* (1), 3–8. DOI: 10.1107/S2053229614024218

5. Sheldrick, G. M. Crystal Structure Refinement with SHELXL. *Acta Crystallogr. C* **2015**, *71* (1), 3–8. DOI: 10.1107/S2053273314026370

6. Dolomanov, O. V.; Bourhis, L. J.; Gildea, R. J.; Howard, J. A. K.; *Olex2,* ver. 1.5; Puschmann, OlexSys Ltd., Durham University: England, **2024**

7. Arnaudet, L.; Bougon, R.; Buu, B.; Lance, M.; Nierlich, M.; Thuéry, P.; Vigner, J. Characterization of the Adducts WF_6•py and WF_6•2py (py = pyridine): Crystal Structure of WF_6•2py. *J. Fluorine Chem.* **1995**, *71* (1), 123–129. DOI: 10.1016/0022-1139(94)03160-2

8. Minkwitz, R.; Molsbeck, W.; Preut, H. Z. Kristallstruktur von $SbF_5 \cdot SO_2$ / Crystal Structure of $SbF_5 \bullet SO_2$. *Naturforsch. B* **1989**, 44 (12), 1581–1583.

9. Frisch, M. J.; Trucks, G. W.; Schlegel, H. B.; Scuseria, G. E.; Robb, M. A.; Cheeseman, J. R.; Scalmani, G.; Barone, V.; Petersson, G. A.; Nakatsuji, H.; Li, X.; Caricato, M.; Marenich, A.; Bloino, J.; Janesko, B. G.; Gomperts, R.; Mennucci, B.; Hratchian, H. P.; Ortiz, J.V.; Izmaylov, A. F.; Sonnenberg, J. L.; Williams-Young, D.; Ding, F.; Lipparini, F.; Egidi, F.; Goings, J.; Peng, B.; Petrone, A.; Henderson, T.; Ranasinghe, D.; Zakrzewski, V. G.; Gao, J.; Rega, N.; Zheng, G.; Liang, W.; Hada, M.; Ehara, M.; Toyota, K.; Fukuda, R.; Hasegawa, J.; Ishida, M.; Nakajima, T.; Honda, Y.; Kitao, O.; Nakai, H.; Vreven, T.; Throssell, K.; Montgomery, J. A., Jr.; Peralta, J. E.; Ogliaro, F.; Bearpark, M.; Heyd, J. J.; Brothers, E.; Kudin, K. N.; Staroverov, V.N.; Keith, T.; Kobayashi, R.; Normand, J.; Raghavachari, K.; Rendell, A.; Burant, J. C.; Iyengar, S. S.; Tomasi, J.; Cossi, M.; Millam, J. M.; Klene, M.; Adamo, C.; Cammi, R.; Ochterski, J. W.; Martin, R. L.; Morokuma, K.; Farkas, O.; Foresman, J. B.; Fox, D. J. Gaussian 09,rev. D.01; Gaussian, Inc.: Wallingford, CT, **2016**.

10. O'Donnell, F. Unpublished work.

11. Andrae, D.; Häußermann, U.; Dolg, M.; Stoll, H.; Preuß, H. Energy-Adjusted *ab initio* Pseudopotentials for the Second and Third Row Transition Elements. *Theor. Chim. Acta* **1990**, *77* (2), 123–141. DOI: 10.1007/bf01114537.

12. Ehlers, A. W.; Böhme, M.; Dapprich, S.; Gobbi, A.; Höllwarth, A.; Jonas, V.; Köhler, K. F.; Stegmann, R.; Veldkamp, A.; Frenking, G. A set of f-polarization functions for pseudo-potential basis sets of the transition metals Sc, Cu, Y, Ag and La, Au. *Chem. Phys. Lett.* **1993**, *208* (1–2), 111–114. DOI: 10.1016/0009-2614(93)80086-5.

13. GaussView, ver. 6.0; Gaussian, Inc.: Wallingford, CT, **2016**.

14. Glendening, E. D.; Badenhoop, J. K.; Reed, A. E.; Carpenter, J.E.; Bohmann, J. A.; Morales, C. M.; Landis, C. R.; Weinhold, F. NBO, ver. 6.0; Theoretical Chemistry Institute, University of Wisconsin:Madison, WI, **2013**.

Chapter 3 – Lewis-Acid Behaviour of WF_6 Towards Mixed Ligand Systems

3.1. Introduction:

Tungsten hexafluoride has been known to form neutral adducts with monodentate pnictogen bases. This has led to the isolation and characterization of various hepta- and octa-coordinate species utilizing monodentate ligands over the years. Tebbe and Muetterties were the first to synthesize $WF_6\{N(CH_3)_3\}$, as well as $WF_6(py)_n$, n = 1,2 in 1968, as evidenced by NMR spectroscopy. The crystal structure of $WF_6(py)_2$ was later characterized by Bougon *et al.* in 1995 showing a bicapped trigonal prismatic molecular geometry.[1-2] Bougon *et al.* were also able to isolate the 1 : 1 adduct of WF_6(F-py) in 1993 with the crystal structure possessing a capped trigonal prismatic geometry.[3] Seppelt *et al.* further expanded the field in 2010, isolating both $WF_6\{P(CH_3)_3\}$ and $WF_6\{P(C_6H_5)(CH_3)_2\}$. Whereas the trimethylphosphine adduct retained a capped trigonal prismatic geometry, the latter adduct was found to possess a capped octahedral geometry, making it currently the only known WF_6 adduct with a neutral mono-dentate base that deviates from a capped trigonal prism.[4] The group stated that this was further proof that hepta-coordinate geometries must be similar in energy, bolstering Muetterties' and Wright's initial claim from 1967.[5] To further investigate this claim, Gerken *et al.* examined adducts with various substituted pyridines whose structures were optimized using DFT methods and fond that the capped trigonal prismatic structures were uniformly preferred.[6] Similar to the three hepta-coordinate geometries, *i.e.*, pentagonal bipyramidal, mono-capped trigonal prismatic and mono-capped octahedral, octa-coordinate species can

adopt various geometries, *i.e.*, square antiprismatic, bicapped trigonal prismatic or trigonal dodecahedral geometries. This is best exemplified with the 1 : 2 adduct of $WF_6(py)_2$ adopting a bicapped trigonal prismatic geometry, whereas the 1 : 1 adducts of $WF_6(L)$ (L = phen, bipy) possess distorted trigonal dodecahedral geometries. To date, however, there are no reports of neutral WF_6 adducts with two different types of Lewis bases, nor the resulting effect of their different basicities and steric demands on structure.

In this chapter, the synthesis, structural characterization, and reactivity of octa-coordinate WF_6 adducted with one equivalent of pyridine and one equivalent of trimethylphosphine are detailed. Additionally, the structure of new $WF_6(py)\{P(CH_3)_3\}$ has been elucidated by X-ray crystallography; vibrational and NMR spectroscopy were used to characterize the reaction products, detailed below. DFT geometry optimization and calculations of the vibrational frequencies at the B3LYP level of theory supported the experimental findings.

3.2. Results and Discussion:

3.2.1. Syntheses and Properties of $WF_6(py)\{P(CH_3)_3\}$

The $WF_6(py)\{P(CH_3)_3\}$ adduct was prepared by vacuum distilling $P(CH_3)_3$ onto $WF_6(py)$ dissolved in CH_3CN at a near 1 : 1 ratio, producing a clear orange solution (Eq. 3.1). The $WF_6(py)$ precursor can be made via the simple addition of pyridine to WF_6 dissolved in CH_3CN at a 1 : 1 ratio and was chosen due to the stronger Lewis-basicity of the ligand (Eq. 3.2).[7] It was surmised that this stepwise synthesis would prevent ligand competition at the metal centre as the weaker $P(CH_3)_3$ ligand would not displace the pyridine ligand. The reaction, however, is not as simple basic addition reaction, with a

variety of side products were identified (See 3.2.3 Multinuclear NMR Spectroscopy). The solvent and volatiles were removed under dynamic vacuum at low temperatures (*ca.* –50 °C) and allowed to warm up to 30 °C resulting in an orange powder.

$$WF_6(py) + P(CH_3)_3 \rightarrow WF_6(py)\{P(CH_3)_3\} \quad (3.1)$$

$$WF_6 + py \rightarrow WF_6(py) \quad (3.2)$$

The powder is soluble in CH_2Cl_2, but reacts with SO_2, forming a clear beige solution with a small amount of similarly coloured precipitate. Multinuclear NMR spectroscopy of the SO_2 solution revealed that the original compound had degraded. In the ^{31}P NMR spectrum, $[FP(CH_3)_3]^+$ (145.2 ppm, (d), $^1J_{P-F}$ = 950 Hz), $WOF_4\{OP(CH_3)_3\}$ (69.3 ppm, (s)) and free $OP(CH_3)_3$ (38.0 ppm, (s)) were identified.[8-9] The $[WOF_5]^-$ anion (F_{eq}: 56.1 ppm, (d), $^2J_{Fax-Feq}$ = 71 Hz, $^1J_{W-F}$ = 52 Hz; F_{ax}: –75.6 ppm (qn), $^2J_{Fax-Feq}$ = 52 Hz, $^1J_{W-F}$ = 52 Hz), meanwhile, was identified as the major product in the ^{19}F NMR spectrum and $[WF_7]^-$ (148.3 ppm, (s)) as the minor product. Trace amounts of $WSF_4(py)$ (83.6 ppm, (s)), $WOF_4(py)$ (66.1 ppm, (s), $^1J_{W-F}$ = 63 Hz), $[W_2O_2F_9]^-$ (F_{term}: 65.4 ppm, (d) $^2J_{F-F}$ = 58 Hz, $^1J_{W-F}$ = 73 Hz; $F_{br.}$: −143.7 ppm, (multiplet), $^2J_{F-F}$ = 58 Hz), $WOF_4\{OP(CH_3)_3\}$ (61.6 ppm, (s), $^1J_{W-F}$ = 69 Hz), as well as $[FP(CH_3)]^+$ (−135.8 ppm, (d), $^1J_{P-F}$ = 950 Hz) were observed.[9-10] An unassigned signal was observed at 167.7 ppm and can be attributed to either WF_6 or $WF_6(py)$ due to their identical chemical shift. The formation of $OP(CH_3)_3$, alongside the formation of a beige precipitate presumed to be S_8, is consistent with the reaction previously observed for $P(CH_3)_3$ with SO_2 conducted by Smith and Smith.[11] Herein, SO_2 is proposed to undergo nucleophilic attack by trimethylphosphine to form a P–S bond (Eq. 3.3). This intermediate results in a formally negatively charged oxygen which then undergoes nucleophilic attack towards the formally positively charged phosphorus

atom. This reacts to form the observed phosphine oxide and unobserved sulfur monoxide, which disproportionates into SO_2 and elemental sulfur at ambient temperature.[11] It is also hypothesized that the generated SO can lead to the formation of the various tungsten oxides and the reaction with elemental sulfur yielding the tungsten sulphide fluoride observed within the system.[10]

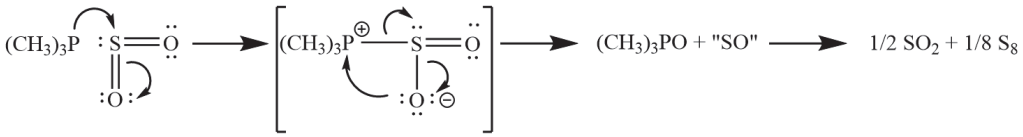

(Eq. 3.3)

3.2.2. X-Ray Crystal Structure of $WF_6(py)\{P(CH_3)_3\}\bullet CH_2Cl_2$

Crystals of $WF_6(py)\{P(CH_3)_3\}\bullet CH_2Cl_2$ were grown from the mother liquor at –40 °C, resulting in orange plate-like crystals. The solid-state structure of $WF_6(py)\{P(CH_3)_3\}\bullet CH_2Cl_2$ was determined via X-ray crystallography at –173 °C. The gas-phase geometry of $WF_6(py)\{P(CH_3)_3\}$ was optimised using the experimental geometry as a starting point.[12] Data collection and refinement parameters of the crystal are provided in the Table 3.1. The $WF_6(py)\{P(CH_3)_3\}$ adduct crystallises in the monoclinic $P2_1/n$ space group alongside one equivalent of CH_2Cl_2. No significant intermolecular contacts were observed, and all atoms are crystallographically unique. A list of the experimental and calculated bond lengths within $WF_6(py)\{P(CH_3)_3\}$ and related species are listed in Table 3.2.

Table 3.1 Crystallographic Data Collection and Refinement Parameters for $WF_6(py)\{P(CH_3)_3\}\bullet CH_2Cl_2$

	$WF_6(py)\{P(CH_3)_3\}\bullet CH_2Cl_2$
Identification Code	MG22004_a
Empirical Formula	$C_9H_{16}Cl_2F_6NPW$
Formula weight	537.95
Temperature (K)	99.98(12)
Crystal system	Monoclinic
Space group	$P2_1/n$
a (Å)	9.7032(3)
b (Å)	13.8549(4)
c (Å)	11.4499(4)
α (°)	90
β (°)	94.294(3)
γ (°)	90
Volume (Å^3)	1534.97(8)
Z	4
ρ_{calc} (g cm^{-3})	2.328
μ (mm^{-1})	8.028
F(000)	1016.0
Crystal size (mm^3)	0.249 × 0.102 × 0.071
GooF	1.067
Final R indexes [I>=2σ (I)]	R_1[a] = 0.0365, wR_2[b] = 0.0670
Final R indexes [all data]	R_1[a] = 0.0504, wR_2[b] = 0.0705
Largest diff. peak/hole (e Å^{-3})	4.97/–2.33

[a]$R_1 = \sum||F_o| - |F_c||/\sum|F_o|$. [b]$wR_2 = [\sum[w(F_o^2 - F_c^2)^2]/\sum w(F_o^4)]^{1/2}$.

The adduct adopts a bicapped trigonal prismatic geometry with the pyridine and trimethylphosphine ligands capping two square faces (Figure 3.1). The dative W–N bond of $WF_6(py)\{P(CH_3)_3\}$ (2.319(3) Å) was found to be insignificantly different from that of $WF_6(py)_2$ (2.334(6) Å).[12] Meanwhile the dative W–P (2.5944(9) Å) bond was found to be slightly longer compared to that of $WF_6\{P(CH_3)_3\}_2$ (2.5867(7) Å) and is believed to be due to the increased electron density on the metal centre donated by the pyridine ligand.[12] This in turn leads to a B–W–B (B = base) angle that lies virtually medial between the two bis-ligand species (123.99(8) vs. 126.3(3) and 119.46(2) for the bis-trimethylphosphine and bis-pyridine compounds, respectively). Interesting, however, is the comparison of the W–

F bonds between these species. Despite pyridine being a stronger Lewis base than trimethylphosphine, octa-coordinate WF_6 adducts with the latter ligand have, on average, longer W–F bonds than those of the former. This is in contrast to the expectation that the stronger pyridine ligand (BF_3 affinity: 128 kJ mol^{-1}, compared to $P(CH_3)_3$, BF_3 affinity: 97 kJ mol^{-1}) donates more electron density to the W centre, rendering the W–F bonds more ionic, *i.e.*, longer, in the adduct.[7] The contrary observation is consistent with the steric effects of the larger $P(CH_3)_3$ ligand, overruling the electronic effect.

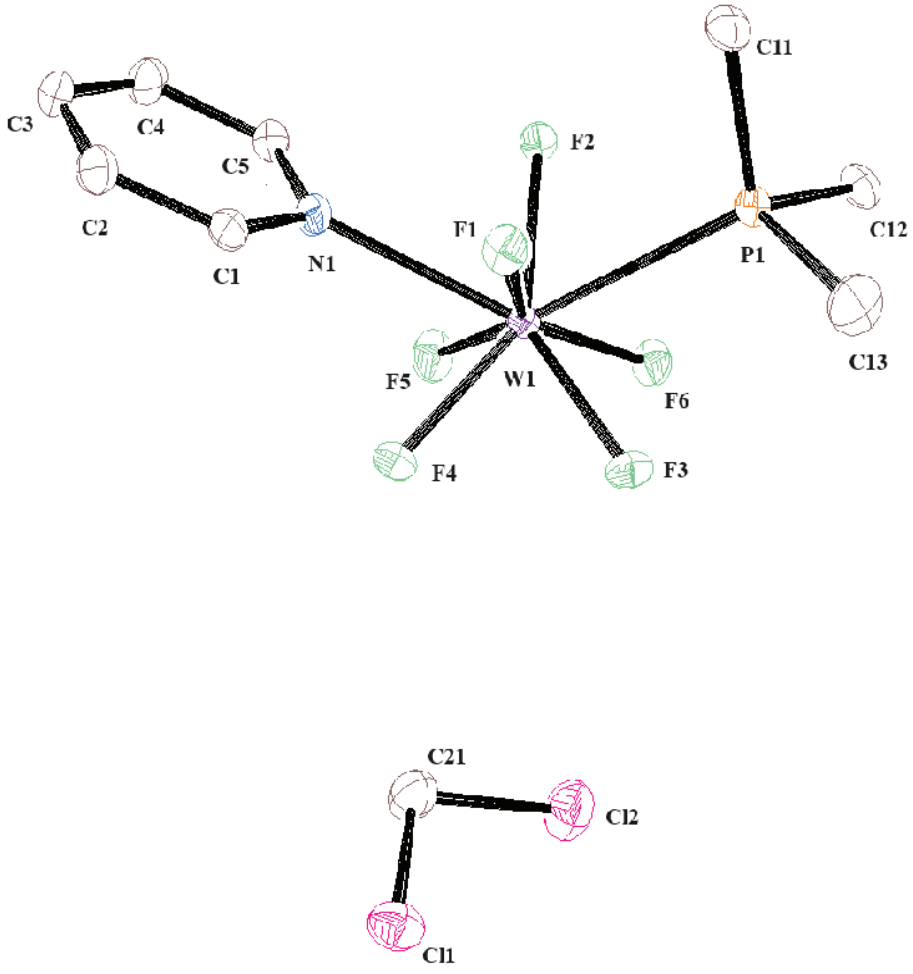

Figure 3.1. Thermal ellipsoid plots (50% probability level) of $WF_6(py)\{P(CH_3)_3\}\bullet CH_2Cl_2$.

Table 3.2. Experimental and Calculated[a] [given in square brackets] Bond Lengths (Å) and Angles (º) of Select Fluoridotungsten(VI) Complexes.

	$WF_6(py)_2$[b]	$WF_6(py)\{P(CH_3)_3\}$	$WF_6\{P(CH_3)_3\}_2$	$WF_6(py)$[c]	$WF_6\{P(CH_3)_3\}$[d]
W–F1	1.885(6)[1.885]	1.912(2)[1.914]	1.940(1)[1.935]	1.880(6)[1.868]	1.893(13)[1.889][e]
W–F2	1.883(6)[1.885]	1.901(2)[1.914]	1.945(1)[1.935]	1.875(5)[1.868]	1.820(15)[1.881][f]
W–F3	1.898(5)[1.884]	1.915(2)[1.904]	1.931(2)[1.910]	1.861(5)[1.877]	1.83(2)[1.867]
W–F4	1.900(5)[1.884]	1.920(2)[1.890]	1.928(1)[1.908]	1.864(5)[1.877]	1.893(13)[1.889][e]
W–F5	1.898(5)[1.884]	1.906(2)[1.890]	1.918(2)[1.910]	1.843(5)[1.877]	1.820(15)[1.881][f]
W–F6	1.900(5)[1.884]	1.927(2)[1.904]	1.919(2)[1.908]	1.868(5)[1.877]	1.89(2)[1.867]
$W–F_{(ave)}$	1.894	1.913	1.930	1.865	1.858
W–B1	2.334(6)[2.480]	2.319(3)[g]	2.5867(7)[2.702]	2.251(7)[2.343]	——
W–B2	2.334(6)[2.480]	2.5944(9)[h]	2.5867(7)[2.702]	——	2.598(9)[2.67]
B–W–B	126.3(3)[126.2]	123.99(8)[124.3]	119.46(2)[125.3]	——	——

[a] Calculated at the B3LYP/aVTZ level of theory. [b] From reference 6. [c] From reference 13. [d] From reference 4. [e] Related to one another via crystallographic symmetry. [f] Related to one another via crystallographic symmetry. [g] Refers to the W–N bond. [h] Refers to the W–P bond.

3.2.3. Multinuclear NMR Spectroscopy

The nature of products in the reaction that form $WF_6(py)\{P(CH_3)_3\}$ in solution was investigated utilizing ^1H, ^{19}F, ^{31}P and $^{31}P\{^1H\}$ NMR spectroscopy. These experiments were carried out utilizing CH_3CN and CH_2Cl_2 as solvents at ambient temperature and at –35 °C (CH_3CN) or –35 and –40 °C (CH_2Cl_2).

Whereas the ^1H NMR spectrum of the CH_3CN solution showed three resonances for adducted pyridine (at 22 °C, H_o: 8.9 ppm H_m: 7.6 ppm, H_p: 8.1 ppm), the signals for the phosphine ligand overlap with the CH_3CN solvent signal. The ^{19}F NMR spectrum of the

orange powder dissolved in CH_3CN at ambient temperatures (Figure 3.2) reveals a mixture of products in the fluorido tungsten region (250 - –150 ppm).

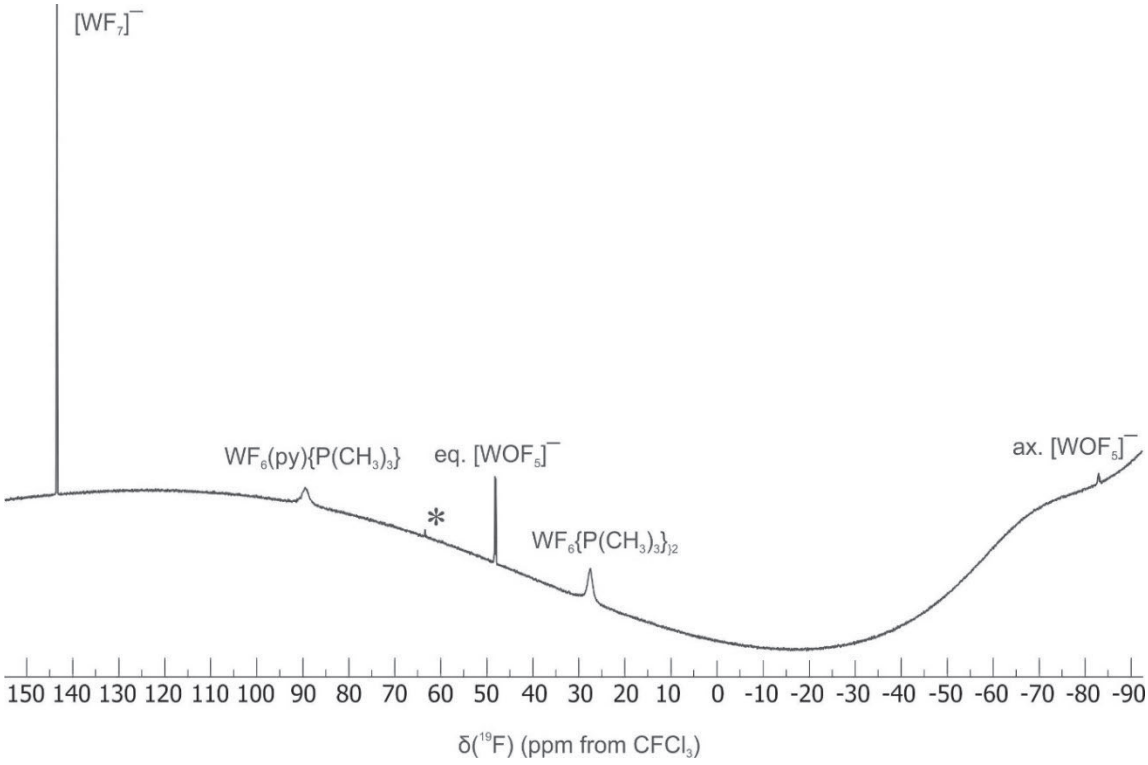

Figure 3.2. ^{19}F NMR spectrum of the isolated products from the reaction of $WF_6(py)$ + $P(CH_3)_3$, dissolved in CH_3CN at 22 °C. The asterisk (*) denotes a trace amount of $WOF_4(py)$.

While traces of the tungsten oxide fluoride species $WOF_4(py)$ (63.5 ppm, (s)), and $[WOF_5]^-$ (F_{eq}: 48.1 ppm, (d), $^2J_{Fax–Feq}$ = 52 Hz, $^1J_{W–Feq}$ = 71 Hz; F_{ax}: –82.9 ppm (qn), $^2J_{Fax–Feq}$ = 52 Hz) are present, the major constituents are $[WF_7]^-$ (143.4 ppm, (s)) with a relative integration of 0.58, a broad resonance at 89.5 ppm integrating to 0.66, as well as a broad resonance at 27.6 ppm with an integration of 1.00.[4,9,13] Previous work within the group has found a resonance at 28 ppm for $WF_6\{P(CH_3)_3\}_2$, thus allowing for attributing the singlet at 27.6 ppm to $WF_6\{P(CH_3)_3\}_2$ and for the tentative assignment of the $WF_6(py)\{P(CH_3)_3\}$ adduct to the resonance at 89.5 ppm.[13] At 22 °C, the different fluorine environments within each adduct, $WF_6(py)\{P(CH_3)_3\}$ and $WF_6\{P(CH_3)_3\}_2$, are rapidly

exchanging on the NMR time scale ($\Delta\nu_{1/2}$ = 492 and 355 Hz, respectively). This is consistent with neutral octa-coordinate adducts, such as $WF_6(py)_2$ which gives rise to a singlet at 114 ppm ($\Delta\nu_{1/2}$ = 300 Hz) at 0 °C.[2] An NMR sample of the orange solid dissolved in CH_2Cl_2 gave similar resonances at 22 °C: $[WF_7]^-$ as a sharp singlet at 143.0 ppm, $WF_6(py)\{P(CH_3)_3\}$ as a board singlet at 95 ppm, $WF_6\{P(CH_3)_3\}_2$ as a broad singlet at 27.7 ppm in a 0.36 : 0.95 : 1.00 relative integral ratio. Small amounts of products from accidental hydrolysis were also observed: $WOF_4(py)$ (63.4 ppm, (s)) and $[WOF_5]^-$ (F_{eq}: 51.9 ppm, (d), $^2J_{Fax-Feq}$ = 53 Hz, $^1J_{W-Feq}$ = 71 Hz; F_{ax}: –110.3 ppm (m), Hz). The ^1H NMR spectrum showed broad singlets for the adducted pyridine, as well as an unresolved overlapping signals for adducted $P(CH_3)_3$ species.

Cooling the CH_3CN solution to –35 °C revealed that the mixed ligand ^{19}F resonance from $WF_6(py)\{P(CH_3)_3\}$ significantly shifted from 89.5 ppm to 63.0 ppm. The temperature of –35 °C was insufficient in slowing down the intramolecular fluorine exchange for $WF_6(py)\{P(CH_3)_3\}$ and $WF_6\{P(CH_3)_3\}_2$, still appearing as broad singlets in the ^{19}F NMR spectrum. The resonances, however, are narrower at –35 °C with $\Delta\nu_{1/2}$ = 285 and 271 Hz for $WF_6(py)\{P(CH_3)_3\}$ and $WF_6\{P(CH_3)_3\}_2$, respectively (Figure 3.3). This narrowing is counterintuitive, since further broadening is expected upon cooling due to slowing of the internal chemical exchange, suggesting that a secondary exchange mechanism, possibly intermolecular, is operative at room temperature. This secondary fast exchange mechanism could explain the substantial change of chemical shift for the $WF_6(py)\{P(CH_3)_3\}$ resonance upon cooling and might also explain the difficulty observing $^{31}P\{^1H\}$ resonances at room temperature. A possible exchange, but not the only one, is that between $WF_6(py)\{P(CH_3)_3\}$ and $WF_6(py)$ and free phosphine, with the latter two not being observed as separate

resonances. It is also noteworthy that the relative intensities changed upon cooling to 0.28 : 0.87 : 1 for $[WF_7]^-$: $WF_6(py)\{P(CH_3)_3\}$: $WF_6\{P(CH_3)_3\}_2$, further supporting intermolecular chemical exchange processes. In addition, ^{19}F resonances associated with $[FP(CH_3)_3]^+$ (138.6 ppm, (d), $^1J_{P–F}$ = 945.4 Hz) and $F_2P(CH_3)_3$ (–7.6 ppm, (d), $^1J_{P–F}$ = 532.7 Hz) were resolved in the LT ^{19}F NMR spectrum, which did not appear in the room temperature spectrum, again suggesting chemical exchange at the higher temperature.[14–15] The $^{31}P\{^1H\}$ NMR spectrum at –35 °C (Fig. 3.4) reveals multiple phosphorus signals, including two septets, representing the major P-containing species in solution. The septet resonance at 96.1 ppm ($^2J_{P–F}$ = 88.2 pm) is assigned to $WF_6\{P(CH_3)_3\}_2$ and the one at 110.0 ppm ($^2J_{P–F}$ = 89.4 Hz) is assigned to the $WF_6(py)\{P(CH_3)_3\}$ adduct (Figure 3.4). Integration of these peaks in the ^1H-coupled ^{31}P NMR spectrum afforded an integration of 1 : 0.51 for $WF_6\{P(CH_3)_3\}_2$ to $WF_6(py)\{P(CH_3)_3\}$, representing a close to equimolar distribution, because of the presence of two phosphorus atoms in the 1 : 2 adduct. This molar ratio is close to that observed in the ^{19}F NMR spectrum, supporting the assignment of the ^{19}F resonances. A doublet at 146.1 ppm is attributed to $[FP(CH_3)_3]^+$, while $F_2P(CH_3)_3$ can be observed at –12.6 ppm (t), paralleling their observation in the ^{19}F NMR spectrum. Small amounts of $[(CH_3)_3PP(CH_3)_3]^{2+}$ and $[HP(CH_3)_3]^+$ were observed at 25.4 ppm (s) and at 0.1 ppm (s), respectively.[14,16–18]

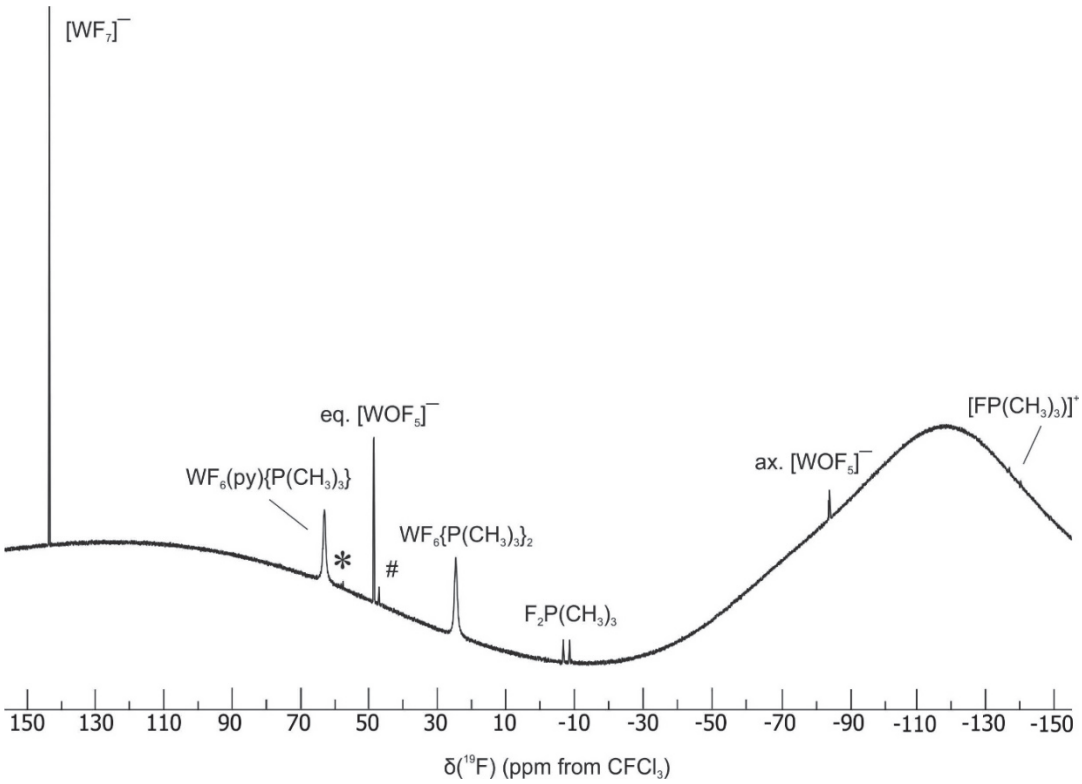

Figure 3.3. ^{19}F NMR spectrum of the isolated products from the reaction of $WF_6(py)$ + $P(CH_3)_3$, dissolved in CH_3CN at –35 °C. # and * denote trace amounts of $WOF_4\{P(CH_3)_3\}$ and $WOF_4(py)$, respectively.

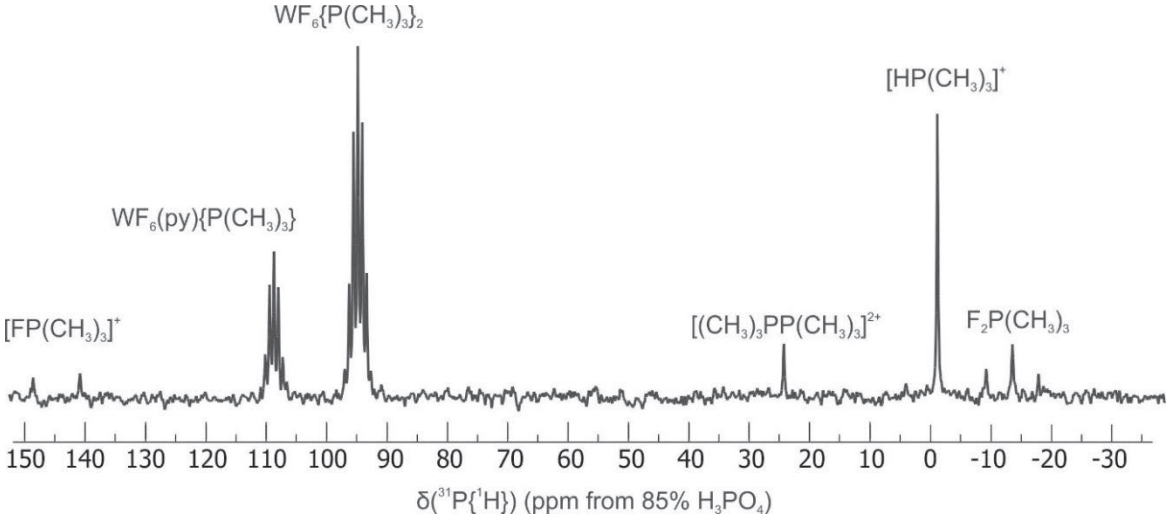

Figure 3.4. $^{31}P\{^1H\}$ NMR spectrum of the isolated products from the reaction of $WF_6(py)$ + $P(CH_3)_3$, dissolved in CH_3CN at –35 °C.

The NMR spectrum in CH_2Cl_2 at –35 °C shows the same species, but with different line widths and relative ratios: $[WF_7]^-$: sharp singlet at 142.2 ppm, $WF_6(py)\{P(CH_3)_3\}$: board singlet at 62.8 ppm, $\Delta\nu_{½}$ = 1100 Hz, $WF_6\{P(CH_3)_3\}_2$: broad singlet at 23.6 ppm, $\Delta\nu_{½}$ = 235 Hz, in addition to signals from the minor components $WOF_4(py)$, $[WOF_5]^-$ and $F_2P(CH_3)_3$. The relative ratio $[WF_7]^-$: $WF_6(py)\{P(CH_3)_3\}$: $WF_6\{P(CH_3)_3\}_2$ is 0.34 : 0.53 : 1. The $^{31}P\{^1H\}$ NMR spectrum confirms the predominance of $WF_6\{P(CH_3)_3\}_2$ at this temperature in CH_2Cl_2. The change in linewidth and relative ratio suggests the presence of solvent- and temperature-dependent equilibria that are not completely understood.

The results from the NMR spectra are surprising on two counts; first, no $WF_6(py)_2$ was observed, although the presence of $WF_6\{P(CH_3)_3\}_2$ suggests ligand scrambling. Secondly, the observation of large amounts of $[WF_7]^-$ is surprising, since it necessitates fluoride-ion transfer. Because of the absence of $[Hpy]^+$ in the ^1H NMR spectrum and the observation of only trace amounts of $[HP(CH_3)_3]^+$ in the ^{31}P NMR spectrum, the formation of $[WF_7]^-$ cannot solely arise from hydrolysis, which generates HF, leading to protonation of the base and F^- addition to WF_6. The $[WF_7]^-$ anion must therefore be formed as a by-product of one or more side reactions. The occurrence of further side reactions is evidenced by the formation of $F_2P(CH_3)_3$ and $[FP(CH_3)_3]^+$, indicating that the $P(CH_3)_3$ ligand is undergoing oxidation. While the mixed-ligand adduct and $WF_6\{P(CH_3)_3\}_2$ are observed in the ^{19}F NMR spectrum, no appreciable pyridine tungsten compound are present, aside from trace amounts of one of the hydrolysis products, $WOF_4(py)$. Thus, approximately two equivalents of pyridine are not accounted for.

In order to control the side reactions that occur at ambient temperatures and assess all reaction products, an NMR-scale reaction was carried out in CH_2Cl_2 solvent, briefly

warmed to –35 °C and then spectra were recorded at –40 °C. This experiment enabled the observation of all reaction products without prior isolation of non-volatile reaction products. Because of the small scale, a perfect control of stoichiometry was not easy to achieve, and a small excess of WF_6(py) was used. Fluorine-19 NMR spectroscopy of the reaction mixture showed several other signals than the previously observed species in the fluorido tungsten region in CH_3CN and CH_2Cl_2 solvents (Figure 3.3). Alongside the aforementioned species ($[WF_7]^-$: 142.5 ppm, WF_6(py){$P(CH_3)_3$}: 61.8 ppm, $\Delta\nu_{½}$ = 410 Hz; and trace amounts of WF_6{$P(CH_3)_3$}$_2$: 22.8 ppm, $\Delta\nu_{½}$ = 270 Hz), new peaks where assigned to WF_6{$P(CH_3)_3$} (130.2 ppm) and WF_6(py)$_2$ (125.1 ppm, $\Delta\nu_{½}$ = 2221 Hz).[2,4] Due to the similarities in chemical shift, the broad peak at 168.4 ppm ($\Delta\nu_{½}$ = 1546 Hz) can be assigned to either free WF_6, WF_6(py), or even $[WF_5(py)_3]^+$.[1,18–19] However, due to the presence of ligands, this signal is most likely WF_6(py) instead of WF_6. Peaks from $[FPMe_3]^+$ (144.1 ppm, (d), $^1J_{F–P}$ = 956.4Hz), and unresolved multiplets for WF_6(py){$P(CH_3)_3$} (108.1 ppm) and WF_6{$P(CH_3)_3$} (97.5 ppm) were observed in the $^{31}P\{^1H\}$ NMR spectrum, confirming the predominance of WF_6(py){$P(CH_3)_3$} in this sample. The ^1H NMR spectrum showed only one set of resonances for adducted pyridine and a doublet for adducted phosphine with possible signals as shoulders of the phosphine signal. The surprising observation of WF_6(py) in this NMR sample might be the result of a slight excess of WF_6(py) being used in this sample, shifting equilibria.

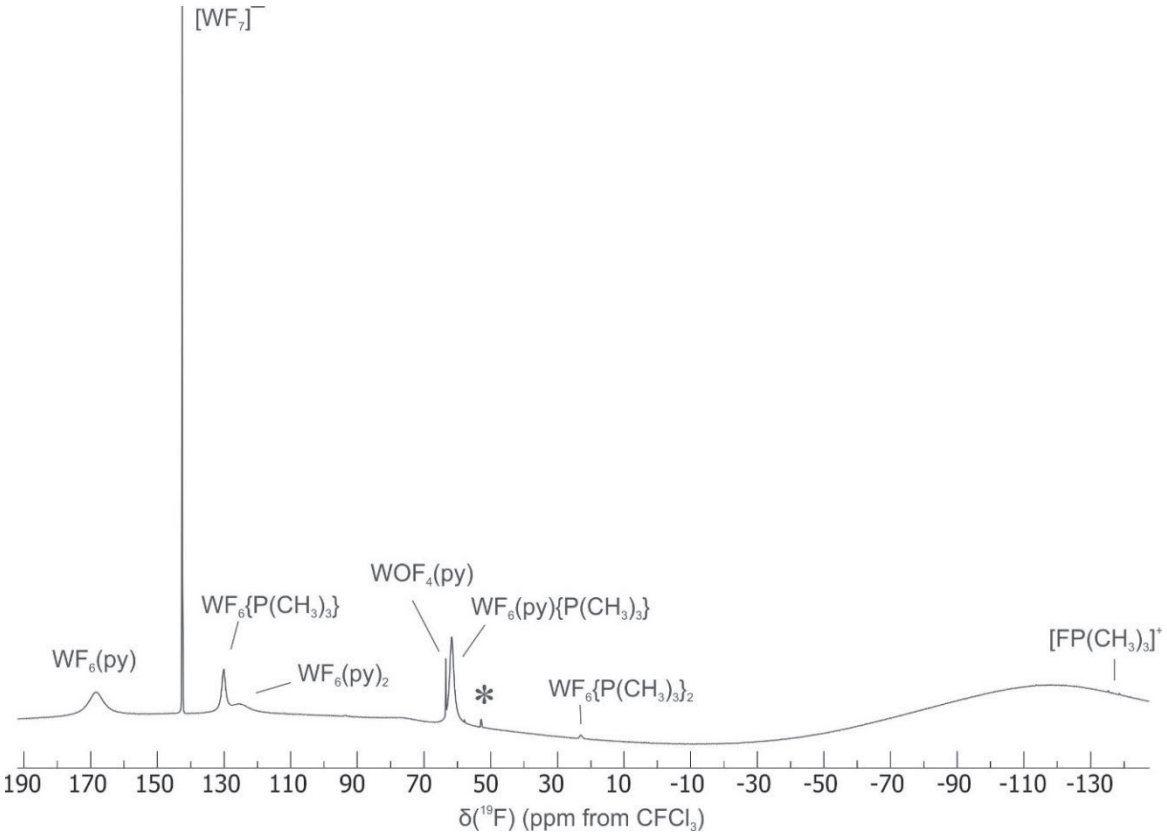

Figure 3.5. ^{19}F NMR spectrum of the reaction mixture of $WF_6(py)$ + $P(CH_3)_3$ in CH_2Cl_2 at –40 °C.

From the above NMR evidence, possible side reactions can be proposed based on species that are observed in solution (species observed by NMR spectroscopy are printed in bold font in the equations below). Dative W^{VI}–P bonds have been previously proposed to be weak with Seppelt *et al.* stating that the trimethylphosphine adduct possesses a detectable dissociation vapour pressure at ambient temperature.(4) Thus, it is likely that the mixed ligand complex exists in equilibrium, explaining the presence of $WF_6(py)$ (Eq. 3.4).

$$\mathbf{WF_6(py)\{P(CH_3)_3\}} \rightleftarrows \mathbf{WF_6(py)} + P(CH_3)_3 \qquad (3.4)$$

Based on the NMR evidence for ligand scrambling, a dissociative equilibrium of the pyridine ligand (3.5) could also be operative, although with a much smaller equilibrium constant than (3.4).

$$\mathbf{WF_6(py)\{P(CH_3)_3\}} \rightleftarrows \mathbf{WF_6\{P(CH_3)_3\}} + \text{py} \qquad (3.5)$$

These heptacoordinate adducts can react with another equivalent of base to generate the 1 : 2 adducts (Eqs. 3.6 and 3.7)

$$\mathbf{WF_6(py)} + \text{py} \rightleftarrows \mathbf{WF_6(py)_2} \qquad (3.6)$$

$$\mathbf{WF_6\{P(CH_3)_3\}} + P(CH_3)_3 \rightleftarrows \mathbf{WF_6\{P(CH_3)_3\}}_2 \qquad (3.7)$$

As seen for $WF_6(py)_2$, fluorido tungsten(VI) species can undergo fluoride abstraction in the presence of a base. Additionally, autoionization is known for WF_6 adducted to bidentate nitrogen and phosphorus bases. While adducts with bidentate nitrogen bases require a slight excess of WF_6 to be present to autoionize, this is not the case for bidentate phosphorus bases, which were shown to undergo autoionization even at a 1 : 1 ratio.[20-21] Thus, based on the presence of $[WF_7]^-$, it is believed that $WF_6(py)\{P(CH_3)_3\}$ undergoes ligand-induced autoionization forming a cationic octa-coordinate pentafluoro tungsten species (Eq. 3.5).

$$\mathbf{2WF_6(py)\{P(CH_3)_3\}} \rightarrow [WF_5(py)_2\{P(CH_3)\}]^+ + \mathbf{[WF_7]^-} + P(CH_3)_3 \qquad \text{(Eq. 3.8)}$$

Based on the observed autoionization of WF_6 with bidentate ligands, which resulted in the formation of octa-coordinate dications, it is proposed that the monocation $[WF_5(py)_2\{P(CH_3)\}]^+$ can undergo an additional instance of ligand-induced autoionization (Eq. 3.9), yielding the $[WF_4(py)_4]^{2+}$ dication, or similar dications with mixed ligands.

$$2[WF_5(py)_2\{P(CH_3)_3\}]^+ \rightarrow [WF_4(py)_4]^{2+} + \mathbf{WF_6\{P(CH_3)_3\}_2} \quad \text{(Eq.3.9)}$$

As observed previously within our group, cationic fluorido W^{VI} species are stronger oxidizers compared to their neutral counterparts.[20] Thus, the oxidization of $P(CH_3)_3$ and reduction of the tungsten centre to paramagnetic W^V species is possible. This is supported by the presence of both $[FP(CH_3)_3]^+$ and $F_2P(CH_3)_3$ observed in the system. In addition, insufficient cationic fluoride species with respect to the amount of $[WF_7]^-$ are observed by NMR spectroscopy, further support the generation of NMR-silent paramagnetic W^V species (Eq. 3.10).[15] Oxidation of pyridine cannot be excluded, although oxidation products have not been observed.

$$[W^{VI}F_4(py)_4]^{2+} + P(CH_3)_3 \rightarrow [W^{V}F_4(py)_4]^{+} + [P(CH_3)_3]^{\cdot+} \quad \text{(Eq. 3.10)}$$

While direct fluorination of the $P(CH_3)_3$ by these cationic species is indeed possible, the presence of $[(CH_3)_3PP(CH_3)_3]^{2+}$ as observed by ^{31}P NMR spectroscopy necessitates the formation of the $[P(CH_3)_3]^{\cdot+}$ radical cation (Eq. 3.11) and provides a means to generate W^V species.

$$2[P(CH_3)_3]^{\cdot+} \rightarrow \mathbf{[(CH_3)_3PP(CH_3)_3]^{2+}} \quad \text{(Eq. 3.11)}$$

Instead, $[WF_7]^-$ may react with $[(CH_3)_3PP(CH_3)_3]^{2+}$ and $[FP(CH_3)_3]^+$ to generate the observed fluorophosphorane species, as well as the intermediate formation of free WF_6, which reacts with free $P(CH_3)_3$ to form the observed $WF_6\{P(CH_3)_3\}$ (Eq. 3.12, 3.13).

$$\mathbf{3[WF_7]^-} + \mathbf{2[(CH_3)_3PP(CH_3)_3]^{2+}} \rightarrow \mathbf{3WF_6} + 2P(CH_3)_3 + \mathbf{F_2P(CH_3)_3} + \mathbf{[FP(CH_3)_3]^+} \quad \text{(Eq. 3.12)}$$

$$\mathbf{[WF_7]^-} + \mathbf{[FP(CH_3)_3]^+} \rightarrow \mathbf{WF_6} + \mathbf{F_2P(CH_3)_3} \quad \text{(Eq. 3.13)}$$

Alternatively, the generated $WF_6(py)_2$ may oxidize $[(CH_3)_3PP(CH_3)_3]^{2+}$ to form $[P(CH_3)_3]^{\cdot+}$ and $[P(CH_3)_3F]^+$, further generating W^V species and explaining its disappearance at 22 °C (Eq. 3.14).

$$\mathbf{WF_6(py)_2} + \mathbf{[(CH_3)_3PP(CH_3)_3]^{2+}} \rightarrow W^{(v)}F_5(py)\{P(CH_3)_3\} + [P(CH_3)_3]^{\cdot+} + \mathbf{[P(CH_3)_3F]^+} \quad \text{(Eq. 3.14)}$$

Tungsten oxide species observed in the spectra are proposed to arise from accidental hydrolysis. Tungsten hexafluoride and its adducts can react with water to form HF and WOF_4 (Eq. 3.15).

$$\mathbf{2WF_6(py)\{P(CH_3)_3\}} + 2H_2O \rightarrow \mathbf{WOF_4(py)} + \mathbf{WOF_4\{P(CH_3)_3\}} + 4HF + py + P(CH_3)_3 \quad \text{(Eq. 3.15)}$$

Any HF formed in Eq. 3.14 can then react with WF_6 and $P(CH_3)_3$ to form $[WF_7]^-$ and $[HP(CH_3)_3]^+$ (Eq. 3.16)

$$WF_6\{P(CH_3)_3\} + HF \rightarrow \mathbf{[WF_7]^-} + \mathbf{[HP(CH_3)_3]^+} \quad \text{(Eq. 3.16)}$$

Lastly, HF can then further react with WOF_4 and free $P(CH_3)_3$ to form $[WOF_5]^-$ and $[HP(CH_3)_3]^+$ (Eq. 3.17).

$$WOF_4 + HF \rightarrow \mathbf{[WOF_5]^-} + H^+ \quad \text{(Eq. 3.17)}$$

3.2.4 Raman Spectroscopy

Because of the side reactions observed in solution, the Raman spectrum of the powder is not expected to represent the pure mixed-ligand complex (Figure 3.6). Vibrational frequencies for $WF_6(py)\{P(CH_3)_3\}$ were calculated, allowing for the tentative assignment of Raman bands to $WF_6(py)\{P(CH_3)_3\}$. The Raman spectrum includes bands

of adducted pyridine, adducted $P(CH_3)_3$, as well as WF modes that match the predicted frequencies (Table 3.3.). However, the experimental Raman bands were somewhat broadened, possibly resulting from overlap of bands of related species, and a number of bands are present in the experimental spectrum that cannot be assigned to the mixed ligand complex. The band at 708 cm^{-1} can be attributed to $[WF_7]^-$ and bands at 602, 342, and 244 cm^{-1} coinciding with $WF_6\{P(CH_3)_3\}_2$ are present, further reflecting observations in the ^{19}F NMR spectra (*vide supra*). No cationic fluorido tungsten – pyridine species could be conclusively identified in the Raman spectrum, possibly due to signal overlap.

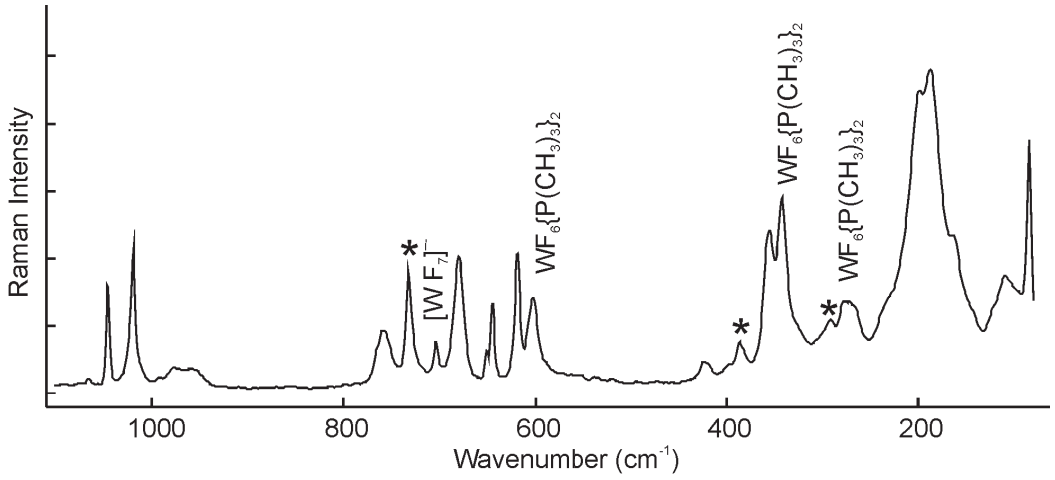

Figure 3.6. Raman spectrum of the orange solid recovered from the addition of $P(CH_3)_3$ to WF_6(py), recorded at ambient temperature in an FEP sample tube. Asterisks (*) denote FEP bands.

Table 3.3. Calculated Vibrational Frequencies (cm^{-1}) of $WF_6(py)\{P(CH_3)_3\}$ and Experimental Raman Frequencies for the orange solid recover from the addition of $P(CH_3)_3$ to $WF_6(py)$.

Expt.[a,b]	Calcd.[c]	Assignments
	3237(134)[8]	NC_5H_5, C–H stretching modes
	3234(>1)[>1]	
3102(6)	3209(210)[4]	
3096sh	3204(100)[6]	
3073(4)	3186(82)[4]	
	3149(37)[>1]	
3006sh	3147(79)[>1]	$P(CH_3)_3$, C–H stretching modes
	3146(16)[>1]	
2997(29)	3131(200)[7]	
	3128(47)[1]	
	3128(42)[>1]	
2922(97)	3049(490)[20]	
	3046(186)[6]	
	3045(29)[1]	
2802(2)		
1607(5)	1653(9)[20]	NC_5H_5, C–C and C–N stretching modes and in-plane ring deformation
1577(4)	1626(13)[3]	
1494(1)	1530(3)[5]	
	1489(>0.1)[30]	
	1482(>1)[9]	
	1465(>1)[7]	$P(CH_3)_3$, C–H wagging
1417(sh)	1463(2)[11]	
	1459(10)[2]	
1411(15)	1458(8)[>0.1]	
	1446(>0.1)[>0.1]	
1326(1)	1395(>0.1)[2]	NC_5H_5, C–C and C–N stretching modes and in-plane ring deformation
1303(7)	1343(1)[4]	$P(CH_3)_3$, C–H wagging
	1325(>0.1)[15]	
	1323(>1)[14]	
	1302(>1)[3]	NC_5H_5, in-plane ring deformation
1220(10)	1251(8)[30]	
1152(1)	1179(2)[3]	
	1109(>1)[>1]	
1065(2)	1099(2)[16]	
1042(24)	1065(54)[7]	
1018(33)	1043(35)[7]	NC_5H_5, $\nu_s(NC_5)$
	1030(>0.1)[>0.1]	NC_5H_5, out-of-plane ring deformations
	1014(>0.1)[>0.1]	

991(1)		
976(4)	983(9)[160]	$P(CH_3)_3$, $\rho(PC_3)$
	979(>1)[1]	NC_5H_5, out-of-plane ring deformations
	976(>0.1)[32]	$P(CH_3)_3$, $\rho(PC_3)$
	974(>0.1)[32]	$P(CH_3)_3$, $\rho(PC_3)$
958(4)		NC_5H_5, out-of-plane ring deformations
	886(>1)[0]	NC_5H_5, out-of-plane ring deformations
	861(>1)[9]	$P(CH_3)_3$, $\rho(PC_3)$
	860(>1)[10]	
	807(>0.1)[>0.1]	$P(CH_3)_3$, $\rho(PC_3)$
	783(>0.1)[20]	NC_5H_5, out-of-plane ring deformations
765(sh)	752(8)[18]	$P(CH_3)_3$, $\nu_{as}(PC_3)$
759(13)	749(6)[20]	$P(CH_3)_3$, $\nu_{as}(PC_3)$
	708(>0.1)[61]	NC_5H_5, out-of-plane ring deformations
703(13)		$[WF_7]^-$, $\nu_s(WF_7)$
	670(4)[1]	NC_5H_5, in-plane ring deformation
680(30)	669(20)[>1]	$P(CH_3)_3$, $\nu_s(PC_3)$
651(12)		
645(19)	655(18)[29]	NC_5H_5, in-plane ring deformation
618(31)	635(32)[77]	$\nu_s(WF_6)$
602(20)		$WF_6(P(CH_3)_3)_2$
	611(>1)[158]	$\nu_{as}(WF_6)$
	580(1)[193]	$\nu_{as}(WF_4)$
	564(5)[112]	$\nu_s(WF_2)$
	530(>1)[9]	$\nu_{as}(WF_2)$
	510(>1)[>1]	$\nu_{as}(WF_4)$
	476(>1)[3]	NC_5H_5, out-of-plane ring deformations
432(6)		
423(5)	419(1)[11]	$\delta_{scissoring}(WF_4)$
419(5)	401(>0.1)[>0.1]	NC_5H_5, out-of-plane ring deformation twisting
	382(>1)[8]	$\delta_{as}(WF_4)$
355(36)	351(10)[60]	$\omega(WF_2)$
342(47)		$WF_6(P(CH_3)_3)_2$
	335(2)[17]	$\delta_{umbrella}(WF_4)$
	325(>1)[1]	$\tau(WF_2)$
	323(6)[1]	$P(CH_3)_3$, $\delta_s(PC_3)$
	300(>1)[15]	$\delta(WF_4) + \delta_{as}(PC_3)$
277(20)		$WF_6(P(CH_3)_3)_2$
	268(>0.1)[2]	$\delta_{as}(PC_3)$
271sh	265(2)[8]	$\delta(WF_2) - \delta_{as}(PC_3)$
267sh	256(2)[1]	$\delta_{as}(PC_3)$
	251(1)[5]	$\delta_{as}(PC_3)$
	242(>0.1)[4]	$\rho(NC_5H_5)$
235(sh)	223(>1)[2]	NC_5H_5 and $P(CH_3)_3$ rocking

	205(1)[>0.1]	CH_3 twisting
	204(>1)[>1]	CH_3 twisting
199(68)	190(2)[1]	$\rho(P(CH_3)_3)$
187(72)	182(1)[>0.1]	CH_3 twisting
	165(>0.1)[1]	CH_3 twisting
	161(>0.1)[>1]	CH_3 twisting
164(35)	159(9)[2]	ν(W–P)
145sh	131(2)[6]	ν(W–N)
110(26)	114(2)[>0.1]	$\rho(NC_5H_5)$
	106(>0.1)[1]	$\rho(NC_5H_5)$
	74(1)[>0.1]	rocking and twisting modes
	52(4)[>1]	
	50(4)[3]	
	5(>0.1)[>1]	

[a] Recorded in ¼' FEP reactor at ambient temperature. [b] FEP bands were observed at 1379(8), 1292sh, 1220(10) {overlap}, 732(26), 386(10), 291(16) cm^{-1}.[c] Calculated at the B3LYP level of theory.

Leaving the powder over the course of a month at room temperature inside the dry box resulted in the formation of a brown-orange tacky solid. The Raman spectrum of the decomposition product is significantly different from that of the freshly isolated sample, with the original bands representing a minor component. Several bands are in excellent agreement with those reported for $WF_5(py)_2$ (1024, 655 cm^{-1}) (Figure 3.7). Additionally, bands at 589 and 562 cm^{-1} are also present that could possibly be attributed to the $\nu_s(WF_4)$ modes of cationic $[W^VF_4(L)_4]^+$ (L = py and/or $P(CH_3)_3$) species similarly observed by Gerken *et al.*[15] The appearance of these bands upon decomposition further supports the formation of NMR-silent W^V species like those proposed above.

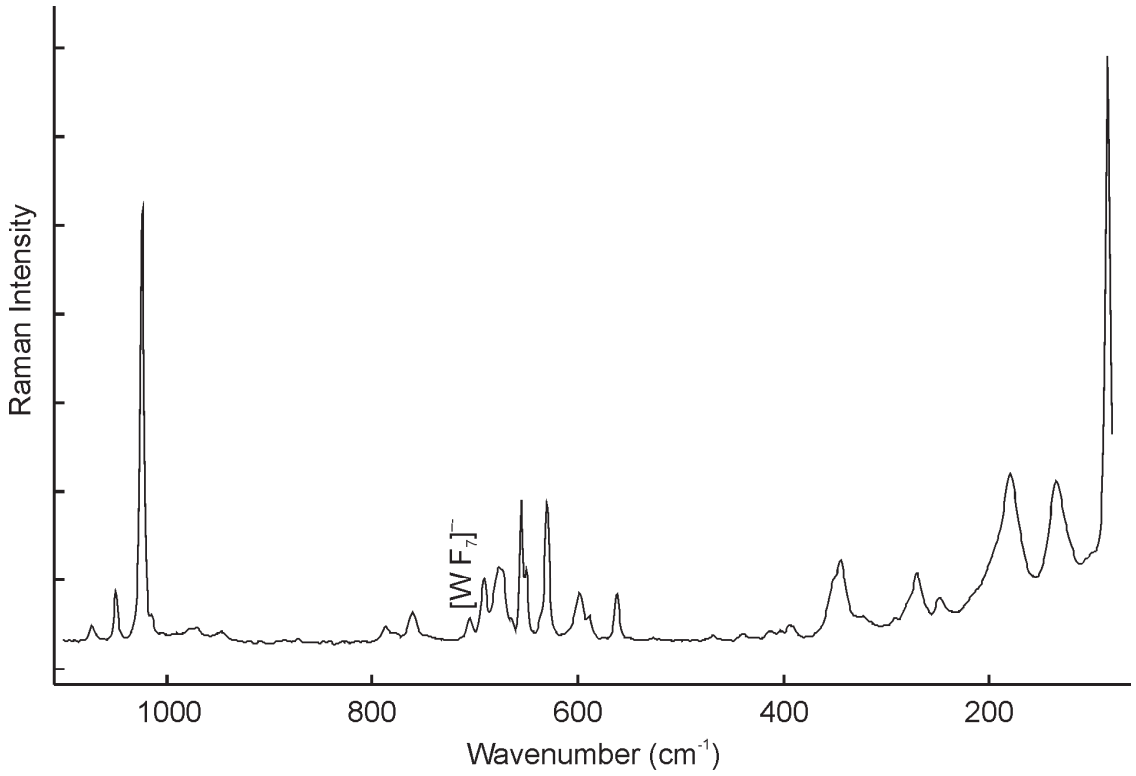

Figure 3.7. Raman spectrum of the brown-orange solid, recorded at ambient temperature in a glass m.p. capillary.

3.2.5 Computational Results

Calculations were carried out at the B3LYP/aVTZ level of theory.[22] NBO analyses were carried out and the important natural–population–analysis (NPA) charge are listed in Table 3.4 and the Wiberg bond indices (WBI) are summarized in Table 3.5.

Table 3.4. Natural–Population–Analysis Charges of Select Fluoridotungsten(VI) Complexes[a]

	WF_6	$WF_6\{P(CH_3)_3\}(py)$	WF_6py_2[b]	$WF_6\{P(CH_3)_3\}_2$	WF_6py[c]	$WF_6P(CH_3)_3$
W1	2.69	2.35	2.57	2.12	2.74	2.45
F1	–0.45	–0.54	–0.52	–0.55	−0.48	–0.51
F2	–0.45	–0.54	–0.52	–0.55	−0.48	–0.50
F3	–0.45	–0.51	–0.50	–0.52	−0.51	–0.48
F4	–0.45	–0.51	–0.50	–0.52	−0.51	–0.51
F5	–0.45	–0.51	–0.50	–0.52	−0.51	–0.50
F6	–0.45	–0.51	–0.50	–0.52	−0.51	–0.48
N1	—	–0.43	–0.43	—	−0.46	—
N2	—	—	–0.43	—	—	—
P1	—	1.13	—	1.10	—	1.09
P2	—	—	—	1.10	—	—
Σ(L)[d]	—	0.76	0.22	0.53	0.26	0.53

[a] Calculated at the B3LYP/aVTZ level of theory. Atom labels are as in Figure 3.1. [b] From reference 13. [c] From reference 6. [d] Sum of the NPA charge of all ligand atoms for one ligand.

Table 3.5. Wiberg Bond Indices of Various Select Fluoridotungsten(VI) Complexes[a]

	WF_6 [b]	$WF_6\{P(CH_3)_3\}(py)$	WF_6py_2[c]	$WF_6\{P(CH_3)_3\}_2$	WF_6py[d]	$WF_6\{P(CH_3)_3\}$
W–F(1)	0.80	0.65	0.69	0.62	0.76	0.70
W–F(2)	0.80	0.65	0.69	0.62	0.76	0.72
W–F(3)	0.80	0.69	0.72	0.66	0.72	0.74
W–F(4)	0.80	0.68	0.72	0.66	0.72	0.70
W–F(5)	0.80	0.68	0.72	0.66	0.72	0.72
W–F(6)	0.80	0.69	0.72	0.66	0.72	0.74
W–N	—	0.33	0.32	—	0.36	—
W–P	—	0.58	—	0.58	—	0.58
N–C	—	1.38	1.38	—	1.36	—
P–C	—	0.94–0.95	—	0.95	—	0.95
C_{aro}–C_{aro}	—	1.44	1.43–1.44	—	1.44	—
C_{aro}–H	—	0.91–0.93	0.91–0.92	—	0.92*	—
C_{Me}–H	—	0.92–0.93	—	0.92–0.93	—	0.92–0.93

[a]Calculated at the B3LYP/aVTZ level of theory. [b]From reference 23. [c]From reference 13. [d]From reference 6.

Upon coordination of the phosphorus ligand to the metal centre to form $WF_6(py)\{P(CH_3)_3\}$, the NPA charge of the metal centre (2.35) becomes substantially smaller than that in free WF_6 (2.69) because of donation of electron density from the ligands. When comparing pyridine and phosphine adducts, it was observed that the NPA charges on tungsten are consistently lower in the presence of phosphine ligands compared to pyridine ligands. This finding is consistent with the greater electronegativity of N versus P, resulting in less charge donation by pyridine, which is also reflected in the sum of the NPA charges of all ligand atoms (charge of $P(CH_3)_3$ in $WF_6\{P(CH_3)_3\}_2$: 0.53 per ligand; charge of pyridine in $WF_6(py)_2$: 0.22 per ligand). The larger charge donation by phosphine ligands is paralleled by stronger W–P bonds ($WF_6(py)\{P(CH_3)_3\}$: WBI = 0.54; $WF_6\{P(CH_3)_3\}_2$: WBI = 0.58) compared to the W–N bonds ($WF_6(py)\{P(CH_3)_3\}$: WBI =

0.22; $WF_6(py)_2$: WBI = 0.22). As a result of the charge donation to the tungsten centre, a substantial decrease in the WBIs of the W−F bonds in $WF_6(py)\{P(CH_3)_3\}$ (0.65 to 0.69), compared to free WF_6 (0.80) was observed, reflecting more ionic bonding in the adducts. Consistent with less charge donation by pyridine, the W–F bonds are stronger/less ionic in the pyridine adducts than in the phosphine adducts. Whereas the dative W–N bonds wherein the WBI are half of the W–F bonds in $WF_6(py)$ (0.36/0.72) and even less so in $WF_6(py)\{P(CH_3)_3\}$ (0.33/0.69) and $WF_6(py)_2$ (0.32/0.72), the W–P bonds are more strongly covalent with WBI values of W–P being more than ¾ that of W–F bonds in $WF_6\{P(CH_3)_3\}$ (0.58/0.74), $WF_6(py)\{P(CH_3)_3\}$ (0.54/0.69), and $WF_6\{P(CH_3)_3\}_2$ (0.58/0.66).

The finding that the dative W–P bonds are stronger than the W–N bonds is seemingly in conflict with the BF_3 affinities for $P(CH_3)_3$ (97 kJ mol^{-1}) and pyridine (128 kJ mol^{-1}), which predict pyridine to be the significantly stronger base.(7) The reconciliation of these conflicting findings could be based on the fact that the BF_3 affinities are enthalpy values towards dissociation of the respective adducts, while the NBO results provide measures of bond order. While the dative W–P bond is more covalent and less polar, it can still be more easily cleaved, presumably because of the larger size of phosphorus versus nitrogen.

3.3 Conclusions

Adducts of WF_6 with mixed ligands were explored utilizing both pyridine and trimethylphosphine ligands. The crystal structure of $WF_6(py)\{P(CH_3)_3\}$ conclusively showed the successful synthesis of the first reported mixed-ligand complex of WF_6. Additionally, the crystal structure showed that the bicapped trigonal prismatic geometry is

retained compared to that of the bispyridine and bis(trimethylphosphine) adducts. The crystal structure allowed for the comparison between select fluorido tungsten species revealing the differences in W–F bond lengths and B–W–B bond angles. DFT (B3LYP) studies help in understanding the differences in bonding character between the pyridine and phosphine ligands with the latter being capable of forming a more covalent dative bond to the metal centre and donating more electron density. This appears to be in contrast with base strength of the two ligands, pyridine being a stronger Lewis base than trimethylphosphine. The more covalent dative W–P bond does not necessarily represent a higher bond dissociation enthalpy. Multinuclear NMR experiments at ambient and low temperature indicate the presence of side reactions with the mixed ligand adduct being only one product. As a consequence of the side reactions, the mixed ligand adduct could not be isolated as a pure compound under the conditions used in this study, and the Raman spectrum shows the presence of other products. Nevertheless, most Raman bands can be correlated to the predicted (based on DFT calculations) vibrational bands of $WF_6(py)\{P(CH_3)_3\}$.

3.4 References

1. Tebbe, F. N.; Muetterties, E. L. Further Evidence of Stereochemical Nonrigidity in Five- and Seven-Coordinate Structures. *Inorg. Chem.* **1968**, *7* (1), 172–174. DOI: 10.1021/ic50059a040

2. Arnaudet, L.; Bougon, R.; Buu, B.; Lance, M.; Nierlich, M.; Thuéry, P.; Vigner, J. Characterization of the adducts WF_6•py and WF_6•2py (py = pyridine): crystal structure of WF_6•2py. *J. Fluorine Chem.* **1995**, *71* (1), 123–129. DOI: 10.1016/0022-1139(94)03160-2

3. Arnaudet, L.; Bougon, R.; Ban, B.; Lance, M.; Nierlich, M.; Vigner, J. Preparation, Characterization, and Crystal Structure of the Adducts WF_6•F-py and WOF_4•F-py (F-py = 2-Fluoropyridine). *Inorg. Chem.* **1993**, *32* (7), 1142–1146. DOI: 10.1021/ic00059a020

4. El–Kurdi, S.; Al–Terkawi, A.–A.; Schmidt, B. M.; Dimitrov, A. Seppelt, K. Tungsten(VI) and Tungsten(V) Fluoride Complexes. *Chem. Eur. J.* **2010**, *16* (2), 595 – 599. DOI: 10.1002/chem.200902307

5. Muetterties, E. L. and Wright, C. M. Molecular Polyhedra of High Co-ordination Number. *Quart. Rev. (London).* **1967**, *21* (1), 115. DOI: 10.1039/QR9672100109.

6. Turnbull, D.; Kostiuk, N.; Wetmore, S. D.; Gerken, M. Syntheses, Characterization, and Computational Studies of Tungsten Hexafluoride Adducts with Pyridine and Its Derivatives. *J. Fluorine Chem.* **2018**, *215*, 1–9. DOI: 10.1016/j.jfluchem.2018.08.007

7. Laurence, C. and Gal, J.–F. The BF_3 Affinity Scale. In *Lewis Basicity and Affinity Scales Data and Measurement*; John Wiley and Sons, Ltd., 2010; pp 85-109.

8. Merat, L.M.O.C.; San Gil, R.A.S.; Guerra, S.R.; Dieguez, L.C.; Caldarell, S.; Eon, J.G.; Ziarelli, F.; Pizzala, H. A Spectroscopic Probe for Combined Acid and Redox Properties in Acid Catalysts. *J. Mol. Catal. A: Chem.*, **2007**, *272* (1-2), 298–305. DOI: 10.1016/j.molcata.2007.02.025

9. Levason, W.; Reid, G.; Zhang, W. Coordination Complexes of the Tungsten(VI) Oxide Fluorides WOF_4 and WO_2F_2 with Neutral Oxygen- and Nitrogen-donor Ligands. *J. Fluorine Chem.* **2016**, *184*, 50–57. DOI: 10.1016/j.jfluchem.2016.02.003

10. Nieboer, J.; Yu, X.; Chaudhary, P.; Mercier, H. P. A.; Gerken, M. Synthesis, Characterization, and Computational Study of WSF_4•NC_5H_5. *Z. Anorg. Allg. Chem.* **2012**, *638* (3–4), 520–525. DOI: 10.1002/zaac.201100453

11. Smith, B.C; Smith, G.H. 1028. Sulfur dioxide. Part II. Reactions of tertiary phosphines with sulfur dioxide. *J. Chem. Soc.* **1965**, 5516-5517. DOI: 10.1039/JR9650005516

12. O'Donnell, F. Unpublished work.

13. Turnbull, D. *Lewis–Acid Behaviour of Neutral and Cationic Fluoridotungsten(V) and (VI) Complexes*, Ph.D. Thesis, University of Lethbridge, Lethbridge, AB, **2020**.

14. Doxsee, K.M.; Hanawalt, E.M.; Weakley, T.J.R. Synthesis of Difluorophosphoranes from Phosphines and Mercuric Fluoride. *Inorg. Chem.* **1992**, *31* (21), 4420–4421. DOI: 10.1021/ic00047a033

15. Turnbull, D.; Wetmore, S. D.; Gerken, M. Stabilisation of $[W^{V}F_4]^+$ by N- and P-Donor Ligands: Second-Order Jahn-Teller Effects in Octacoordinate d^1 Complexes. *Chem. - Eur. J.* **2021**, *27* (44), 11335-11343. DOI: 10.1002/chem.202100863

16. Siddique, R. M.; Winfield, J. The Oxidation of Dimethyl Sulphide, Trimethylamine, and Trimethylphosphine by Solvated Copper(II) or Thallium(III) Hexafluorometallates in Acetonitrile. *Can. J. Chem.* **1989**, *67* (11), 1780 DOI: 10.1138/v89-275

17. King, R. P.; Levason, W.; Reid, G. Neutral and cationic germanium(IV) fluoride complexes with phosphine coordination – synthesis, spectroscopy and structures. *Dalton Trans.* **2021**, *50* (47), 17751-17765. DOI: 10.1039/d1dt03339e

18. Rothwell, W. P.; Shen, W. X.; Lunsfrod, J. H.; ^{31}P Solid-State NMR of a Chemisorbed Phosphonium Ion in H-Y Zeolite: Observation of ^{1}H-^{31}P J Coupling in the Solid State *J. Am. Chem. Soc.* **1984**, *106* (8), 2452–2453 DOI: 10.1021/ja00320a048

19. Turnbull, D.; Hazendonk, P.; Wetmore, S. D.; Gerken, M. Stabilisation of $[WF_5]^+$ and WF_4 by Pyridine: Facile Access to $[WF_5(NC_5H_5)_3]^+$ and $WF_5(NC_5H_5)_2$. *Chem. - Eur. J.* **2020**, *26* (30), 6879-6886. DOI: 10.1002/chem.202000424

20. Arnaudet, L.; Bougon, R.; Ban, B.; Lance, M.; Navaza, A.; Nierlich, M.; Vigner, J. 2,2'-Bipyridine Fluoro Complexes of Tungsten(VI): Preparation, Characterization and Crystal Structure of $[WF_4(bipy)_2]^{2+} \bullet 2[WF_7]^- \bullet WF_6$ and $[WF_4(bipy)_2]^{2+} \bullet 2[WF_7]^- \bullet CH_3CN$; Preparation and Characterization of WF_6 bipy. *J. Fluorine Chem.* **1994**, *67* (1), 17-25. DOI: 10.1016/0022-1139(93)02926-6

21. Levason, W.; Monzittu, F. M.; Reid, G.; Zhang, W. Neutral and Cationic Tungsten(VI) Fluoride Complexes with Tertiary Phosphine and Arsine Coordination, *Chem. Commun.* **2018**, *54* (83), 11681–11684. DOI: 10.1039/C8CC05598J

22. Calculations performed by Felix O'Donnell.

23. Turnbull, D.; Wetmore, S. D.; Gerken, M. Stabilization of $[WF_5]^+$ by Bidentate N-Donor Ligands. *Angew. Chem., Int. Ed. Engl.* **2019**, *58* (37), 13035–13038. DOI: 10.1002/anie.201906600

Chapter 4 – Exploration of Phosphine Oxides as Ligands towards WF_6

4.1. Introduction

Tungsten hexafluoride has been reacted with numerous oxygen-containing compounds over the years, resulting in many fluoride tungsten compounds with W–O or W=O bonds. For example, numerous alkoxy-derivatives have been synthesized with the isolation of $WF_n(OCH_3)_{6-n}$ (n = 0-5), $WF_5(OC_2H_5)$, and $WF_5(OC_6H_5)$ representing just a few examples.[1-7] Meanwhile, pure WOF_4 has been obtained by reacting WF_6 with either B_2O_3 or SiO_2/HF.[8-10] This tungsten oxide fluoride has been observed to act as a fluoride-ion acceptor, capable of forming $[WOF_5]^-$ salts, as well as reacting with the anion to form $[W_2O_2F_9]^-$ (Eq. 4.1).(11-17) To date, no reactions of WF_6 with o-donor ligands has resulted in datively-bonded complexes.

$$WOF_4 + [WOF_5]^- \rightarrow [W_2O_2F_9]^- \quad (4.1)$$

Similar to tungsten hexafluoride, WOF_4 has also been found to form neutral adducts with a variety of ligands, the first of which was synthesized by Bougon *et al.* in 1983 wherein pure WOF_4 was reacted with pyridine (py) to form $WOF_4(py)_n$ (n = 1-2). The mono-adducted complex was observed to adopt a distorted octahedral geometry *trans* to the oxygen atom. The bis-adduct, meanwhile, was observed to adopt a pentagonal bipyramidal geometry with an axial oxo ligand.[18] The group further expanded upon these ligands with the synthesis of WOF_4(F-py) in 1993, observed to adopt a similar geometry and arrangement to WOF_4(py).[19]

Recently, Levason *et al.* developed an alternative pathway to $WOF_4(L)_{1-2}$ species by reacting WF_6 with $O(SiMe_3)_2$ in CH_3CN to form $WOF_4(NCCH_3)$. Due to the weak

basicity of CH_3CN, the group found they could displace this ligand with a variety of monodentate and bidentate ligands. Additionally, Levason *et al.* further reacted $WOF_4(NCCH_3)$ with an additional equivalent of $O(SiMe_3)_2$ and ligand to produce various $WO_2F_2(L)_2$ species. Perhaps most interesting of these species were adducts formed with dative oxygen bonds.[20] With the isolation of $WOF_4(L)$ (L = $O{=}P(C_6H_5)_3$, $O{=}P(CH_3)_3$, C_4H_8O, $O{=}S(CH_3)_2$), precedent was established to investigate if similar adducts with WF_6 could be synthesized. Indeed, phosphine oxides are known to possess BF_3 affinities that rival or surpass that of $P(CH_3)_3$ (97.43 ± 0.30 kJ/mol) which has been observed to form an adduct with WF_6. For instance, triethylphosphine oxide is reported to have a BF_3 affinity of 119.28 ± 0.74 kJ/mol, with the affinity of triphenylphosphine oxide reported as 103.3 ± 1.50 kJ/mol according to Laurence and Gal.[21] Further oxidation of these $O{=}PR_3$ ligands is also impossible due to the phosphorus existing in the +5 oxidation state. However, fluorine/oxygen exchange could still proceed as observed with the reaction of $O(SiMe_3)_2$.[20] In this chapter, the reactivity of WF_6 towards $O{=}PR_3$ (R = C_6H_5, C_2H_5) is detailed.

4.2. Results and Discussion

4.2.1. Synthesis

The reaction of WF_6 with $OP(C_2H_5)_3$ at an approximately equimolar ratio was carried out in CH_2Cl_2, resulting in a clear colorless solution. Upon removal of volatiles, a clear colorless oil was recovered in near stoichiometric yield, if adduct formation is assumed (Eq. 4.2). Subsequent cooling to –37 °C resulted in the oil solidifying into a white powder. Similarly, the reaction of WF_6 with $OP(C_6H_5)_3$ at an approximately equimolar ratio was also carried out in CH_3CN, resulting in a white precipitate crashing out of solution.

This precipitate, which was soluble in CH_2Cl_2, was recovered with a calculated yield of 111% assuming adduct formation (Eq. 4.2).

$$WF_6 + OPR_3 \rightarrow WF_6\{OPR_3\} \qquad (R = C_2H_5, C_6H_5) \text{ (Eq. 4.2)}$$

The products, however, were revealed to be mixtures of tungsten oxide fluorides and fluorinated phosphorus species, and were characterized via multinuclear NMR spectroscopy (Chapter 4.2.2.). Clear cubic crystals were grown and subsequently identified as $F_2P(C_6H_5)_3$ (Chapter 4.2.3.). From this, a reaction mechanism to obtain these products can be hypothesized. As is well known, phosphine oxides possess a resonance structure with the oxygen being negatively charged and the phosphorus becoming positively charged (Eq. 4.3). It is proposed that OPR_3 reacts with WF_6 to form $[WOF_5]^-$ and $[FPR_3]^+$ (R = C_2H_5, C_6H_5) via the mechanism below.

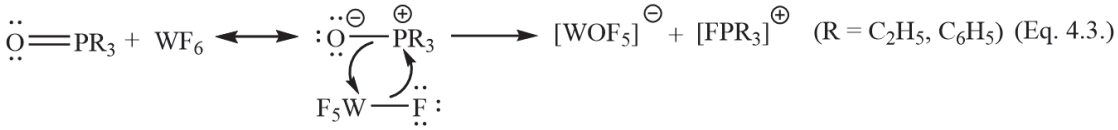

From here, it is reasonable to believe that subsequent fluoride-ion transfer can occur resulting in WOF_4 and F_2PR_3 (R = C_2H_5, C_6H_5) (Eq. 4.4).

$$[WOF_5]^- + [FPR_3]^+ \leftrightharpoons WOF_4 + F_2PR_3 \qquad (R = C_2H_5, C_6H_5) \text{ (Eq. 4.4)}$$

The resulting WOF_4 could then form a coordination product with any remaining free ligand to produce the proposed adducts. (Eq. 4.5)

$$WOF_4 + OPR_3 \rightarrow WOF_4(OPR_3) \qquad (R = C_2H_5, C_6H_5) \text{ (Eq. 4.5)}$$

4.2.2. Multinuclear NMR spectroscopy

In order to glean insight into the resulting products, the white precipitate recovered from the reaction of WF_6 with $OP(C_6H_5)_3$ was redissolved in CH_2Cl_2. The ^1H NMR spectrum at ambient temperature revealed overlapping signals situated in the range for aromatic protons (7.54-7.20 ppm) (Figure 4.1). The ^{19}F NMR spectrum is more informative, revealing numerous products arising from the aformentioned reaction (Figure 4.2). The major resonance of the spectrum lies at 60.1 ppm ((s), $^1J_{W–F}$ = 70 Hz), assigned to $WOF_4(OP(C_6H_5)_3)$, which is in good agreement with the values reported by Levason *et al.* (60.5 ppm, $^1J_{W–F}$ = 69 Hz).[20] Indeed, this assignment is confirmed with the $^{31}P\{^1H\}$ NMR spectrum displaying a singlet at 44.9 ppm (Figure 4.3), which is shifted to higher frequency compared to that of free $OP(C_6H_5)_3$ (27.7 ppm). Signals for $[WF_7]^–$ (142.4 ppm (s)), $[W_2O_2F_9]^–$ (F_{term}: 61.5 ppm (d), $^2J_{F–F}$ = 59 Hz, $^1J_{W–F}$ = 71 Hz; resonance for $F_{br.}$ is not observed because of its expected low intensity), $[FPPh_3]^+$ (–128.8 ppm (d), $^1J_{F–P}$ = 1002 Hz) and trace amounts of F_2PPh_3 (–40.0 ppm (d), $^1J_{F–P}$ = 673 Hz) were also found in the ^{19}F NMR spectrum. The $[FPPh_3]^+$ cation was also observed at 95.4 ppm ((d), $^1J_{P–F}$ = 1006 Hz) in the $^{31}P\{^1H\}$ NMR spectrum, while the expected signal for F_2PPh_3 was not observed, likely because of the low concentration.[20] Based on integration of the ^{19}F resonances, the molar ratio of $WOF_4(OP(C_6H_5)_3)$ to the sum of the fluorido oxido tungstenate anions was 1 : 0.5. The integration of the cation resonance and the two anion resonances indicate a mixture of dissolved $[FPPh_3]^+[WF_7]^–$ and $[FPPh_3]^+[W_2O_2F_9]^–$ salts in an approximate 1 : 0.09 ratio.

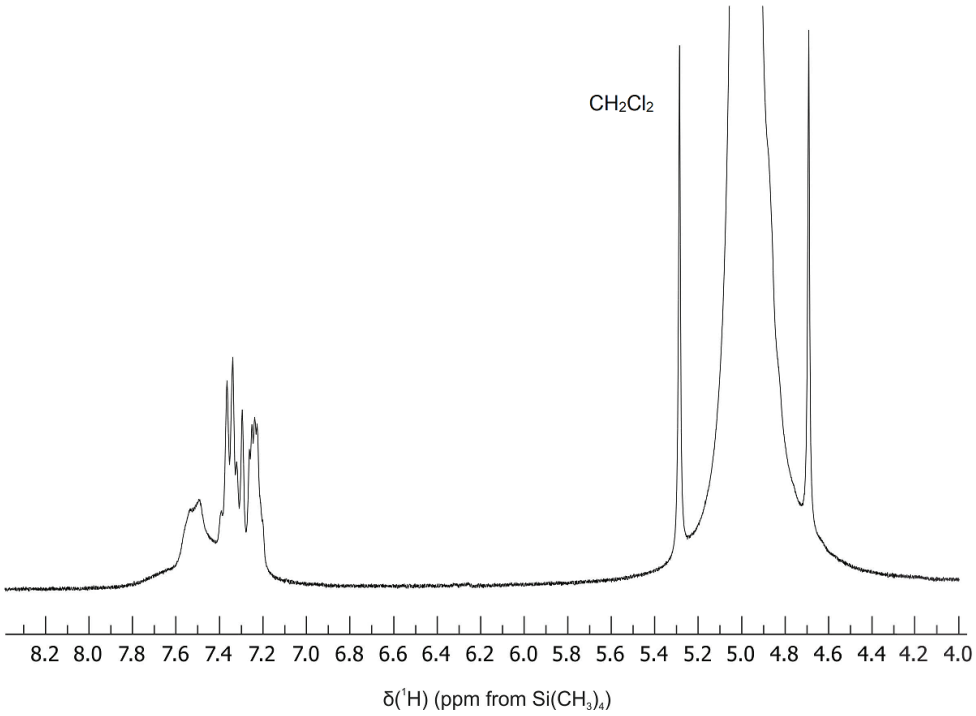

Figure 4.1. ^{1}H NMR spectrum of the isolated products from the reaction of WF_6 + $OP(C_6H_5)_3$, dissolved in CH_2Cl_2 at 22 °C.

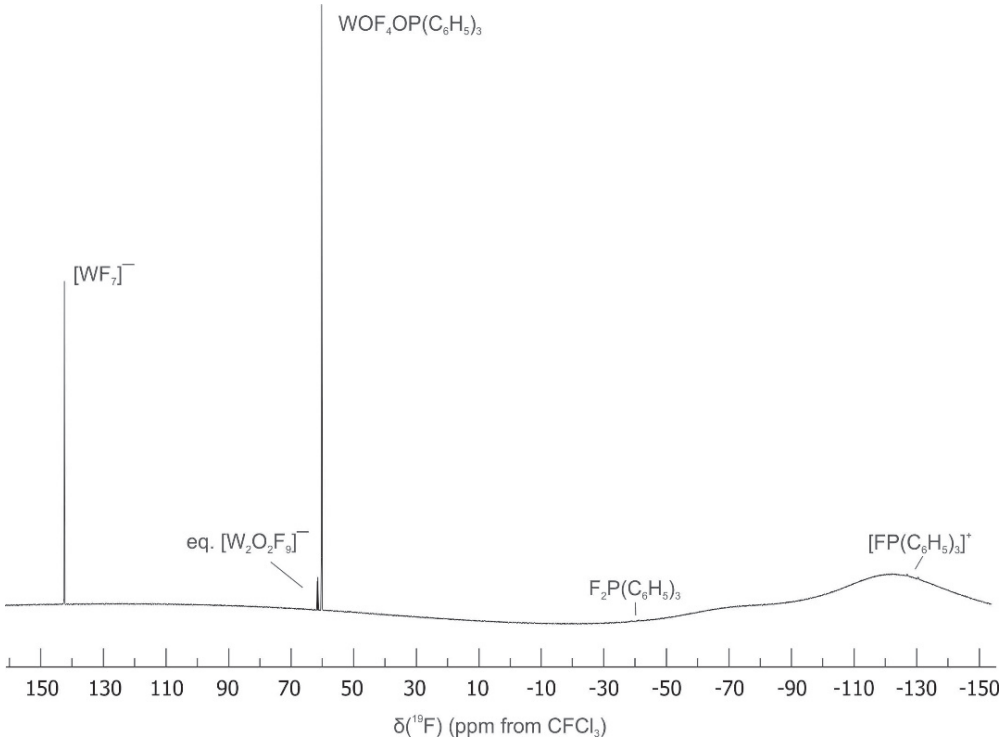

Figure 4.2. ^{19}F NMR spectrum of the isolated products from the reaction of WF_6 + $OP(C_6H_5)_3$, dissolved in CH_2Cl_2 at 22 °C.

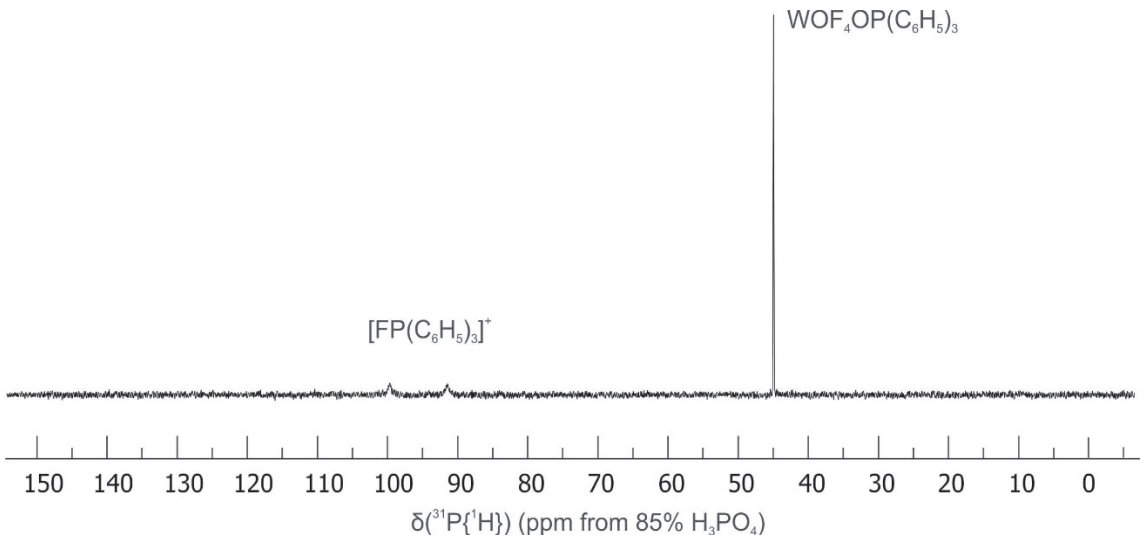

Figure 4.3. $^{31}P\{^{1}H\}$ NMR spectrum of the isolated products from the reaction of WF_6 + $OP(C_6H_5)_3$, dissolved in CH_2Cl_2 at 22 °C.

Levason *et al.* reported that increasing amounts of $[W_2O_2F_9]^-$ appear as a result of the decomposition of $WOF_4\{OP(C_6H_5)_3\}$, although the exact mechanism or rationale was not provided.[20] To verify their claim, the NMR sample was left at ambient temperature for 2 days and the ^{19}F NMR spectrum recorded once more (Figure 4.4). Consistent with the previous report, the amount of $[W_2O_2F_9]^-$ increased with the bridging fluorine now observed at –145.6. ppm ((sept.) $^2J_{F–F}$ = 58 Hz), alongside the appearance of $[WOF_5]^-$ at 52.1 ppm (F_{eq}: (d), $^2J_{F–F}$ = 53 Hz; resonance for $F_{ax.}$ is not observed because of its expected low intensity), paralleled by a reduction in $[WF_7]^-$ concentration and an increase in the deoxofluorination products, $[FPPh_3]^+$ and F_2PPh_3. This observation can be explained by deoxofluorination of the phosphine oxide by $[WF_7]^-$, which likely exists in a dissociative equilibrium with a low concentration of WF_6 at room temperature.

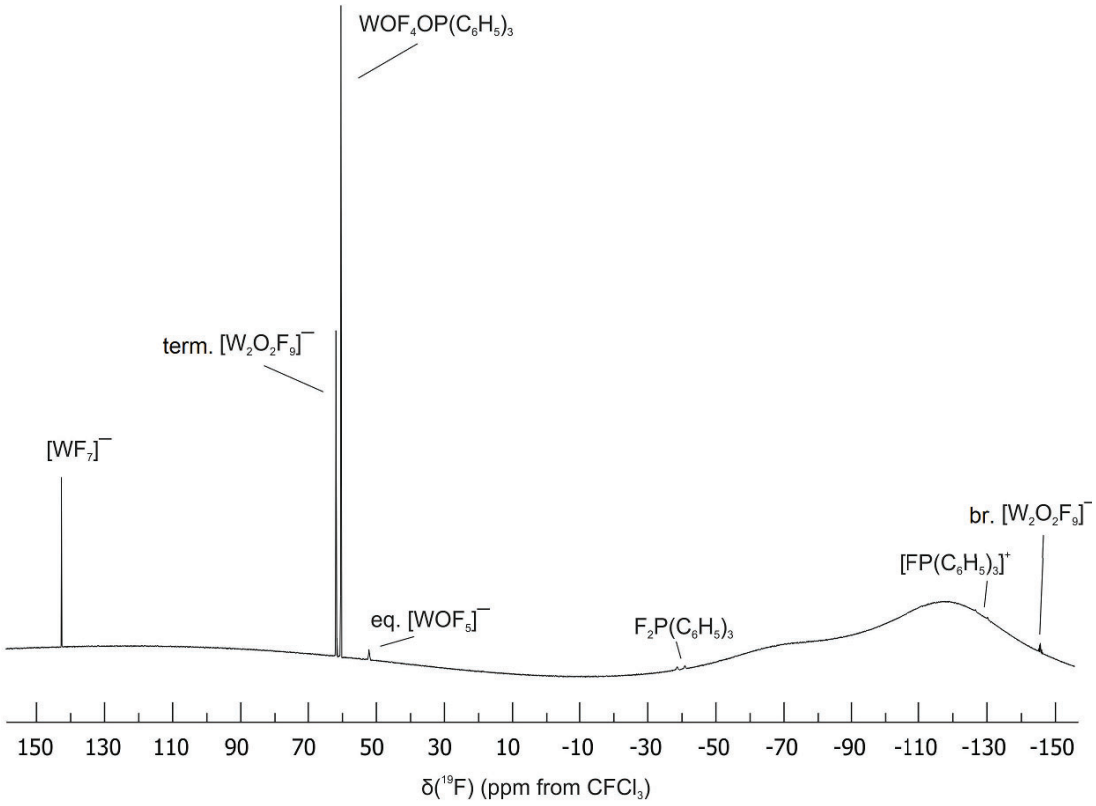

Figure 4.4. ^{19}F NMR spectrum of the isolated products from the reaction of WF_6 + $OP(C_6H_5)_3$, dissolved in CH_2Cl_2 at 22 °C after leaving the solution for 2 days at ambient temperature.

Multinuclear NMR spectra (^1H, ^{19}F and $^{31}P\{^1H\}$) of WF_6 with $OP(C_2H_5)_3$ in CH_2Cl_2 were recorded at 22 °C (Figures 4.5-7). The ^1H NMR spectrum reveals a doublet of quartets at 1.82 ppm ($^2J_{H–P}$ = 12.1, $^3J_{H–H}$ = 7.7 Hz), another doublet of quartets at 1.35 ppm ($^2J_{H–P}$ = 11.9, $^3J_{H–H}$ = 7.7 Hz) for methylene groups, and finally, two overlapping doublets of triplets forming the resonances at 0.73 ($^2J_{H–P}$ = 20.8, $^3J_{H–H}$ = 7.7 Hz) and 0.60 ppm ($^2J_{H–P}$ = 17.9, $^3J_{H–H}$ = 7.7 Hz) due to the methyl groups. A low-intensity unassigned resonance was also observed at 9.08 ppm. The two sets of methylene and methyl groups are shifted with respect to those observed for the free ligand in CH_2Cl_2 (CH_2: 0.91 ppm, $^2J_{H–P}$ = 11.7, $^3J_{H–H}$ = 7.7 Hz; CH_3: 0.38 ppm, $^2J_{H–P}$ = 16.0, $^3J_{H–H}$ = 7.8 Hz). The doublet of quartets at 1.35 ppm is

tentatively assigned as the CH_2 protons of $WOF_4\{OP(C_2H_5)_3\}$ allowing for the signal at 0.60 ppm to be assigned to the CH_3 portion of $WOF_4\{OP(C_2H_5)_3\}$.[20] Assignment of the second P–CH_2CH_3 containing species is inconclusive at this time, especially since only one resonance was observed in the $^{31}P\{^1H\}$ NMR spectrum for $WOF_4\{OP(C_2H_5)_3\}$ (Figure 4.7). Setting the integration of the CH_2 peak at 1.35 ppm to 2.00 H, the signal at 1.82 ppm integrates to 1.50 H, and the overlapping multiplets around 0.66 ppm integrate to 5.37 H. It was hypothesized at one point that there could be some imposed asymmetry onto the ligand due to complexation. However, if this was the case, the integration of the signals at 1.82 and 1.35 ppm should have integrated to 1 : 2 assuming one of the ethyl branches is different.

The ^{19}F NMR spectrum showed the major fluorine-containing products as a signal at 58.0 ppm ((s) $^1J_{W–F}$ = 71 Hz), assigned to the $WOF_4\{OP(C_2H_5)_3\}$ adduct, and is in agreement with the $WOF_4\{OP(CH_3)_3\}$ adduct formed by Levason *et al.* appearing as a singlet at 58.3 ppm ($^1J_{W–F}$ = 66 Hz).[20] This observation is paralleled by a $^{31}P\{^1H\}$ resonance at 77 ppm ((s) $^1J_{P–C}$ = 66 Hz) for the $WOF_4\{OP(C_2H_5)_3\}$ adduct. The ^{31}P NMR chemical shift is shifted to higher frequency from 51.0 ppm ((s) $^1J_{P–C}$ = 66 Hz) for the free ligand and is very close to that previously observed for $WOF_4\{OP(CH_3)_3\}$ ((s) 66.9 ppm).[20] Small amounts of $[WF_7]^-$ ((s) 143 ppm), and $[WOF_5]^-$ ($F_{eq.}$: 50 ppm (d) $^2J_{F–F}$ = 53 Hz, $^1J_{W–F}$ 71 Hz; $F_{ax.}$: –97 ppm (qn) $^2J_{F–F}$ = 53 Hz) and traces of free WF_6 ((s, broad) 163 ppm) were also observed in the ^{19}F NMR spectrum.[22] Despite there being anionic tungsten fluoride species present within the ^{19}F NMR spectrum, no cationic fluorido tungsten signals are observed. Thus, it is believed that $[FP(C_2H_5)_3]^+$ must be present to balance the anionic charges. This would, in turn, give rise to the second set of P–CH_2CH_3 signals observed in

the ^{1}H NMR spectrum. The relative integration of these signals are in the same range as the relative integration of the anions resonances versus that of the $WOF_4\{OP(C_2H_5)_3\}$ adduct in the ^{19}F NMR spectrum. The absence of resonances for $[FP(C_2H_5)_3]^+$ in the ^{19}F and ^{31}P NMR spectra at room temperature could be a consequence of chemical exchange. The absence of $F_2P(C_2H_5)_3$ in the NMR spectra, which is one of the expected deoxofluorination products, is assumed to be a consequence of its volatility and it being removed under dynamic vacuum during the isolation of the reaction products. Alternatively, residual difluorophosphorane could be exchanging with $[FP(C_2H_5)_3]^+$ as detailed in Equation 4.4. The predominance of $WOF_4\{OP(C_2H_5)_3\}$ versus anionic oxide fluorides, compared to larger amounts of tungsten oxide fluorides in the reaction with $OP(C_6H_5)_3$ (Figure 4.2,4) is a consequence of the stronger Lewis basicity of $OP(C_2H_5)_3$ compared to that of the triphenyl analogue, reducing the effective fluoride-ion acceptor strength of $WOF_4\{OP(C_2H_5)_3\}$.

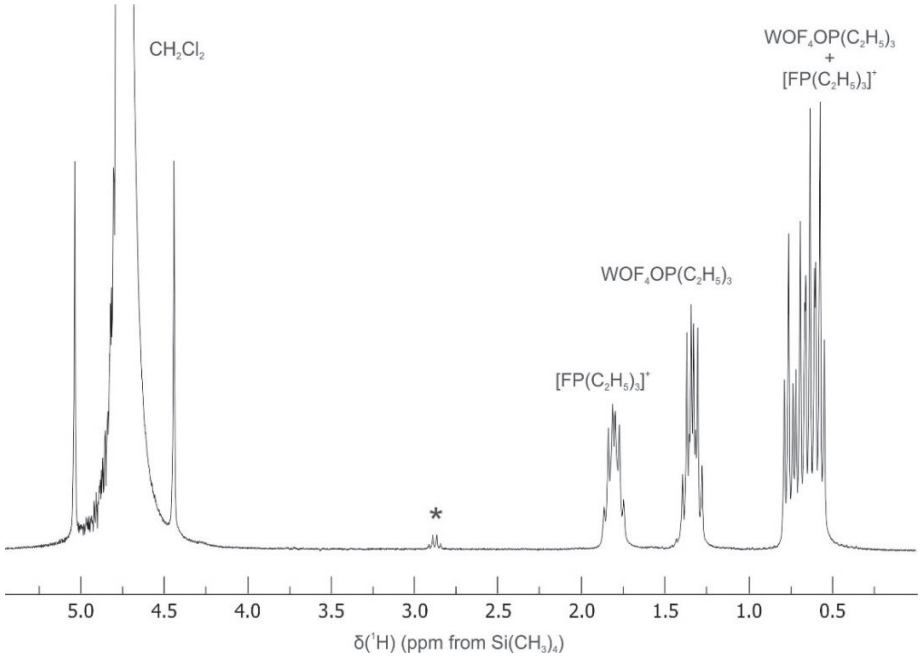

Figure 4.5. ^1H NMR spectrum of the isolated products from the reaction of WF_6 + $OP(C_2H_5)_3$, dissolved in CH_2Cl_2 at 22 °C. Asterisk (*) denotes traces of ethanol on the outside of the sample tube.

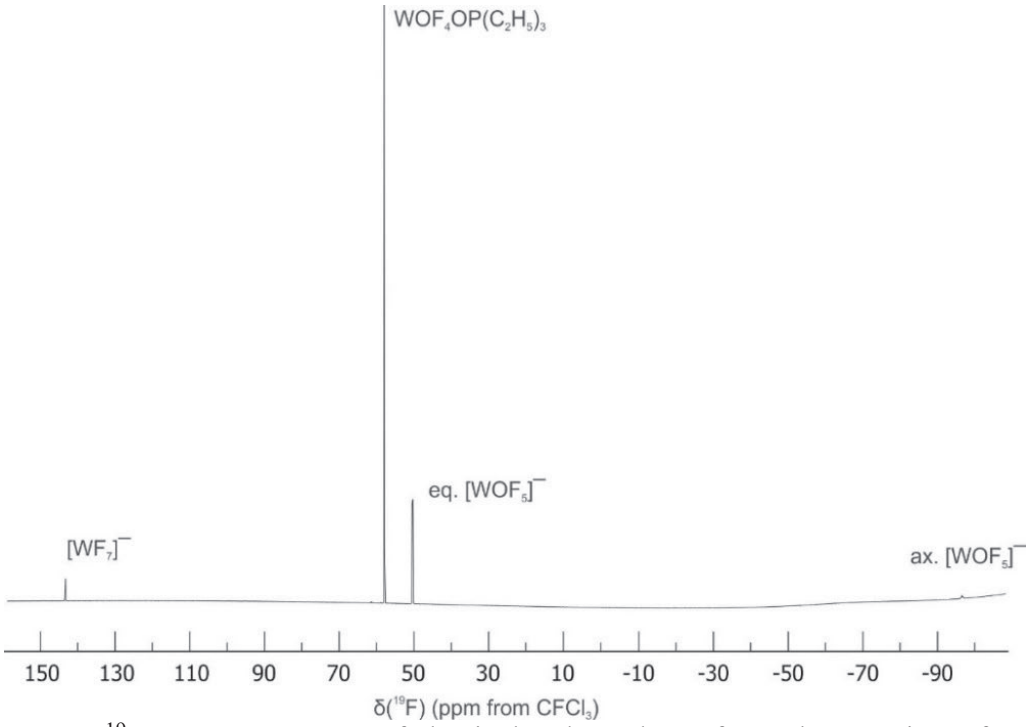

Figure 4.6. ^{19}F NMR spectrum of the isolated products from the reaction of WF_6 + $OP(C_2H_5)_3$, dissolved in CH_2Cl_2 at 22 °C.

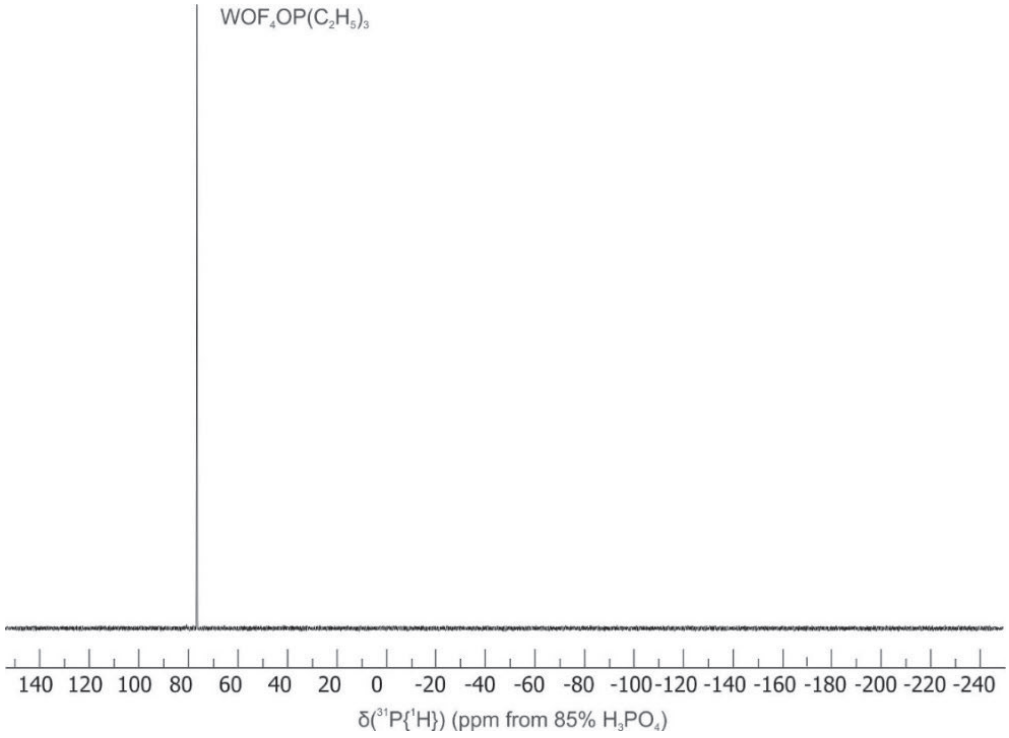

Figure 4.7. $^{31}P\{^{1}H\}$ NMR spectrum of the isolated products from the reaction of WF_6 + $OP(C_2H_5)_3$, dissolved in CH_2Cl_2 at 22 °C.

In an attempt to form the targeted WF_6 phosphine oxide adducts at low temperature, NMR-scale reactions were carried out and kept below –80 °C in an attempt to prevent deoxofluorination (Figures 4.9-11, 13,15). Proton NMR spectroscopy analysis of the reaction of WF_6 with $OP(C_6H_5)_3$ showed a triplet at 6.72 ppm ($^{3}J_{H–H}$ = 7.08 Hz) alongside overlapping multiplets from 6.52 to 6.24 ppm. Free WF_6 was observed at 165.53 ppm ((s) $^{1}J_{W–F}$ = 43 Hz) in the ^{19}F NMR spectrum, due to an excess being used in the sample preparation. The phosphine oxide ligand has almost quantitatively undergone deoxofluorination with large amounts of $[WF_7]^-$ (142.4 ppm), $[W_2O_2F_9]^-$ (F_{term}: (d) 65.1 ppm, $^{2}J_{F–F}$ = 57 Hz, $^{1}J_{W–F}$ = 71 Hz; F_{br}: (sept) –148.2 ppm, $^{2}J_{F–F}$ = 57 Hz) and $[FP(C_5H_6)_3]^+$ ((d) –126.0 ppm, $^{1}J_{P–F}$ = 998 Hz) being observed with only trace amounts of $WOF_4(OP(C_6H_5)_3)$ (59.7 ppm (s), $^{1}J_{W–F}$ = 69 Hz) being observed. The integration of the anionic resonances versus that of $[FP(C_5H_6)_3]^+$ match a molar ratio of 1 : 1. A number of

other trace tungsten fluoride signals were observed at 178.6, 171.3, 63.2 and 57.5 ppm. The $^{31}P\{^{1}H\}$ NMR spectrum confirms the presence of $[FP(C_6H_5)_3]^+$ 95.4 ppm ((d) $^{1}J_{P-F}$ = 1000 Hz), $WOF_4\{OP(C_6H_5)_3\}$ 45.0 ppm (s). Two unknown signals were also present at 55.8 and 50.8 ppm.

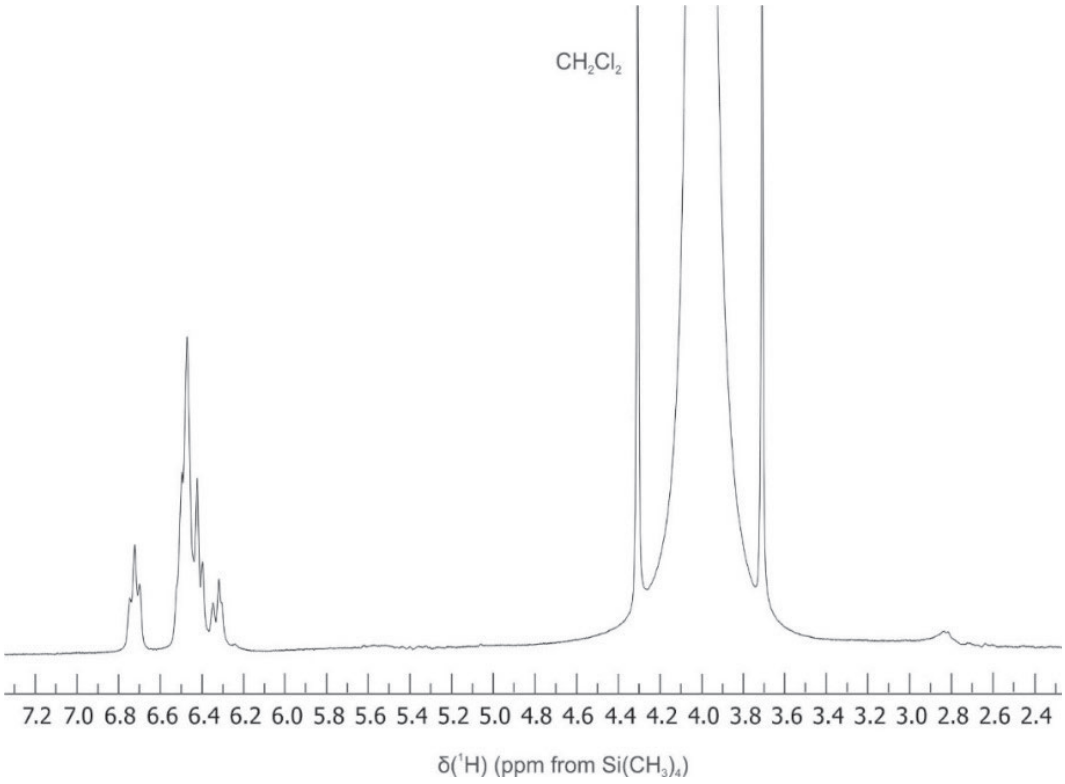

Figure 4.8. ^{1}H NMR spectrum of the reaction of WF_6 with $OP(C_6H_5)_3$ in CH_2Cl_2 at –80 °C.

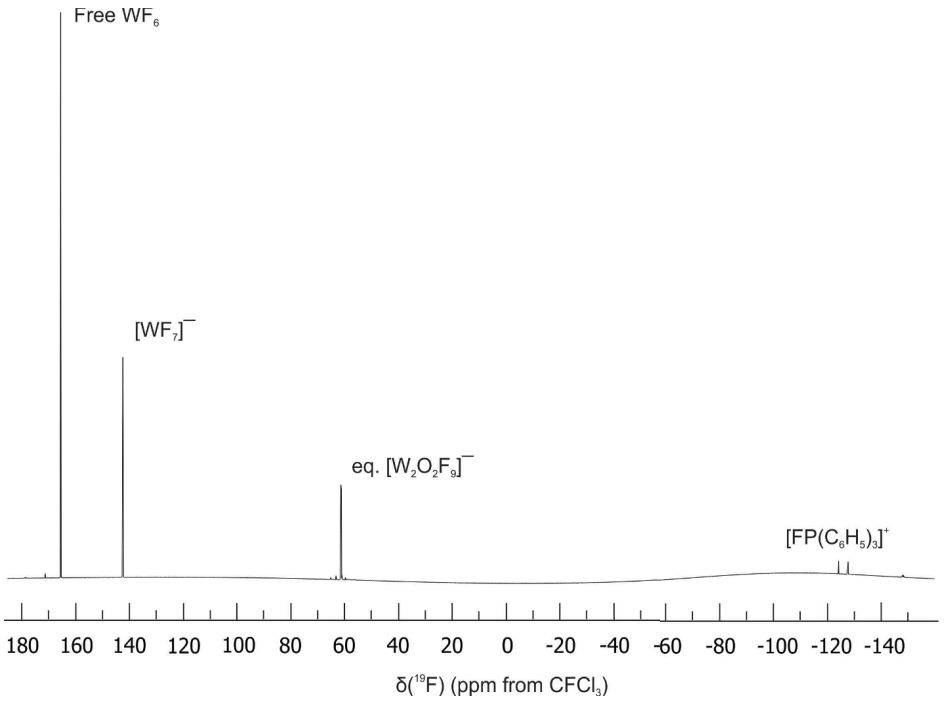

Figure 4.9. ^{19}F NMR spectrum of the products from the reaction of WF_6 with $OP(C_6H_5)_3$ in CH_2Cl_2 at –80 °C.

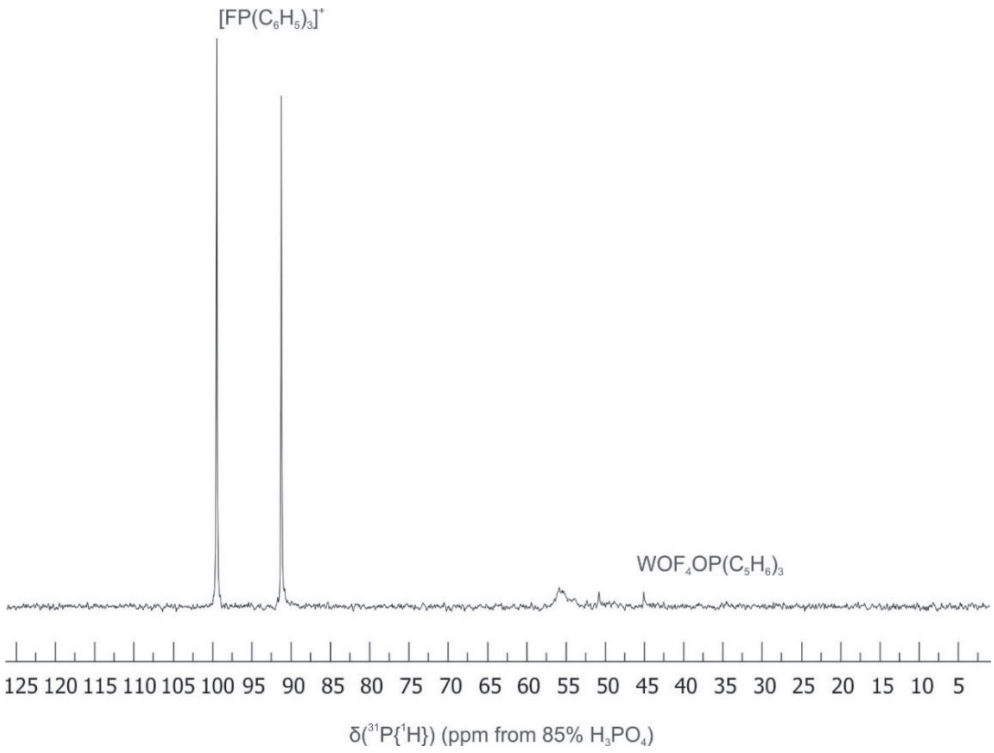

Figure 4.10. $^{31}P\{^1H\}$ NMR spectrum of the products from the reaction of WF_6 with $OP(C_6H_5)_3$ in CH_2Cl_2 at –80 °C.

The ^{1}H NMR spectrum of the reaction of WF_6 with $OP(C_2H_5)_3$ in CH_2Cl_2 at –80 °C showed a multiplet at 0.69 ppm and is assigned to the CH_2 group of $F_2P(C_2H_5)_3$. Another peak at 0.45 ppm was assigned to the CH_2 group of free $OP(C_2H_5)_3$ and overlapping multiplets at –0.11 ppm were assigned as the CH_3 groups of both compounds (Figure 4.11). The resonance at 0.69 ppm likely contains contributions from the $WOF_4\{OP(C_2H_5)_3\}$ adduct, increasing its intensity. The ^{19}F NMR spectrum showed a substantial number of fluorine-containing species; $WOF_4\{OP(C_2H_5)_3\}$ ((s) 57.4 ppm, $^{1}J_{W–F}$ = 70 Hz), $F_2P(C_2H_5)_3$ ((d, sept) –44.0 ppm, $^{1}J_{P–F}$ = 558 Hz, $^{3}J_{F–H}$ = 12 Hz) and $[WOF_5]^-$ (two overlapping sets of multiples: $F_{eq.}$: (dqn) 48.7 ppm $^{2}J_{F–F}$ = 52 Hz, $^{1}J_{W–F}$ = 35 Hz and (d) 49.0 ppm $^{2}J_{F–F}$ = 52 Hz $^{1}J_{W–F}$ = 35 Hz,; $F_{ax.}$: (qn) –91.2 ppm, $^{2}J_{F–F}$ = 52 Hz, and (qn) –91.5 ppm, $^{2}J_{F–F}$ = 52 Hz) were observed to be the major products further supporting Eq. 1-3. The reason for the observation of two sets of multiplets for the $[WOF_5]^-$ anion in an approximate 1 : 1 ratio is not fully understood. A possible explanation for the two sets of anion resonances is that strong ion-pairing with $[FP(C_2H_5)_3]^+$ ((d) –164.0 ppm $^{1}J_{P–F}$ = 952 Hz) could be present for half of the $[WOF_5]^-$, slightly shifting the chemical environments of the anion. The chemical exchange of the ion-pairing would then be sufficiently slow at –80 °C. Ion-pairing could also explain the splitting observed for the $[WF_7]^-$ anion ((s) 142.51 ppm and (s) 142.46 ppm) which usually appears as a singlet. Finally, trace amounts of WF_6 ((s) 163.7 ppm) were also observed.

The new 1 : 2 adduct $WOF_4\{OP(C_2H_5)_3\}_2$ is invoked to explain the remaining ^{19}F resonances at 72.4, 65.3, and –88.9 ppm in a 1 : 2 : 1 ratio of their integrals (Figure 4.13-14). The resonance at 72.4 ppm ((q) $^{2}J_{F–F}$ = 55 Hz) is tentatively assigned to the equatorial fluorine (F_a) of the complex coupling to the two other equatorial fluorines (F_b) and the axial

fluorine (F_c). The F_b fluorines appear as a triplet at 65.3 ppm ($^2J_{F–F}$ = 56 Hz, $^1J_{W–F}$ = 58 Hz) and coupling equally to the other two fluorine environments. The quartet at –88.9 ppm ($^2J_{F–F}$ = 52 Hz) is assigned to the axial fluorine (F_c). So far, such 1 : 2 adducts of WOF_4 have only been observed for pyridine as a base.[18] Finally, the $^{31}P\{^1H\}$ NMR spectrum revealed free $OP(C_2H_5)_3$ ((s) 54.0 ppm, $^1J_{P–C}$ = 66 Hz), $F_2P(C_2H_5)_3$ ((t) –6.6 ppm, $^1J_{P–F}$ = 559 Hz, $^1J_{P–C}$ = 118 Hz), and $[FP(C_2H_5)_3]^+$ at 147 ppm. The $WOF_4(OP(C_2H_5)_3)$ adduct was observed to have shifted to 74.8 ppm ((s) $^1J_{P–C}$ = 66 Hz), with the proposed $WOF_4\{OP(C_2H_5)_3\}_2$ adduct being assigned to the singlet at 79.3 ppm ((s) $^1J_{P–C}$ = 66 Hz). The origin of the remaining ^{31}P resonance at 98.7 ppm ($^1J_{P–C}$ = 66 Hz) is currently unknown.

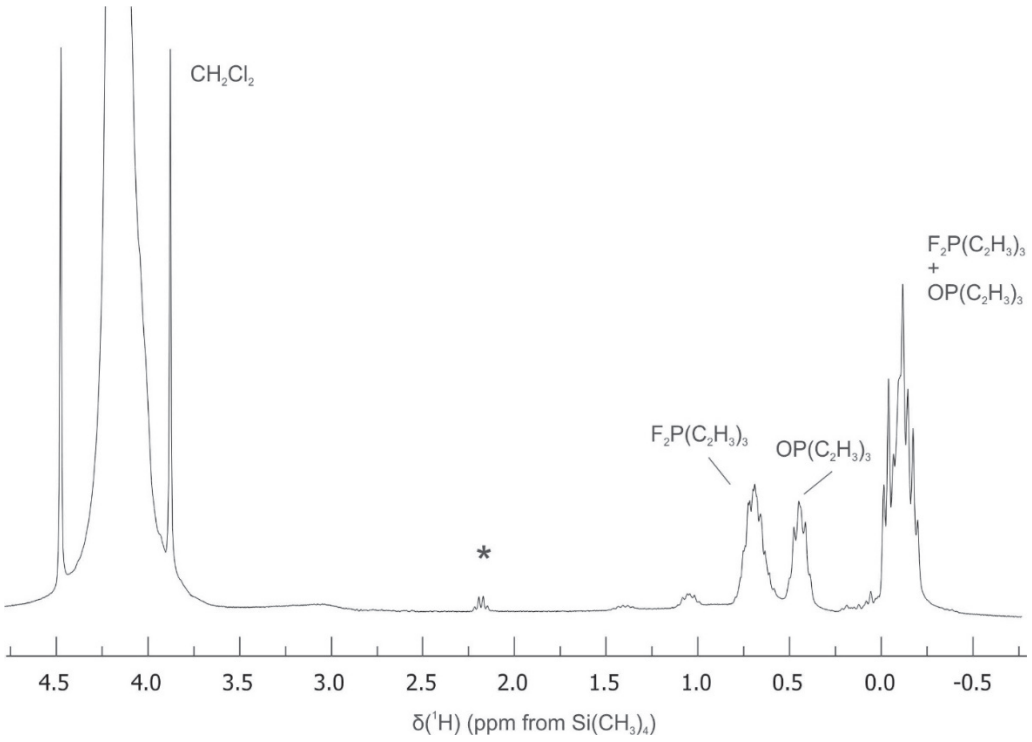

Figure 4.11. ^1H NMR spectrum of the reaction of WF_6 with $OP(C_2H_5)_3$ in CH_2Cl_2 at –80 °C. Asterisk (*) denotes traces of ethanol on the outside of the sample tube.

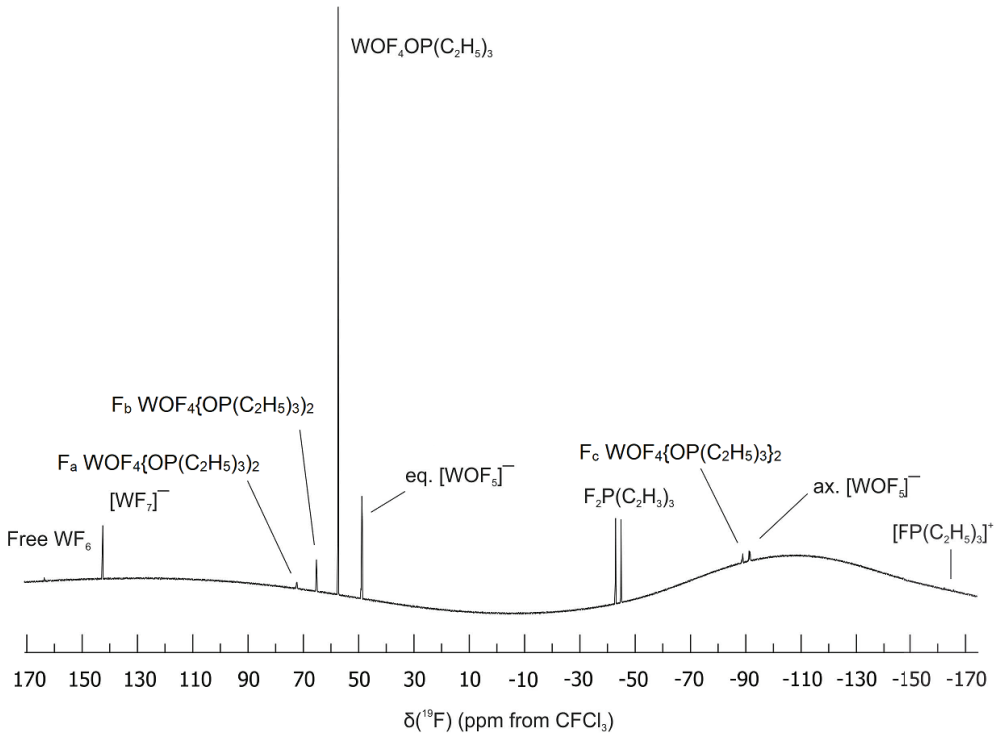

Figure 4.12. ^{19}F NMR spectrum of the reaction of WF_6 with $OP(C_2H_5)_3$ in CH_2Cl_2 at –80 °C.

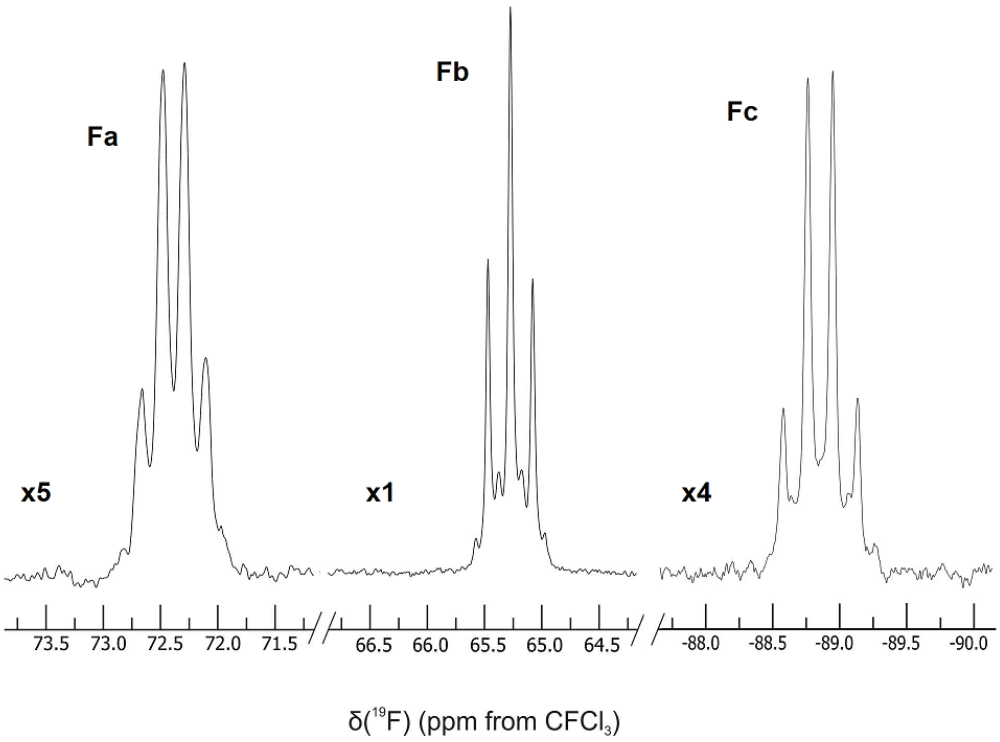

Figure 4.13. Fluorine-19 resonances assigned to the proposed $WOF_4\{OP(C_2H_5)_3\}_2$ adduct in the ^{19}F NMR spectrum of WF_6 with $OP(C_2H_5)_3$ in CH_2Cl_2 at –80 °C.

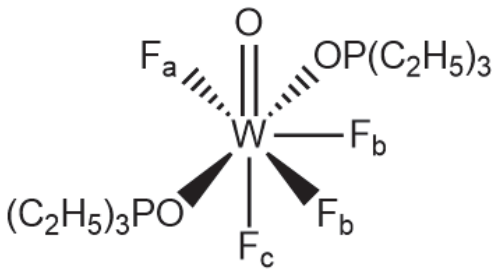

Figure 4.14. Lewis diagram of the proposed $WOF_4\{OP(C_2H_5)_3\}_2$ adduct.

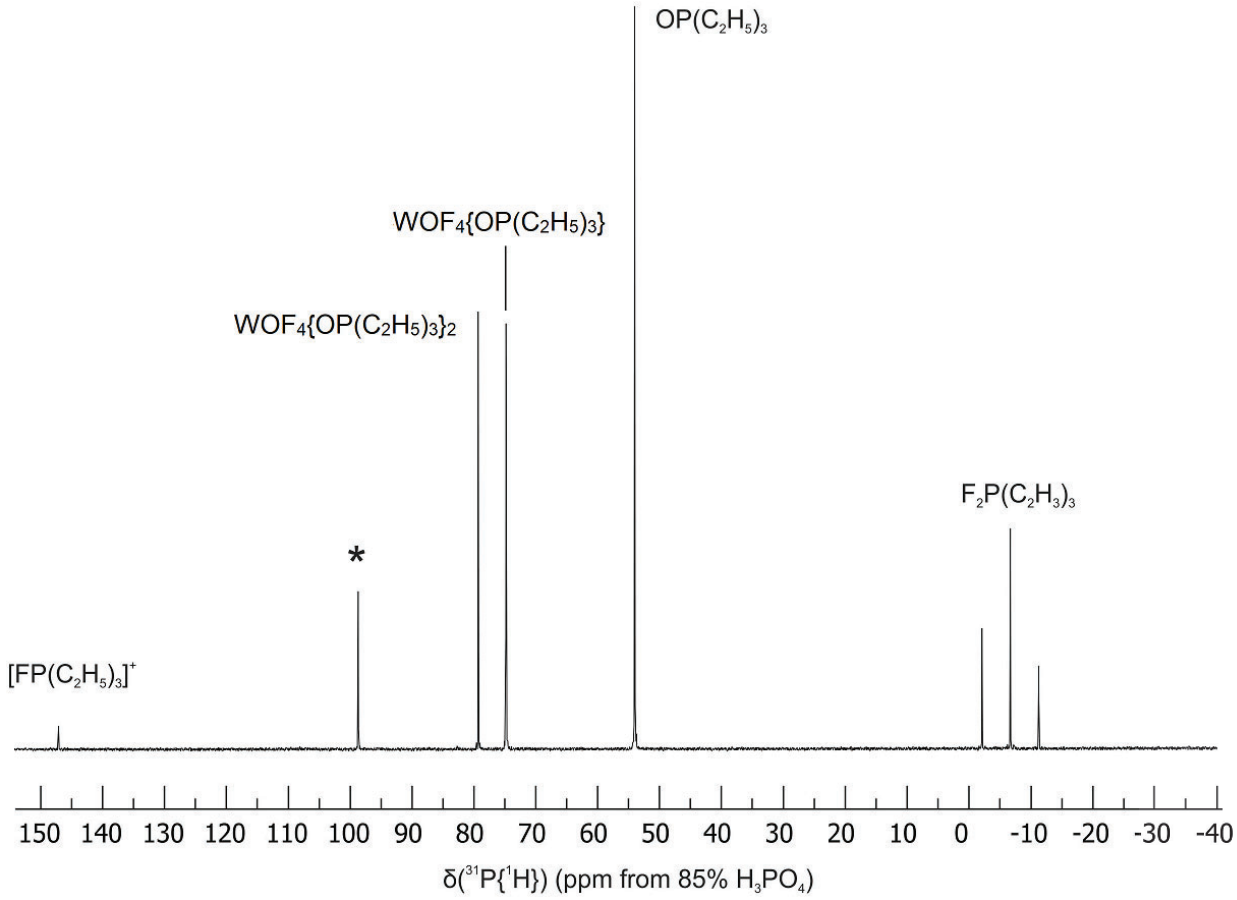

Figure 4.15. $^{31}P\{^1H\}$ NMR spectrum of the products from the reaction of WF_6 with $OP(C_2H_5)_3$ in CH_2Cl_2 at –80 °C. Asterisk (*) an unassigned resonance.

4.2.3. X-ray Crystallography:

Clear colorless prisms coated in white powder were grown at –35 °C from the precipitate recovered from the reaction of WF_6 with $OP(C_6H_5)_3$ being dissolved in the minimum amount of CH_2Cl_2 over the course of 16 h.

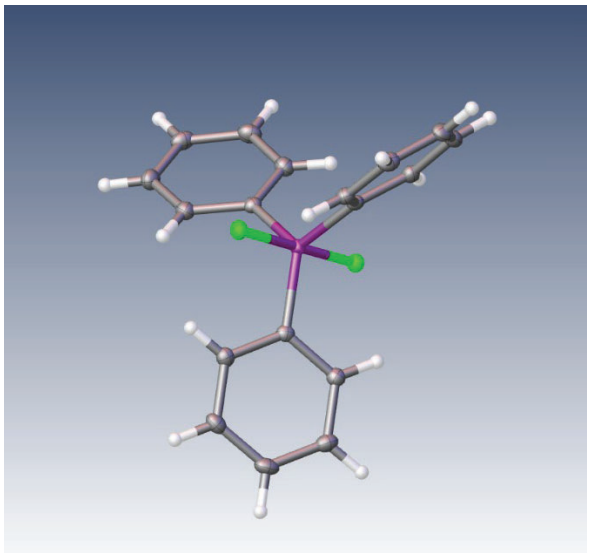

Figure 4.15. Thermal ellipsoid plot (50% probability level) of $F_2P(C_5H_6)_3$.

Table 4.1. Crystallographic Data Collection and Refinement Parameters for $F_2P(C_6H_5)_3$

	$F_2P(C_5H_6)_3$
Identification Code	MG23003
Empirical Formula	$C_{18}H_{15}F_2P$
Formula weight	300.27
Temperature (K)	100.00(10)
Crystal system	Orthorhombic
Space group	*Pbcn*
a (Å)	6.0491(3)
b (Å)	16.4307(9)
c (Å)	14.2421(8)
α (°)	90
β (°)	90
γ (°)	90
Volume (Å^3)	1414.54(13)
Z	4
ρ_{calc} (g cm^{-3})	1.409
μ (mm^{-1})	0.206
F(000)	624.0
Crystal size (mm^3)	0.319 × 0.238 × 0.218
GooF	1.062
Final R indexes [I>=2σ (I)]	R_1[a] = 0.0325, wR_2[b] = 0.0843
Final R indexes [all data]	R_1[a] = 0.0391, wR_2[b] = 0.0872
Largest diff. peak/hole (e Å^{-3})	0.33/–0.33

[a]$R_1 = \sum||F_o| - |F_c||/\sum|F_o|$. [b]$wR_2 = [\sum[w(F_o^2 - F_c^2)^2]/\sum w(F_o^4)]^{1/2}$.

The difluorophosphorane $F_2P(C_6H_5)_3$ crystallizes in the orthorhombic *Pbcn* space group, adopting a trigonal bipyramidal geometry (Figure 4.15). This structure has been observed previously and the data are in good agreement with those reported by Finze *et al.*[23] The compound orientates itself in stacks along the *a* axis with the axial fluorines and phenyl groups slightly offset, with no π-π interactions observed between phenyl rings (Figure 4.16).

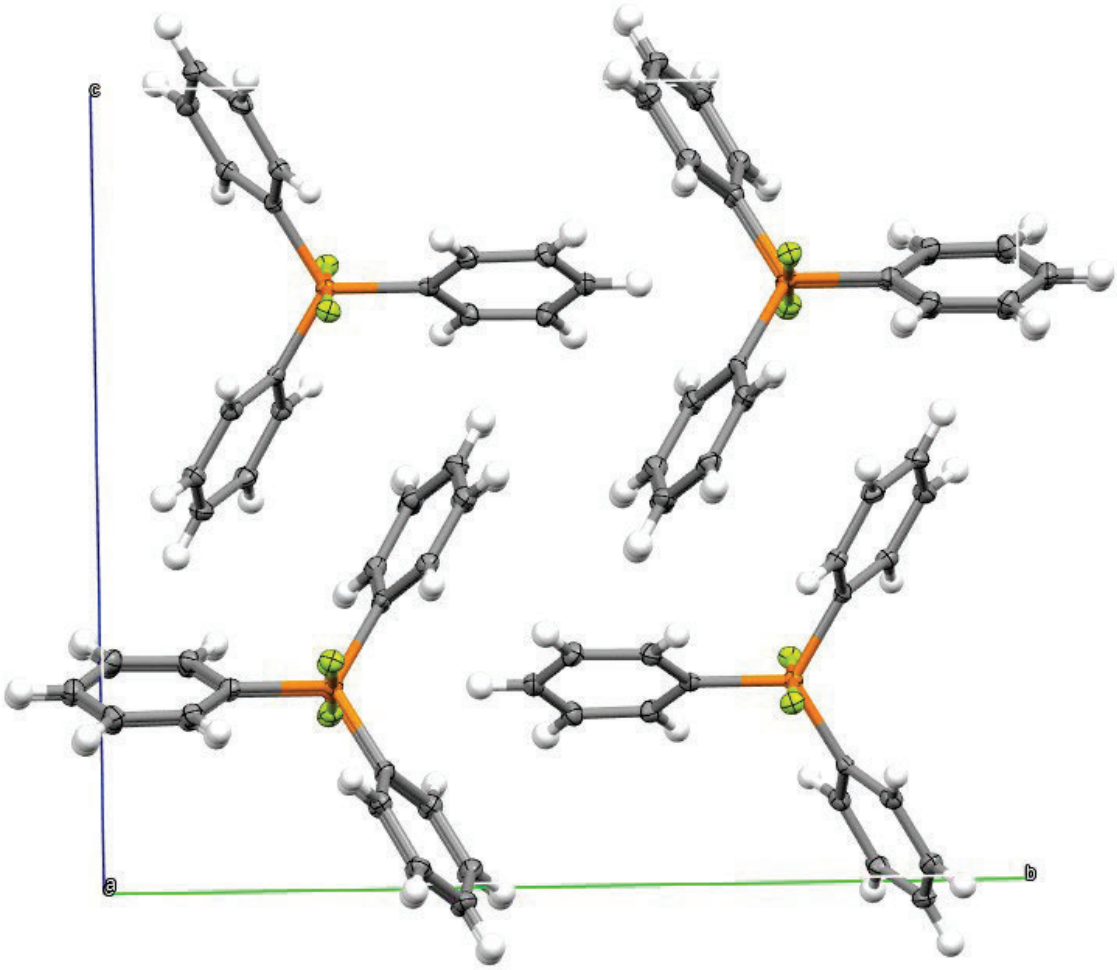

Figure 4.16. Crystal packing diagram of $F_2P(C_6H_5)_3$ viewed down the *a* axis.

4.3. Conclusion

The reactivity of WF_6 towards phosphine oxides was explored utilizing $OP(C_2H_5)_3$ and $OP(C_6H_5)_3$ as ligands. The reactions resulted in deoxofluorination of the ligands to produce fluorophosphoranes and tungsten oxides or the fluorophosphonium cation and fluorido oxo tungstenate anions at ambient temperature. Performing the reaction below –80 °C was ineffective in preventing deoxofluorination, indicating the rapid nature of this reaction and the instability of a transient WF_6 phosphine oxide adduct. The NMR spectra of the WF_6 with $OP(C_2H_5)_3$ at the NMR-scale revealed a large number of products. The

$WOF_4\{OP(C_2H_5)_3\}_2$ adduct is proposed as a side product of the low temperature reaction of WF_6 with $OP(C_2H_5)_3$. This proposed 1 : 2 adduct will need to be confirmed in a future study of reactions of $WOF_4(NCCH_3)$ with excess $OP(C_2H_5)_3$ at low temperatures.

4.4 References

1. Noble, A. M.; Winfield, J. M. Methoxypentafluorotungsten(VI) *J. Chem. Soc.*, Chem. Commun. **1969**, *4*, 151a. DOI: 10.1039/c2969000151a

2. Handy, L. B.; Brinckman, F. E. Chemistry of the Methoxyfluorotungsten(vi) Series *J. Chem. Soc., Chem. Commun.* **1970**, *4*, 214–215. DOI: 10.1039/c29700000214

3. Noble, A. M.; Winfield, J. M. Reactions of Tungsten Hexafluoride with Sulphite Esters and with Trimethyl Phosphite. Preparation and Reactions of Alkoxy- and Phenoxytungsten (VI) Pentafluorides. *J. Chem. Soc. A* **1970**, 501–506. DOI: 10.1039/j19700000501

4. Noble, A. M.; Winfield, J. M. Reactions of Tungsten Hexafluoride with Alkylalkoxy- and Alkylphenoxy-Silanes, Hexamethyldisiloxane, and Dimethyl ETher. *J. Chem. Soc. A* **1970**, 2574. DOI: 10.1039/j19700002574

5. Walker, D. W.; Winfield, J. M. The Fluorination of Methoxy-Groups by Tungsten Hexafluoride. *J. Inorg. Nucl. Chem.* **1972**, *34* (2), 759–762. DOI: 10.1016/0022-1902(72)80458-5.

6. Walker, D. W.; Winfield, J. M. Reactions of Molybdenum Hexafluoride with Compounds Containing Methoxo Groups. *J. Fluorine Chem.* **1972**, *1* (3), 376–378. DOI: 10.1016/S0022-1139(00)83237-6

7. Quiñones, G. S.; Hägele, G.; Seppelt, K. MoF_6 and WF_6: Nonrigid Molecules? *Chem. Eur. J.* **2004**, *10* (19), 4755–4762. DOI: 10.1002/chem.200400095

8. Burns, R. C.; O'Donnell, T. A.; Waugh, A. B. A Specific Method for the Preparation of Many Transition Metal and Actinide Oxide Tetrafluorides. *J. Fluorine Chem.* **1978**, *12* (6), 505– 517. DOI: 10.1016/S0022-1139(00)81093-3

9. Paine, R. T.; McDowell, R. S. Gas-phase Composition and Structure of Metal Oxide Tetrafluorides. *Inorg. Chem.* **1974**, *13* (10), 2366–2370. DOI: 10.1021/ic50140a014.

10. Paine, R. T.; Ryan, R. R.; Asprey, L. B. Synthesis, Characterization, and Structure of Uranium Oxide Tetrafluoride. *Inorg. Chem.* **1975**, *14* (5), 1113–1117. DOI: 10.1021/ic50147a031

11. Bougon, R.; Bui Huy, T.; Charpin, P. Acid Properties of the Oxytetrafluorides of Molybdenum, Tungsten, and Uranium Toward Some Inorganic Fluoride Ion donors. *Inorg. Chem.* **1975**, *14* (8), 1822–1830. DOI: 10.1021/ic50150a016

12. Kanatani, T.; Matsumoto, K.; Hagiwara, R. Syntheses and Physicochemical Properties of Low-Melting Salts Based on VOF_4^- and $MoOF_5^-$, and the Molecular Geometries of the Dimeric $(VOF_4^-)_2$ and $Mo_2O_4F_6^{2-}$ Anions. *Eur. J. Inorg. Chem.* **2010**, *2010* (7), 1049–1055. DOI: 10.1002/ejic.200901099

13. Matsumoto, K.; Hagiwara, R. A New Room Temperature Ionic Liquid of Oxyfluorometallate Anion: 1-Ethyl-3-Methylimidazolium Oxypentafluorotungstate (EMImWOF$_5$). *J. Fluorine Chem.* **2005**, *126* (7), 1095–1100. DOI: 10.1016/j.jfluchem.2005.03.018

14. Mazej, Z.; Gilewski, T.; Goreshnik, E. A.; Jagličić, Z.; Derzsi, M.; Grochala, W. Canted Antiferromagnetism in Two-Dimensional Silver(II) Bis[pentafluoridooxidotungstate(VI)] *Inorg. Chem.* **2017**, *56* (1), 224–233. DOI: 10.1021/acs.inorgchem.6b02034

15. Bortolus, M. R.; Mercier, H. P. A.; Schrobilgen, G. Group 6 Oxyfluoro-Anion Salts of $[XeF_5]^+$ and $[Xe_2F_{11}]^+$: Syntheses and Structures of $[XeF_5][M_2O_2F_9]$ (M=Mo, W), $[Xe_2F_{11}][M'OF_5]$ (M′=Cr, Mo, W), $[XeF_5][HF_2]\cdot CrOF_4$, and $[XeF_5][WOF_5]\cdot XeOF_4$ *J. Chem. Eur. J.* **2020**, *26* (41), 8935–8950. DOI: 10.1002/chem.202000826.

16. Turnbull, D.; Gerken, M. Crystal structure of an Ordered $[WOF_5]^-$ Salt: (1,10-phen-H)[WOF$_5$] (1,10-phen = 1,10-phenanthroline). *Acta. Crystallogr. E* **2020**, *76* (8), 1345–1348. DOI: 10.1107/S2056989020009767

17. Stene, R. E.; Scheibe, B.; Karttunen, A. J.; Petry, W.; Kraus, F. Synthesis and Characterization of A[$W_2O_2F_9$] (A = Li – Cs) *Eur. J. Inorg. Chem.* **2020**, *2020* (23), 2260–2269. DOI: 10.1002/ejic.202000289

18. Arnaudet, L.; Bougon, R.; Ban, B.; Charpin, P.; Isabey, J.; Lance, M.; Nierlich, M.; Vigner, J. Preparation, Characterization, and Crystal Structure of the Adducts $WOF_4\bullet_nC_5H_5N$ (n = 1, 2). *Inorg. Chem.* **1989**, *28* (2), 257–262. DOI: 10.1021/ic00301a020.

19. Arnaudet, L.; Bougon, R.; Ban, B.; Lance, M.; Nierlich, M.; Vigner, J. Preparation, Characterization, and Crystal Structure of the Adducts WF_6•F-py and WOF_4•F-py (F-py = 2-Fluoropyridine). *Inorg. Chem.* **1993**, *32* (7), 1142–1146. DOI: 10.1021/ic00059a020

20. Levason, W.; Reid, G.; Zhang, W. Coordination Complexes of the Tungsten(VI) Oxide Fluorides WOF_4 and WO_2F_2 with Neutral Oxygen- and Nitrogen-donor Ligands. *J. Fluorine Chem.* **2016**, *184*, 50–57. DOI: 10.1016/j.jfluchem.2016.02.003

21. Laurence, C. and Gal, J.–F. The BF_3 Affinity Scale. In *Lewis Basicity and Affinity Scales Data and Measurement*; John Wiley and Sons, Ltd., 2010; pp 85-109.

22. Turnbull, D. *Lewis–Acid Behaviour of Neutral and Cationic Fluoridotungsten(V) and (VI) Complexes*, Ph.D. Thesis, University of Lethbridge, Lethbridge, AB, **2020**.

23. Schneider, L. N.; Krauel, E.-V. T, Deutsch, C.; Urbahns, K.; Bischof, T.; Maibom, K. A. M., Landmann, J.; Keppner, F.; Kerpen, C.; Hailmann, M.; Zapf, L.; Knuplez, T.; Bertermann, R.; Ignat'ev, N. V., Finze, M. Stable and Storable $N(CF_3)_2$ Transfer Reagents *Chem. Eur. J.* **2021**, *27* (42), 10973–10978. DOI: 10.1002/chem.202101436

Chapter 5 – Lewis Acidity of WF_6 Towards Tridentate Terpyridine

5.1 Introduction

Tungsten hexafluoride is one of the nine confirmed transition metal hexafluorides and is widely used outside of the laboratory setting. First made by Malm *et al.* in 1958 by subjecting the pure metal to elemental fluorine, the compound has been utilized in chemical vapor deposition.[1] In the semiconductor industry, the compound is reduced with silicon, hydrogen gas, and various hydrides to form tungsten films integral to the manufacturing of integrated circuits.[2] Tungsten hexafluoride has also found use in the manufacturing of tungsten carbides when reduced with dimethyl ether and hydrogen gas, with the resulting compound being used in milling bits, armor piercing rounds, tire studs and jewellery.[3-7]

Tungsten hexafluoride has demonstrated unique properties further differentiating it from the other transition metal hexafluorides. Alongside molybdenum, technetium and rhenium hexafluorides, tungsten hexafluoride is capable of forming $[MF_7]^-$ and $[MF_8]^{2-}$ complex fluoride anions.[1,8-9] Among the metal hexafluorides, WF_6 possesses the lowest electron affinity.[10-12] As a consequence, tungsten hexafluoride is the weakest oxidizer of the metal hexafluorides being incapable of oxidizing NO.[13] This lack of oxidizing strength has been key in exploring and developing numerous stable WF_6 complexes with organic bases such as pnictogen-based and chalcogen-based ligands.

Bidentate ligands are well known to induce autoionization of neutral WF_6. In 1992, Bougon *et al.* found that bipy causes ligand-induced autoionization in the presence of a slight excess of WF_6, leading to the formation of the $[WF_4(bipy)_2]^{2+}$ dication and $[WF_7]^-$

.[14] This cationic species was found to adopt a trigonal dodecahedral geometry in the solid state. In 2018, Levason *et al.* examined bidentate phosphorus and arsenic bases, *i.e.*, *o*-$C_6H_4(E)_2$ (E = $P(CH_3)_2$, $As(CH_3)_2$) and $(CH_3)_2PCH_2CH_2P(CH_3)_2$.[15] Unlike for the pyridine-based bidentate ligands, these species were found to readily induce autoionization even with stoichiometric amounts of WF_6.[15] Similar to the bipyridine dicationic species, crystal structures of the $[WF_4\{o\text{-}C_6H_4(E(CH_3)_2)_2\}_2]^{2+}$ (E = P, As) dications showed trigonal dodecahedral cation coordination geometries.

However, with the careful control of stoichiometry, isolation of neutral WF_6 adducts with bidentate pyridine ligands is possible. Bougon *et al.* were able to characterize WF_6(bipy) via Raman and IR spectroscopy in 1992.[14] In 2019, Gerken *et al.* were able to replicate these results and studied this adduct in more detail, as well as characterize WF_6(phen) by vibrational spectroscopy and computational analysis.[16] Gas-phase geometry optimizations of the compounds revealed that, unlike $WF_6(py)_n$ (n = 1,2) which were found to be capped trigonal prismatic, these species adopted distorted trigonal dodecahedral geometries.[16-17] Additionally, it was found that the presence of ligands allowed the metal center to relinquish a fluoride to a sufficiently strong Lewis acid, such as SbF_5, to form the $[WF_5(L–L)]^+$ (L–L = bipy, phen) cations. While the hepta-coordinate cations can be described as monocapped octahedral, closer structural analysis found that they can be better described as 4 : 3 polyhedra.[16]

Investigation of fluoride abstraction of WF_6 stabilized by monodentate ligands was conducted by the Gerken group in 2020. Herein, $WF_6(py)_2$ was reacted with $[(CH_3)_3Si(py)][O_3SCF_3]$, allowing for the isolation and characterization of $[WF_5(py)_3][O_3SCF_3]$. Utilizing variable-temperature ^{19}F NMR spectroscopy in conjunction

with DFT calculations allowed for the determination of a trigonal dodecahedral cation coordination geometry about tungsten. Attempts to synthesize $[WF_5(py)_2][X]$ ($X = O_3SCF_3$, SbF_6) that contained a hepta-coordinate cation were unsuccessful as the cation was found to be too unstable, capable of undergoing dismutation and subsequent redox decomposition with excess pyridine to form $W^{(V)}F_5(py)_2$.[18] Fluoride abstraction of $WF_5(py)_2$, however, was achieved utilizing $[(CH_3)_3Si(py)][O_3SCF_3]$ in pyridine solvent to produce $[WF_4(py)_4][O_3SCF_3]$. The use of WF_6, $(CH_3)_3SiO_3SCF_3$, and $P(CH_3)_3$ as the reducing agent, ligand, and solvent, respectively, yielded $[W^{(V)}F_4\{P(CH_3)_3\}][O_3SCF_3]$.[19] The crystal structure of both compounds contained square antiprismatic cations, which served to develop the τ_8 and τ_8' geometry indices.

While tungsten has been shown to exhibit coordination numbers of up to eight, the ability of WF_6 to donate a fluoride ion under the right conditions could be exploited to coordinate ligands of higher denticity, such as 2,2′:6′,2′′-terpyridine (terpy). Indeed, $[WF(terpy)_2]^+$ has been synthesized by Weighart *et al.* in 2013 via accidental fluorination of $W(terpy)_2$ using $AgPF_6$ in CH_2Cl_2, showing that terpy can coordinate to tungsten in high oxidation states.[20] However, the group was unable to conclusively determine the oxidation state of the metal centre due to the redox-non-innocence of the terpy ligand. Pyridine and ligands such as bipy and terpy can accept an electron, resulting in the oxidation of an electron-rich metal center, but without any changes of the overall charge of the complex, thus leading to the ambiguity.

Herein, we report the synthetic route of octa-coordinate $[WF_5]^+$ stabilized by neutral tridentate terpyridine, exploiting the capability of tungsten hexafluoride to undergo ligand-

induced autoionization. In this Chapter, the synthesis and structural characterization are detailed, alongside vibrational and NMR spectroscopic characterization.

5.2 Results and Discussion

5.2.1 Synthesis and Properties of $[WF_5(terpy)][WF_7]$ and $[WF_5(terpy)][SbF_6]$

The reaction of terpy with 2 equivalents of WF_6 was carried out in SO_2, resulting in a red solution (Eq. 5.1). Removal of volatiles produced an orange powder of $[WF_5(terpy)][WF_7]$ in near quantitative yield. No evidence of further fluoride abstraction was shown utilizing and additional equivalent of WF_6. Reacting the salt with the strong Lewis acid SbF_5SO_2 allowed for WF_6 in $[WF_7]^-$ to be displaced by the stronger Lewis acid SbF_5, resulting in $[SbF_6]^-$ anion formation [Eq. (5.2)]. The by-products of WF_6 and SO_2 are sufficiently volatile, allowing them to be removed under reduced pressure upon warming to ambient temperature.

$$2WF_6 + terpy \rightarrow [WF_5(terpy)][WF_7] \quad (5.1)$$

$$[WF_5(terpy)][WF_7] + SbF_5SO_2 \rightarrow [WF_5(terpy)][SbF_6] + SO_2 + WF_6 \quad (5.2)$$

Dissolving the $[WF_5(terpy)][WF_7]$ salt in either CH_3CN or CH_2Cl_2 resulted in clear, red solutions. Attempts to use anhydrous HF as a solvent resulted in the insoluble salt turning yellow and then to a white powder upon agitation, suggesting decomposition. Use of $WF_6(py)$ as a starting material was explored as the solid could allow for better control of stoichiometry; however, the reaction resulted in a black powder that was insoluble in SO_2, CH_3CN, and CH_2Cl_2.

5.2.2 Crystal Structure of $[WF_5(terpy)][WF_7]\cdot SO_2$

Orange plate-like crystals of $[WF_5(terpy)][WF_7]\cdot SO_2$ (Figure 5.1.) were grown from a concentrated solution in SO_2 at –45 °C over 16 h. The $[WF_5(terpy)][WF_7]$ salt crystallized in the triclinic $P\bar{1}$ space group with one co-crystallized SO_2 molecule in the asymmetric unit (Figure 5.1). Selected crystallographic data are listed in Table 5.1, while selected bond lengths and angles are given in Table 5.2.

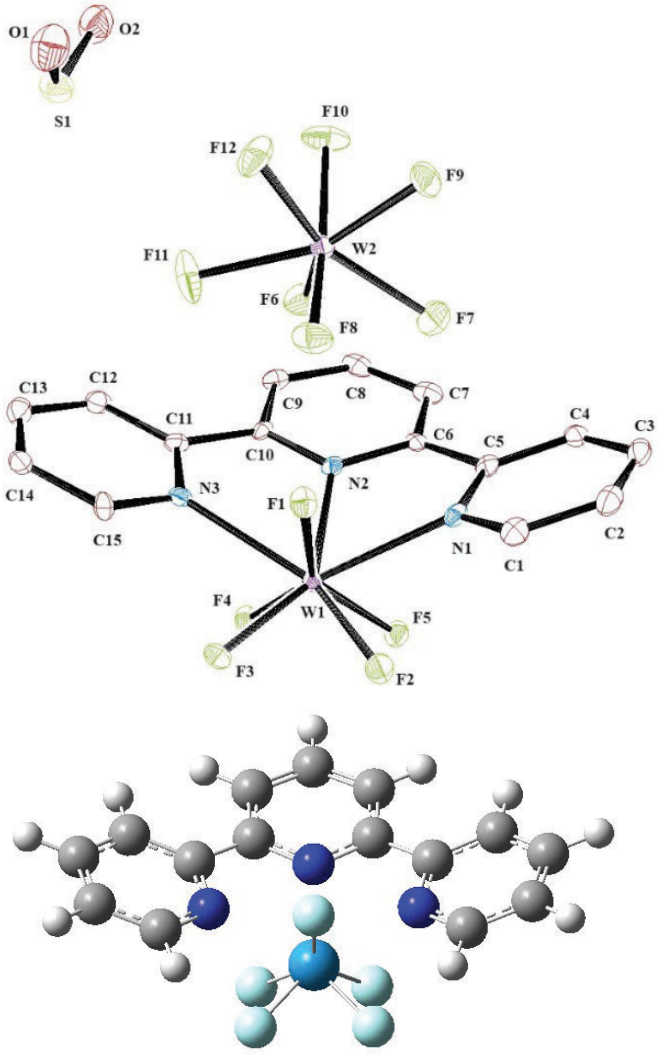

Figure 5.1. Thermal ellipsoid plot (50% probability level) with hydrogens omitted for clarity of the asymmetric unit of $[WF_5(terpy)][WF_7]\bullet SO_2$ (top) and B3LYP/def2-TZVPPD optimized gas-phase structure of $[WF_5(terpy)]^+$ (bottom).

Table 5.1 Crystallographic Data Collection and Refinement Parameters for $[WF_5(terpy)][WF_7]\bullet SO_2$

	$[WF_5(terpy)][WF_7]\bullet SO_2$
Identification Code	MG23016B
Empirical Formula	$C_{15}H_{11}F_{12}N_3O_2SW_2$
Formula weight	893.03
Temperature (K)	100.01(10)
Crystal system	Triclinic
Space group	$P\bar{1}$
a (Å)	9.5761(2)
b (Å)	9.6787(2)
c (Å)	12.0343(2)
α (°)	71.722(2)
β (°)	75.886(2)
γ (°)	86.985(2)
Volume (Å^3)	1026.80(4)
Z	2
ρ_{calc} (g cm^{-3})	2.888
μ (mm^{-1})	11.424
F(000)	820.0
Crystal size (mm^3)	0.42 × 0.32 × 0.23
GooF	1.095
Final R indexes [I>=2σ (I)]	R_1 = 0.0224, wR_2 = 0.0545
Final R indexes [all data]	R_1 = 0.0241, wR_2 = 0.0553
Largest diff. peak/hole (e Å^{-3})	1.79/–1.29

[a] $R_1 = \sum||F_o| - |F_c||/\sum|F_o|$. [b] $wR_2 = [\sum[w(F_o^2 - F_c^2)^2]/\sum w(F_o^4)]^{1/2}$.

Table 5.2. Selected experimental and Calculated Bond Lengths[a] [Å; given in square brackets] of $[WF_5(terpy)][WF_7]\bullet SO_2$

	$[WF_5(terpy)][WF_7]\bullet SO_2$
W1–F1	1.874(3) [1.881]
W1–F2	1.896(3) [1.870]
W1–F3	1.883(3) [1.870]
W1–F4	1.897(3) [1.890]
W1–F5	1.885(3) [1.890]
W1–N1	2.271(4) [2.352]
W1–N2	2.162(4) [2.244]
W1–N3	2.278(4) [2.352]
C5–C6	1.457(7) [1.463]
C10–C11	1.449(7) [1.463]
W2–F6	1.884(3)
W2–F7	1.863(3)
W2–F8	1.850(3)
W2–F9	1.894(3)
W2–F10	1.851(3)
W2–F11	1.897(3)
W2–F12	1.915(3)

[a] Calculated at the B3LYP/aVTZ level of theory.

While the ions pack into layers, the cations do not orient themselves to allow for π-π interactions between the terpy rings, presumably due to the repulsion of the cations. Interactions between anions and cations are not observed because of the coordinative saturation of the tungsten centres in the anion and cation. The $[WF_7]^-$ anion has a distorted monocapped octahedral structure, which has been previously observed in the $[Cs][WF_7]$ crystal structure.[8] The distance between the S1 of SO_2 and F12 of the $[WF_7]^-$ anion is 2.788(4) Å, which is shorter than the sum of the van der Waals radii (F: 1.47 Å, S: 1.80 Å, S–F: 3.27 Å), suggesting the solvent's role in crystal formation.[21] The geometry of the octacoordinated cations was determined with the use of the τ_8 geometry index, where α and β are angles of non-adjacent L–W–L units (Eq. 5.3).[18]

$$\tau_8 = \left|\frac{\alpha-\beta}{129.8-97.1}\right| = \left|\frac{\alpha-\beta}{32.7}\right| \quad (5.3)$$

By choosing any one ligand atom (L1), finding the third largest L1–M–L2 angle (α), and the angle between the two closest ligands to these (L3–M–L4, β), the value for τ_8 was obtained to differentiate between the trigonal dodecahedral, square antiprismatic, or bicapped trigonal prismatic geometries. In an ideal hard-sphere model, these angles would be 129.8° and 97.1° in the trigonal dodecahedral geometry resulting in a τ_8 value of 1, whereas a value of 0° would be obtained for square antiprismatic geometry, where $\alpha = \beta$. Meanwhile, calculations should be carried out on the 'top' and 'bottom' sets of ligands as the bicapped trigonal prismatic geometries will possess a 'face' with a value of 1 and the opposing 'face' with a value of 0. Utilizing the angles of N1–W1–N3(α1) and F1–W1–N2(β1) for the 'top' face as well as F2–W1–F4(α2) and F3–W1–F5(β2) for the 'bottom' yields τ_8 values of 0.94 and 0.06, respectively, clearly indicating a bicapped trigonal prismatic geometry. This geometry contrasts the trigonal dodecahedral geometry of $[WF_5(py)_3]^+$ as the monodentate ligands are not geometrically constrained to one another. The W–F bond lengths within the $[WF_5(terpy)]^+$ cation range from 1.874(3) to 1.897(3) Å, with the shortest bond being the W–F1 bond. These values are, on average, larger than those in most other fluoridotungsten(VI) complexes and are similar to those in the neutral $WF_6(py)_2$ complex (Table 5.3). This reflects an increase in electron donation from the ligand to the metal center and the higher coordination number. Meanwhile, the W–N bond lengths in the $[WF_5(terpy)]^+$ cation (2.162(4)-2.278(4) Å) vary largely within the complex due to the N-donor atoms occupying both the capping and non-capping positions. The capping W–N bonds (2.271(4) and 2.278(4) Å) are longer than those in other cationic fluoridotungsten(VI) complexes species (Table 5.3) and are most similar to that of the neutral hepta-coordinate $WF_6(py)$. Conversely, the non-capping W–N bond (2.162(4) Å) is significantly shorter compared to all other fluoridotungsten(VI) complexes. The angle

between the plane of the N3 ring and the plane of the N1 ring was found to be 144.61°, reflecting the difference in coordination sites of the capping N1 and N3 atoms and the non-capping central N2.

Table 5.3 Ranges of select experimental bond lengths of various W(VI) fluorido species with pyridine-based ligands.

	W–F (Å)	W–N (Å)	C_{py}–C_{py} (Å)
$[WF_5(terpy)][WF_7]$	1.874(3)-1.897(3)	2.162(4)-2.278(4)	1.449(7),1.457(7)
$[WF(terpy)_2][PF_6]$[a]	2.0291(18)	2.066(3)-2.176(3)	1.439(5),1.441(4)
$[WF_5(phen)][SbF_6]$[b]	1.832(3)-1.861(3)	2.223(4)-2.229(3)	1.415(6)[(e)]
$[WF_5(phen)][Sb_2F_{11}]$[b]	1.8377(19)-1.860(2)	2.230(3)-2.240(3)	1.408(5)[(e)]
$[WF_5(bipy)][Sb_2F_{11}]$[b]	1.838(3)-1.854(3)	2.224(4)-2.234(4)	1.461(8)
$WF_6(py)$[c]	1.843(5)-1.875(5)	2.251(7)	N/A
$WF_6(py)_2$[d]	1.883(6)-1.900(5)	2.344(6)	N/A

[a] Ref. 20 [b] Ref. 16. [c] Ref. 22. [d] Ref. 17. [e] Bond length of the C5–C6 atoms.

Gas-phase density functional theory (DFT) optimizations on the $[WF_5(terpy)]^+$ cation used the bicapped trigonal prism and trigonal dodecahedron as starting point geometries. In both cases, the resulting structure adopted the bicapped trigonal prismatic geometry upon optimization (Figure 5.1 and Table 5.2). Overall, the calculated W–N bond lengths are overestimating the experimental values, leading to an underestimation of the W–F bond lengths. Nevertheless, the τ_8 values for the optimized structure of 1.08 and 0.01 are in good agreement with values obtained from the crystal structure.

Weighart *et al.* previously synthesized several terpy complexes with transition metals in lower oxidation states.[(20)] In compounds such as $[WF(terpy)_2]^+$ determination of the oxidation state appeared to be complicated due to the redox non-innocence of the terpy ligand, which is capable of accepting one or more electrons. Reduction of $bipy^0$ to either

bipy^{1-} or bipy^{2-} causes a shortening of the interpyridine C_{py}–C_{py} bonds, allowing for possible determination of the ligand's oxidation state via crystallography. While this trend also applies to terpy, the changes of distances between these bonds are smaller requiring higher-quality crystal structures.[20] This resulted in the group tentatively assigning the cation as $[W^{(V)}F(tpy^{\bullet-})(tpy^{2-})]$, but stating it could not rule out $[W^{(VI)}F(tpy^{2-})_2]^+$ or $[W^{(IV)}F(tpy^{\bullet-})_2]^+$. With the isolation of the $[WF_5(terpy)]^+$ salt comparisons to $[WF(terpy)_2]^+$ can be established. Considering the C_{py}–C_{py} bonds in the $[WF_5(terpy)][WF_7]$ salt (1.449(7), 1.457(7) Å), the bond lengths are indistinguishable from those of $[WF(terpy)_2]^+$ (1.439(5), 1.441(4) Å) because of the large standard deviations. When directly comparing the central or capping W–N bonds, the $[WF(terpy)_2]^+$ cation reflects the charged nature of the terpy moiety with bonds of 2.066(3)-2.176(3) Å that are shorter than those of the $[WF_5(terpy)]^+$ cation (2.162(4)-2.278(4) Å), suggesting that the former forms stronger dative W–N bonds. This also explains the difference in W–F bond lengths between the species as the increased electron donation of the terpy ligands in $[WF(terpy)_2]^+$ (W–F: 2.0291(18) Å) would result in a substantially longer W–F bond compared to $[WF_5(terpy)][WF_7]$ (1.874(3)-1.897(3) Å).

5.2.3 Raman Spectroscopy of $[WF_5(terpy)][X]$ (X = WF_7, SbF_6)

The Raman spectra of the $[WF_5(terpy)][WF_7]$ and $[WF_5(terpy)][SbF_6]$ salts were recorded at room temperature (Figure 5.2-3). Vibrational frequencies of the geometry-optimized cation were calculated at the B3LYP/def2-TZVPPD level of theory. The calculated vibrational frequencies are in good agreement with the experimental Raman frequencies with their assignments, alongside that of free terpy, being listed in Table 5.4.

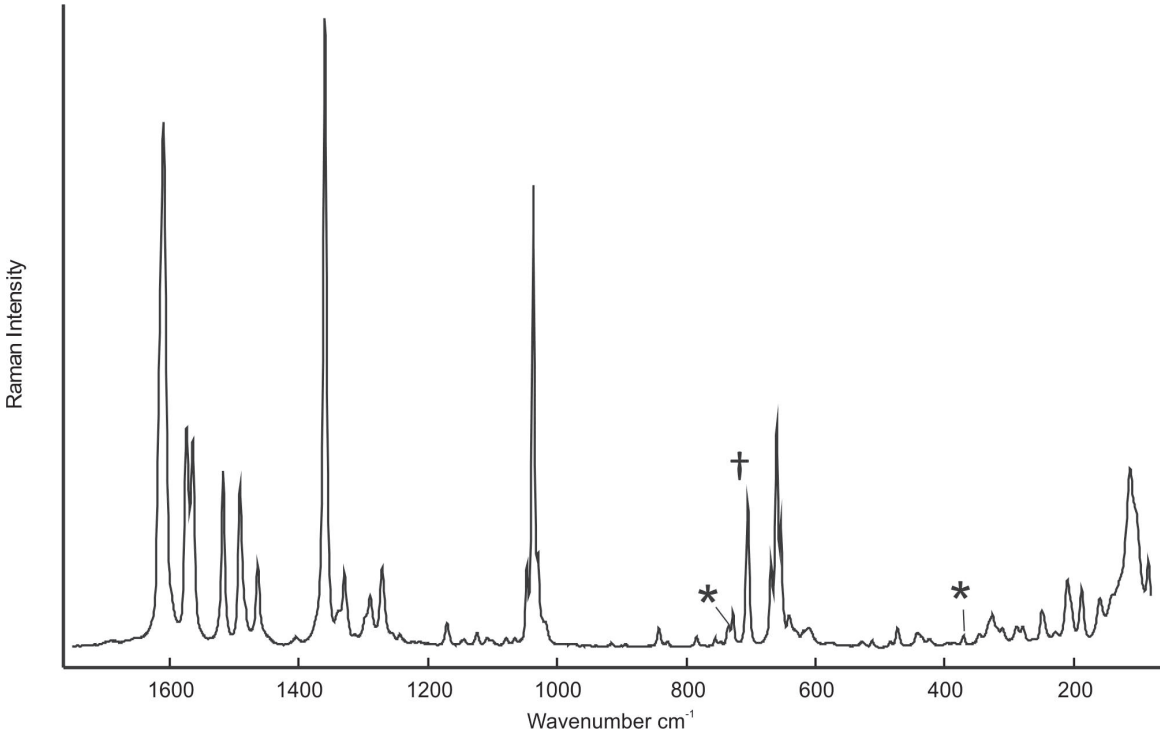

Figure 5.2 Raman spectrum of $[WF_5(terpy)][WF_7]$ at ambient temperature. FEP bands (*) observed at 735 and 385 cm^{-1} and $[WF_7]^-$ band (†) observed at 705 cm^{-1}.

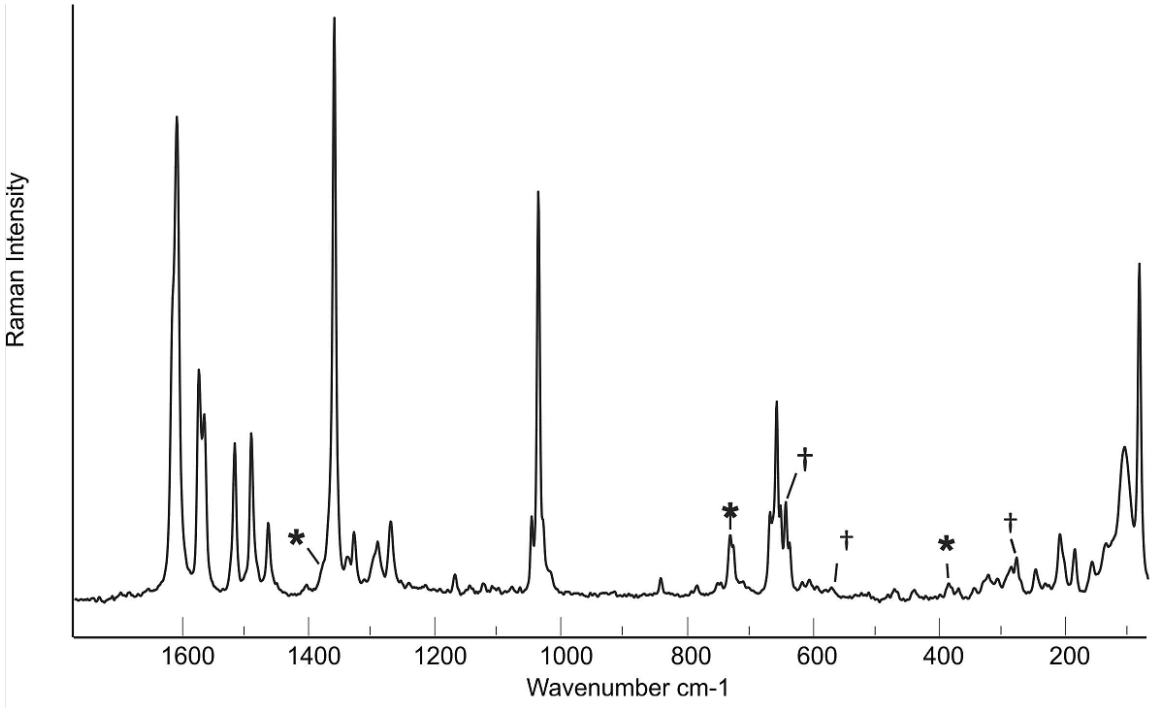

Figure 5.3 Raman spectrum of $[WF_5(terpy)][SbF_6]$ at ambient temperature. FEP bands (*) observed at 1380, 735 and 385 cm^{-1}. $[SbF_6]^-$ bands (†) are observed at 645, 573 and 280 cm^{-1}.

Table 5.4 Observed Raman and calculated vibrational frequencies (cm^{-1}) of free terpy and $[WF_5(terpy)][X]$ (X = WF_7, SbF_6).

terpy		$[WF_5(terpy)][WF_7]$[a,b]	$[WF_5(terpy)][SbF_6]$[a,c]	$[WF_5(terpy)]^+$	
exptl	calcd	exptl	Exptl	Calcd[d]	Assignments[e]
3011(3)	3150(142)[29]	3151(1)		3239(247)[8]	
	3149(81)[16]			3239(19)[1]	
3087(3)	3204(439)[7]	3122(2)		3236(220)[3]	
	3201(40)[27]			3235(83)[1]	
3073sh	3200(270)[4]	3109(2)		3224(158)[<1]	
	3194(84)[13]			3224(17)[2]	C-H stretching modes
3061(11)	3197(132)[<1]	3097(1)	3093(4)	3220(162)[<1]	
	3193(24)[21]			3220(87)[1]	
3052(8)	3178(48)[10]			3207(111)[<1]	
	3177(67)[12]			3204(57)[2]	
3042sh	3176(169)[<1]	3060(1)		3204(154)[<1]	
1646(3)		1691(1)			
1620(7)	1629(149)[106]			1655(6)[17]	
1609(10)	1630(391)[5]			1646(143)[22]	
	1621(116)[21]	1611(84)	1610(83)	1644(501)[62]	
1594(61)	1624(133)[39]			1623(48)[16]	
	1613(6)[39]	1574(35)	1575(39)	1621(188)[3]	
1574(100) 1561 sh	1608(76)[43]	1565(33)	1566(32)	1605(305)[72]	
1478(30)	1515(71)[2]	1517(29)	1518(26)	1545(181)[30]	
1470(31)	1509(64)[22]	1491(26)	1492(27)	1526(143)[54]	
1454(21)	1482(99)[9]	1464(8)	1465(13)	1503(100)[11]	
1439(15)	1480(23)[82]	1448 sh		1496(10)[123]	C–C and C–N stretching modes and in-plane ring deformation
1406(8)	1466(3)[31]			1487(<1)[10]	
1354(4)	1437(7)[8]	1404(1)	1404(2)	1442(5)[4]	
1344(4)					
1321(94)	1354(296)[2]	1360(100)	1360(100)	1383(518)[4]	
1302(5)	1333(6)[3]	1337(7)	1339(6)	1356(8)[26]	
	1294(2)[2]	1329(11)	1330(12)	1342(8)[23]	
1235(10)	1289(13)[3]	1290(8)	1291(9)	1329(23)[7]	
1248(15)	1291(78)[6]	1271(12)	1271(12)	1316(94)[13]	
1283(12)	1310(177)[<0.1]	1337(7)	1339(6)	1314(120)[11]	
1223(11)	1288(4)[1]	1243(2)	1243(2)	1289(11)[67]	
	1192(3)[15]			1219(<1)[16]	in-plane ring deformation
	1178(4)[5]	1170(4)		1199(<1)[2]	

1154(10)	1178(6)[6]		1169(4)	1198(9)[11]	in-plane ring deformation
	1153(<1)[14]	1140(1)	1141(1)	1173(2)[12]	
	1124(2)[<1]	1129(1)		1149(10)[1]	
	1115(<1)[1]	1109(1)	1110(2)	1131(4)[7]	
1097(6)	1120(8)[4]	1170(4)	1169(4)	1130(4)[5]	
1087(4)	1103(6)[8]	1079(1)	1079(2)	1107(3)[1]	
1064(5)	1072(4)[10]	1066(1)	1066(2)	1089(4)[3]	
1041(20)	1067(44)[<0.1]	1047(13)	1047(19)	1076(41)[1]	ring breathing mode (1+3–2)
994(98)	1013(114)[<1]	1037(73)	1037(71)	1053(216)[10]	ring breathing mode (1+2+3)
	1011(64)[2]	1030(15)	1029(sh)	1047(13)[32]	ring breathing mode (1– 3)
	1013(11)[6]	1020(4)	1020(sh)	1042(10)[<1]	out-of-plane ring deformation
	1023(1)[<0.1]			1041(<1)[2]	
	1022(<0.1)[<0.1]			1040(1)[4]	
	1016(1)[2]	1018(4)	1017(sh)	1034(4)[4]	
	990(<1)[<1]			1009(<1)[1]	
981(4)	989(<1)[<1]			1008(<0.1)[<0.1]	
	932(5)[<1]			934(<1)[<1]	
	915(<1)[<0.1]			918(<1)[<0.1]	
	913(2)[<1]			917(<1)[<1]	
	861(<0.1)[1]	842(3)	842(3)	863(8)[1]	in-plane ring deformation
832(10)	847(5)[7]	829(1)		854(1)[5]	out-of-plane ring deformation
795(5)	820(5)[10]	784(1)	785(2)	806(2)[13]	
	794(1)[62]			792(<1)[133]	
	767(<0.1)[37]			773(<1)[<1]	
	764(1)[17]			766(<1)[3]	
	762(1)[11]			755(1)[6]	
724(20)	743(16)[<1]	727(5)	727(8)	747(10)[5]	in-plane ring deformation
656(4)	677(1)[5]	669(13)	670(15)	686(8)[4]	in plane ring deformation + $\nu_s(WF_5)$
		660(35)	659(34)	677(52)[116]	$\nu_s(WF_5)$ + in plane ring deformation
640(5)	672(<1)[23]			673(<1)[26]	in-plane ring deformation
631(3)	656(5)[6]			665(<1)[18]	
620(7)	636(1)[11]	653(19)	653(17)	654(5)[15]	
615(5)	627(7)[1]			643(<1)[11]	out-of-plane deformation
		640(5)	639(3)	640(1)[140]	$\nu_{as}(WF_4)$ – ν(W–F)

			618(3)	620(1)[109]	$\nu_{as}(WF_4)$
		610(3)	608(2)	610(7)[36]	ν(W–F)
	563(<1)[4]			557(<0.1)[<0.1]	ρ ring(2)
				548(<1)[1]	$\nu_{as}(WF_4)$
	490(2)[2]			524(<1)[1]	out-of-plane deformation
	507(<1)[2]	484(1)		486(<1)[3]	
	419(1)[4]			482(<0.1)[<1]	
		473(3)	473(2)	470(5)[3]	
	417(6)[1]			450(<0.1)[2]	
		442(2)	441(2)	448(3)[<1]	
400(10)	409(5)[1]	423(1)		422(<1)[13]	
				387(<1)[10]	$\delta_{scissoring}(WF_4)$
	352(2)[<1]	371(2)	371(2)	370(2)[2]	in-plane deformation
		346(2)	346(2)	338(1)[18]	$\delta_{umbrella}(WF_4)$
				331(<1)[31]	ω(W–F)
		326(5)	324(4)	325(8)[2]	in-plane deformation
		310(2)	309(3)	316(1)[8]	δ(W–F 1+2+3–4+5)
281(7)	279(<1)[<1]	288(3)	287(5)	301(2)[<1]	out-of-plane deformation
		279(3)	279(7)	280(1)[1]	$\delta_{as}(WF_4)$
	272(1)[<1]			272(<1)[5]	ρ rings
				266(<1)[24]	ρ(W–F)
245(10)		249(8) 229(5)	248(5)	240(4)[7]	$\delta(WF_5)$
				214(<1)[<0.1]	τ(W–F 1+2+3)
		187(9)	187(9)	195(6)[3]	$\nu_{as}(WN_3)$
223(19)	223(8)[<1]			192(2)[<0.1]	τ(W-F 4+5) τ ring (2)
		159(8)	159(6)	166(2)[1]	$\nu_{as}(WN_2)$
			138(9)	143(2)[<1]	$\nu_s(WN_2)$
192(5)	140(1)[<1]			107(1)[<0.1]	twisting mode
123(16)	103(4)[<0.1]			102(1)[3]	
102(22)	93(4)[5]	113(29)	108(26)	89(4)[1]	
	59(8)[1]			86(<1)[<0.1]	
	39(<1)[3]			59(1)[<1]	
	38(18)[<1]			43(5)[3]	

[a] Recorded in ¼" FEP reactor at ambient temperature. [b] The WF_7^- $\nu_s(WF_7)$ band was observed at 705(22) with FEP bands observed at 735(5) and 385(4) cm^{-1}. [c] Anionic SbF_6^- bands were observed at 645(19), 573(3) and 280(7) {overlap} 210(12) cm^{-1} with FEP bands observed at 1380, 735 and 385 cm^{-1}. [d] Calculated at the B3LYP/aVTz level of theory. Absolute Raman intensities (in $Å^4\ u^{-1}$)) are given in parentheses and absolute IR intensities (in km mol^{-1}) are given in square brackets. [e] Symbols and abbreviations denote stretch (ν), bend (δ), rock (ρ), twist (τ), wag (ω), symmetric (s), and asymmetric (as).

The most intense C–C stretching bands (exptl. 1611/1360/1037, calcd. 1644/1383/1053 cm^{-1}) are blue-shifted with respect to those of free terpy (exptl. 1574/1321/995, calcd. 1574/1354/1013 cm^{-1}), indicating complexation. The cation bands for the $[SbF_6]^-$ salt are essentially the same as those of the $[WF_7]^-$ salt, save for a slight increase in intensity of the 1574, 1464, 1047, and 279 cm^{-1} bands, with the latter intensity increase attributable to overlap with an $[SbF_6]^-$ anion band. Meanwhile, the anionic $\nu_s(WF_7^-)$ band was observed at 705 cm^{-1} with bands attributed to the $[SbF_6]^-$ anion appearing at 645, 573, and 280 cm^{-1}. The main cationic W–F peak (exptl. $[WF_7]^-$ salt: 660, $[SbF_6]^-$ salt: 659, calcd. 677 cm^{-1}) is a composite mode consisting of a symmetric W–F stretch and an in-plane ring deformation. The frequency is consistent with the symmetric W–F stretching frequencies of other octacoordinate fluoridotungsten compounds ($WF_6(NC_5H_5)_2$: exptl. 661,[23] calcd. 673 cm^{-1}; WF_6(2,2′-bipy): exptl. 665/647, calcd. 692/661 cm^{-1}; WF_6(1,10-phen): exptl. 658, calcd. 688 cm^{-1}; $[WF_4(2,2'\text{-bipy})_2]^{2+}$: exptl. 678/645, [24] calcd. 684/650 cm^{-1}) and are significantly lower than that of free WF_6 (exptl. 771,[25] calcd. 759 cm^{-1}).

5.2.4. Multinuclear NMR Spectrometry of $[WF_5(terpy)][WF_7]$

In order to compare the complexes with the free ligand, ^1H and ^{13}C NMR spectra of terpy in acetonitrile were recorded at 22 °C. The spectra are shown in Figures 5.5 and 5.6 together with the peak assignments using the atom numbering in Figure 5.4. All values are in good agreement with those previously reported by Pazderski *et al.*[26] Starting from the most deshielded resonance, the H6/H6′′ protons *ortho* to the nitrogen atom are assigned to the resonance at 8.82 ppm ((ddd) $^3J_{H6–H5}$ = 4.76 Hz, $^4J_{H6–H4}$ = 1.86 Hz, $^5J_{H6–H3}$ = 0.92 Hz), followed by the H3/H3′′ protons at 8.77 ppm ((dt) $^3J_{H3–H4}$ = 7.49 Hz, $^4J_{H5–H3}$ and $^5J_{H6–H3}$ =

1.14 Hz). The H3′/H5′ and H4′ protons of the central ring are assigned to the doublet at 8.59 ppm ((d) $^{3}J_{H3'–H4'}$ = 7.85 Hz) and the triplet at 8.14 ppm ((t) $^{3}J_{H3'–H4'}$ = 7.82 Hz), respectively. The resonance at 8.06 ppm ((td) $^{3}J_{H3–H4}$ and $^{3}J_{H4–H5}$ = 7.73 Hz, $^{4}J_{H6–H4}$ = 1.80 Hz) is assigned to the H4/H4′′ protons and, finally, the H5/H5′′ protons appear at 7.54 ppm ((ddd) $^{3}J_{H5–H4}$ = 7.51 Hz, $^{3}J_{H6–H5}$ = 4.76 Hz, $^{4}J_{H5–H3}$ = 1.23 Hz). In the ^{13}C NMR spectrum, the quaternary C2/C2′′ and C2′/C6′ carbons are assigned to the most deshielded resonances at 154.9 and 154.5 ppm, respectively. The C6/C6′′ carbons, similar to their protic counter parts, are also deshielded and are assigned to the resonance at 148.4 ppm. Meanwhile, the carbon atoms *para* to the nitrogens, C4′ and C4/C4′′, resonate at 137.4 and 136.3 ppm, respectively. The C5/C5′′ peaks (123.2 ppm) are found to be lower in chemical shift. The C3/C3′′ and C3′/C5′ carbons appear at 119.9 ppm as one signal in the CH_3CN sample and are in agreement with the report by Pazderski *et al.*[26]

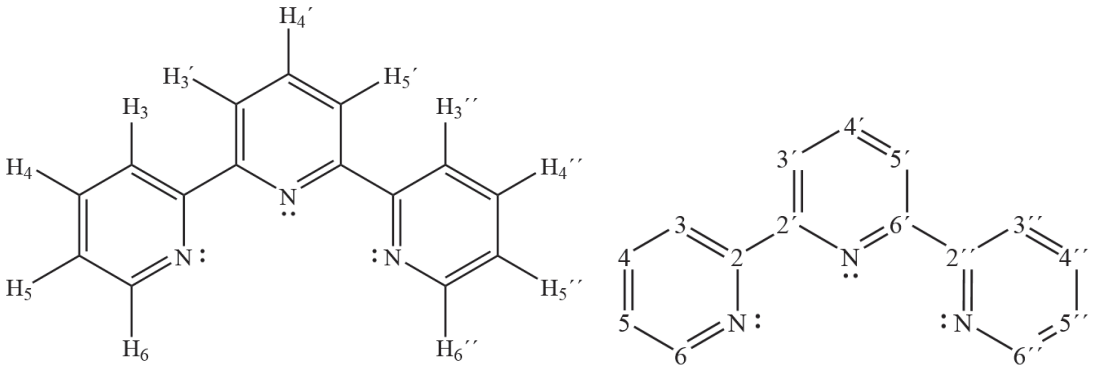

Figure 5.4. Numeric classification of protons (left) and carbons (right) for terpy.

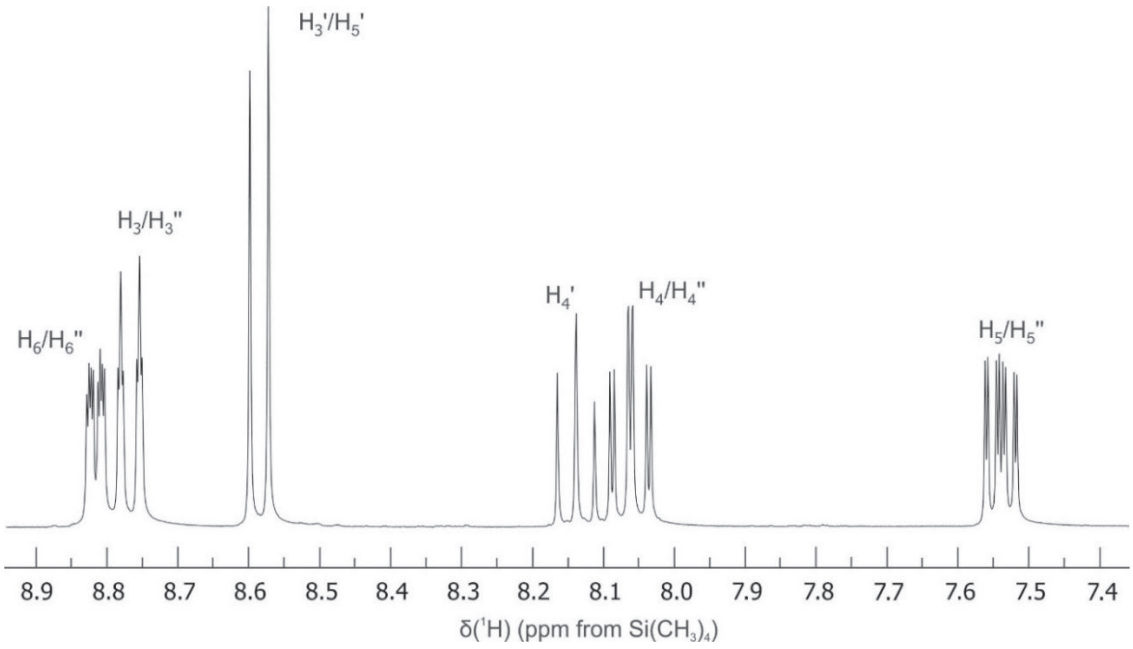

Figure 5.5. ^{1}H NMR spectrum of free terpy at 22 °C in acetonitrile.

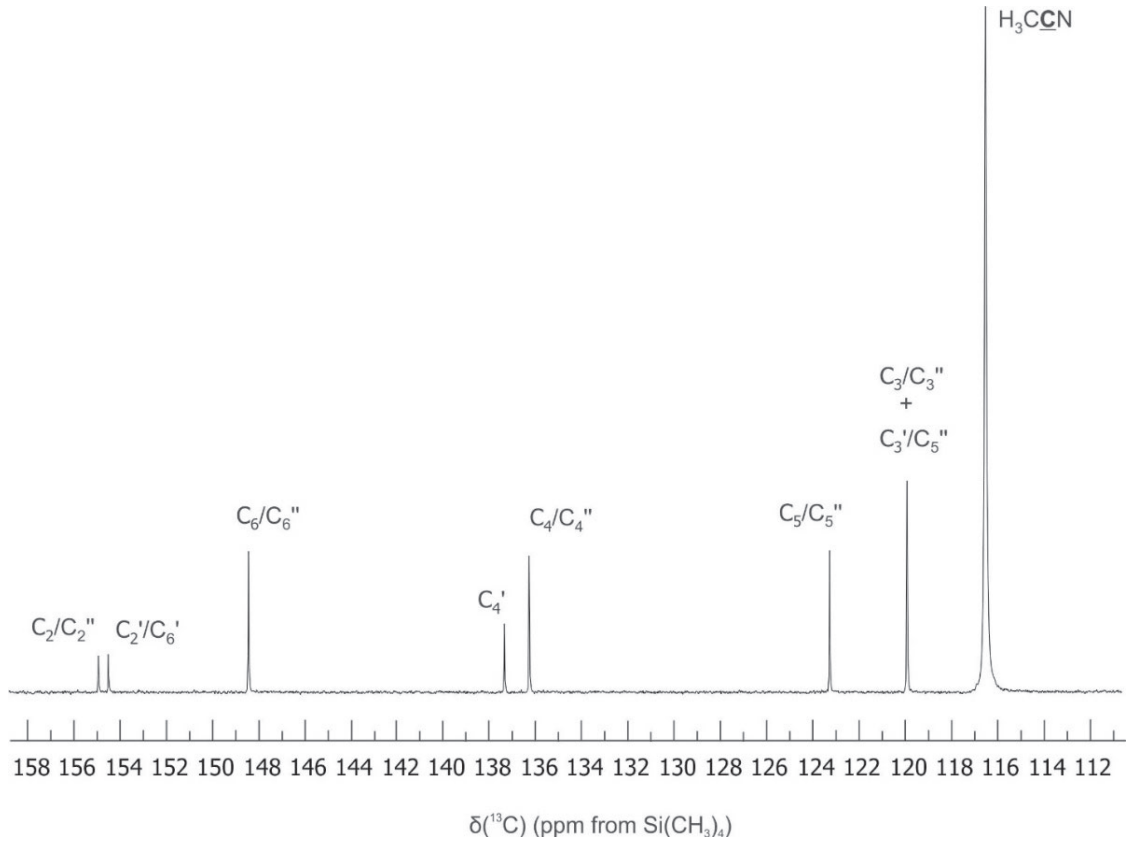

Figure 5.6. ^{13}C{^{1}H} NMR spectrum of free terpy at –35 °C in acetonitrile.

The ^{1}H and ^{19}F NMR spectra of $[WF_5(terpy)][X]$ (X = WF_7, SbF_6) were recorded in SO_2 at 22 and –60 °C (Figures 5.7-13) with the ^{13}C NMR spectra recorded at –35 °C. The ^{1}H NMR spectrum of the $[WF_7]^-$ salt at 22 °C showed resonances that are shifted to higher frequency compared to the free ligand. The H6/H6′′ protons now appear at 10.14 ppm ((d) $^{3}J_{H6–H5}$ = 5.98 Hz). The H5/H5′′ protons are now observed to be at 8.73 ppm ((td) $^{3}J_{H5–H4}$ = 8.00 Hz, $^{3}J_{H6–H5}$ = 4.28 Hz). Meanwhile, H4′ and H3′/H5′ can be assigned to the AB_2 spin system of the central ring being drastically shifted to 9.45 and 9.27 ppm, respectively ($^{3}J_{H3′/5′–H4′}$ = 7.95 Hz). Lastly, the multiplet at 9.14-9.20 ppm is attributed to the remaining H4/H4′′ and H3/H3′′ protons. Overall, the resonances for the ortho and para protons exhibit a more substantial shift to higher frequency compared to those of the meta hydrogens. The ^{13}C NMR spectra show that the para and meta carbons are deshielded upon coordination to the metal center, while the ortho carbons are more shielded (Figure 5.7). The C4′ carbon is assigned to the resonance at 156.9 ppm and has shifted dramatically compared to the free ligand mirroring the observations of the coordinated H4′ proton. The C4/C4′′ carbons are thus assigned to the resonance at 148.3 ppm and believed to be two separate unresolved signals to explain the broadness of the resonance and expected signal height with the C5/C5′′ carbons assigned to the resonance at 131.0 ppm. Meanwhile, the C3′/C5′ and C3/C3′′ carbons have now resolved into two distinct signals at 126.1 and 125.7 ppm, respectively. Interestingly, the quaternary carbons, C2′/C6′ (150.6 ppm) and C2/C2′′ (150.3 ppm) alongside the C6/C6′′ carbons (145.2 ppm) have become shielded upon adduction to the metal center.

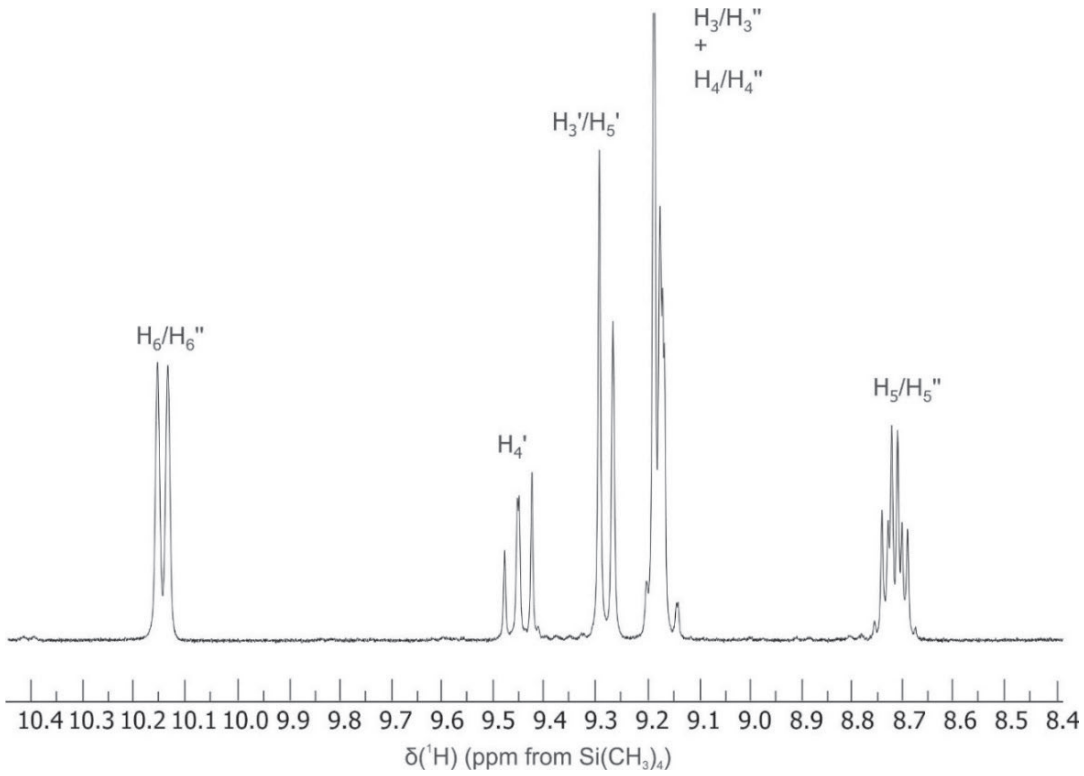

Figure 5.7. ^{1}H NMR spectrum of $[WF_5(terpy)][WF_7]$ at 22 °C in SO_2.

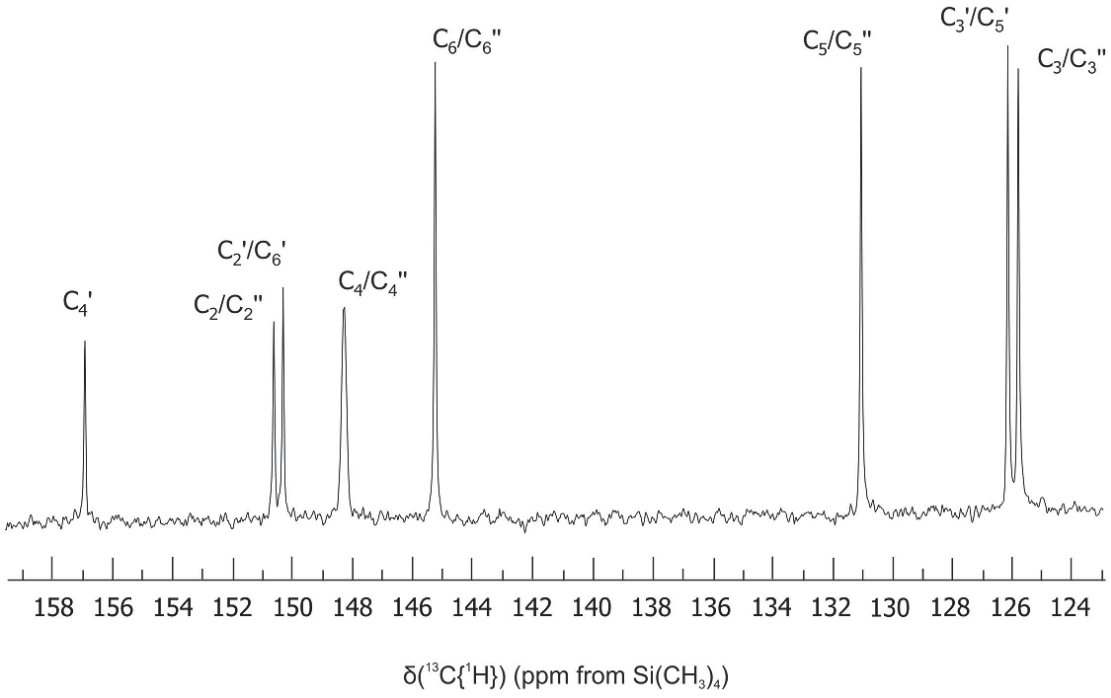

Figure 5.8. $^{13}C\{^{1}H\}$ NMR spectrum of $[WF_5(terpy)][WF_7]$ at 22 °C in SO_2.

Meanwhile, the ^{19}F NMR spectrum at 22 °C contains an intense singlet for the $[WF_7]^-$ anion at 148.6 ppm and an additional singlet at 145.3 ppm (Figure 5.9). The singlet at 145.3 ppm ($\Delta\nu_{½}$ = 11 Hz, $^1J_{W-F}$ = 21 Hz) is attributed to the rapidly exchanging fluorine environments in $[WF_5(terpy)]^+$ cation. These resonances integrate to 5 : 6.44 for $[WF_5(terpy)]^+$ to $[WF_7]^-$. The disparity between the expected ratio of 5 : 7 is believed to be a consequence of a small degree of hydrolysis resulting in trace amounts of the oxide fluoride anions $[W_2O_2F_9]^-$ ($F_{term,}$: (d) 65.6 ppm, $^2J_{F-F}$ = 58 Hz, $^1J_{W-F}$ = 70 Hz; resonance for $F_{br.}$ is not observed because of its expected low intensity) and $[WOF_5]^-$ ($F_{eq.}$: 58.6 ppm, $^2J_{F-F}$ = 52 Hz, $^1J_{W-F}$ = 71 Hz; resonance for $F_{ax.}$ is not observed because of its expected low intensity). Cooling the solution to –60 °C was insufficient to suppress the exchange of the cation fluorine environments, resulting in a shift to 138.9 ppm and a slight broadening ($\Delta\nu_{½}$ = 24 Hz), meanwhile, the $[WF_7]^-$ anion shifted to 148.9 ppm (Figure 5.10). The cationic resonance is considerably lower in frequency compared to other cationic W(VI) fluorido compounds with multidentate ligands with resonances at 204 and 206 ppm for the heptacoordinate $[WF_5(phen)]^+$ and $[WF_5(bipy)]^+$ cations, respectively.[16]

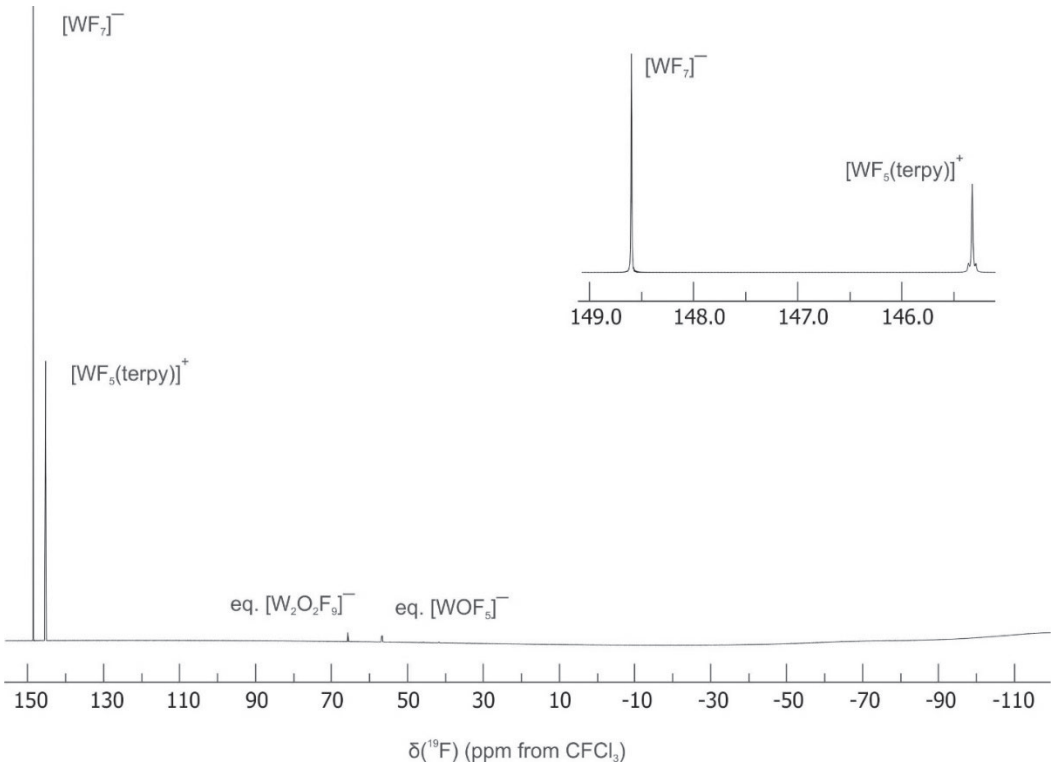

Figure 5.9. ^{19}F NMR spectrum of $[WF_5(terpy)][WF_7]$ at 22 °C in SO_2.

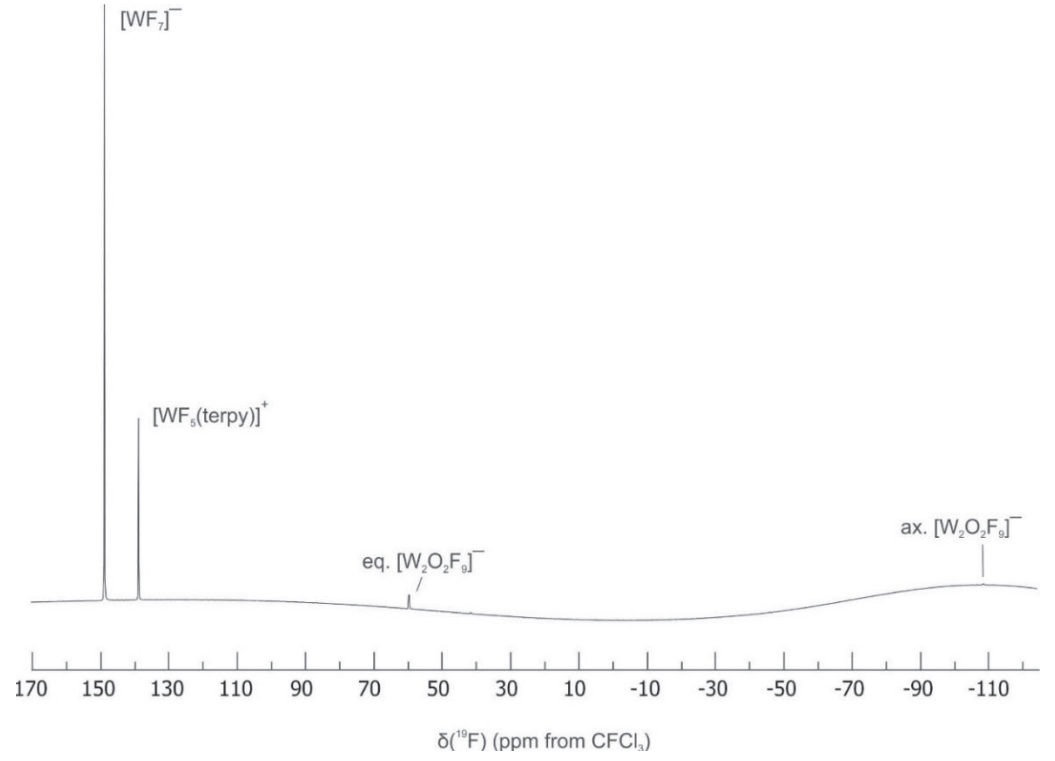

Figure 5.10. ^{19}F NMR spectrum of $[WF_5(terpy)][WF_7]$ at –60 °C in SO_2.

The ^{19}F NMR spectrum of $[WF_5(terpy)][SbF_6]$ once more shows the main cation peak at 145.6 ppm. Trace peaks of free WF_6 at 167.4 ppm ((s) $^1J_{W-F}$ = 43 Hz) presumed to be trapped in the solid from the reaction described in Eq. 2, $WOF_4(OSO)$ ((br. s) 73.6 ppm), $[W_2O_2F_9]^-$ ($F_{term.}$: 67.0 ppm (d), $^2J_{F-F}$ = 58 Hz; resonance for $F_{br.}$ is not observed because of its expected low intensity), and $[WOF_5]^-$ (F_{ax}: (br. d) 58 ppm; resonance for $F_{ax.}$ is not observed because of its expected low intensity) are present alongside two unknown trace impurities at 65.6 and 46.0 ppm. (Figure 5.11) The $[SbF_6]^-$ resonance could not be conclusively discerned from the baseline, presumably because of the usual broader nature of the fluorine resonances coupled to the quadrupolar $^{121,123}Sb$ nuclei and the distribution of intensities to the multiplet splitting of the fluorine resonance. The ^1H NMR spectrum shows slightly shifted peaks compared to the $[WF_7]^-$ analogue with the H6/H6′′ protons now appearing at 10.22 ppm ((d) 6.01 Hz), the H5/H5′′ shifting to 8.83-76 ppm (m), the H4′ proton appearing at 9.51 ppm ((dd) 8.03 Hz, 7.88 Hz), the H3′/H5′ protons now at 9.34 ppm ((d) 8.05 Hz), and the H4/H4′′ and H3/H3′′ protons forming the multiplet at 9.26-9.23 ppm. Trace impurities at 10.49 ((br. d) 6.38 Hz), 9.71 ((t) 6.35 Hz), 9.46 (s), 9.39 (s), and 8.93-8.86 (m) are present and are presumed to be $[Hterpy]^+$ believed to have formed from hydrolysis. Lastly, the ^{13}C NMR spectrum shows identical peaks to the $[WF_7]^-$ analogue: 157.0 ppm (s, C4′), 150.7 (s, C2′/C6′), 150.3 (s, C2/C2′′), 148.4 (s, C4/C4′′), 145.3 (s, C6/C6′′), 131.1 (s, C3′/C5′), 126.1(s, C3/C3′′), 125.7 (s, C5/C5′′). Trace impurities of 146.9, 127.2, 126.5, and 126.3 ppm are present and are once more presumed to be $[Hterpy]^+$ as a consequence of hydrolysis.

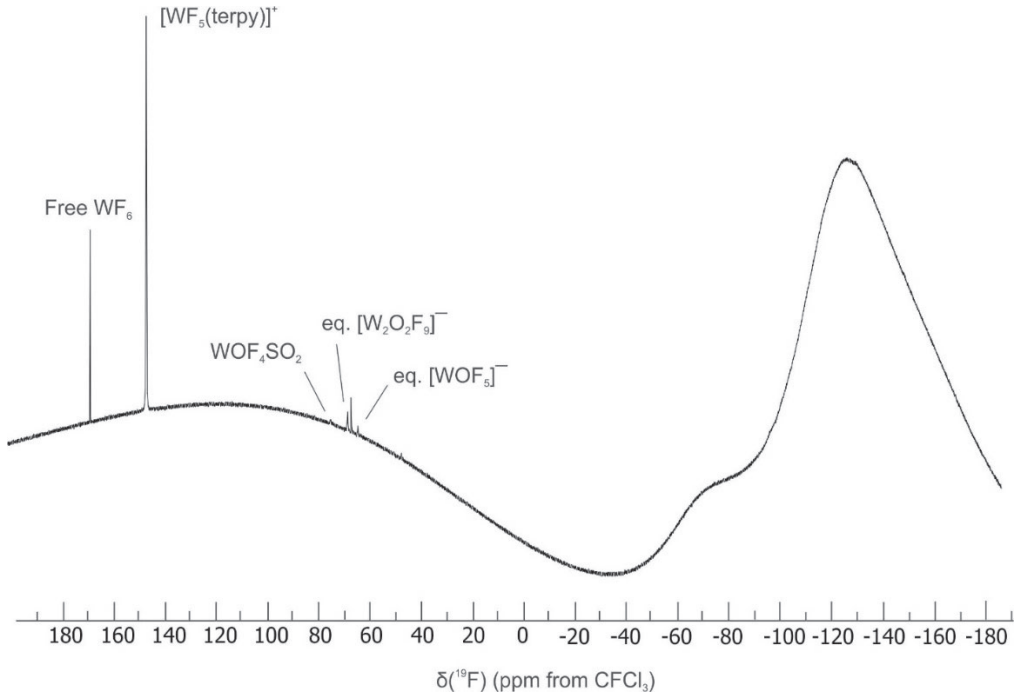

Figure 5.11. ^{19}F NMR spectrum of $[WF_5(terpy)][SbF_6]$ at 22 °C in SO_2.

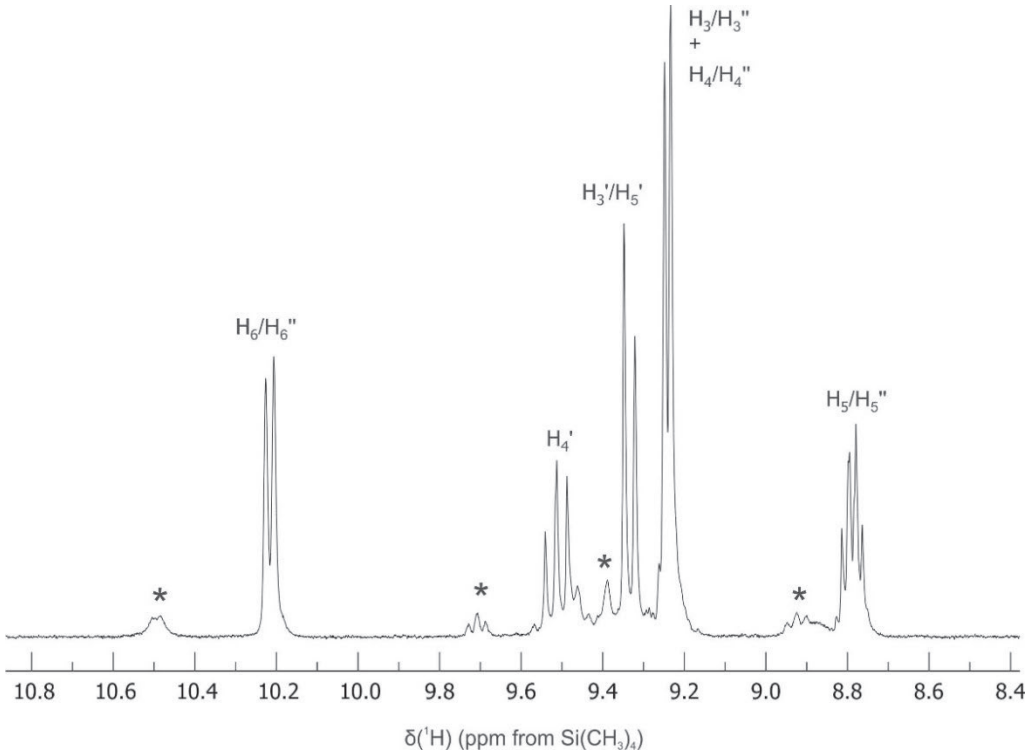

Figure 5.12. ^{1}H NMR spectrum of $[WF_5(terpy)][SbF_6]$ at 22 °C in SO_2. Asterisks (*) denote traces of $[Hterpy]^+$.

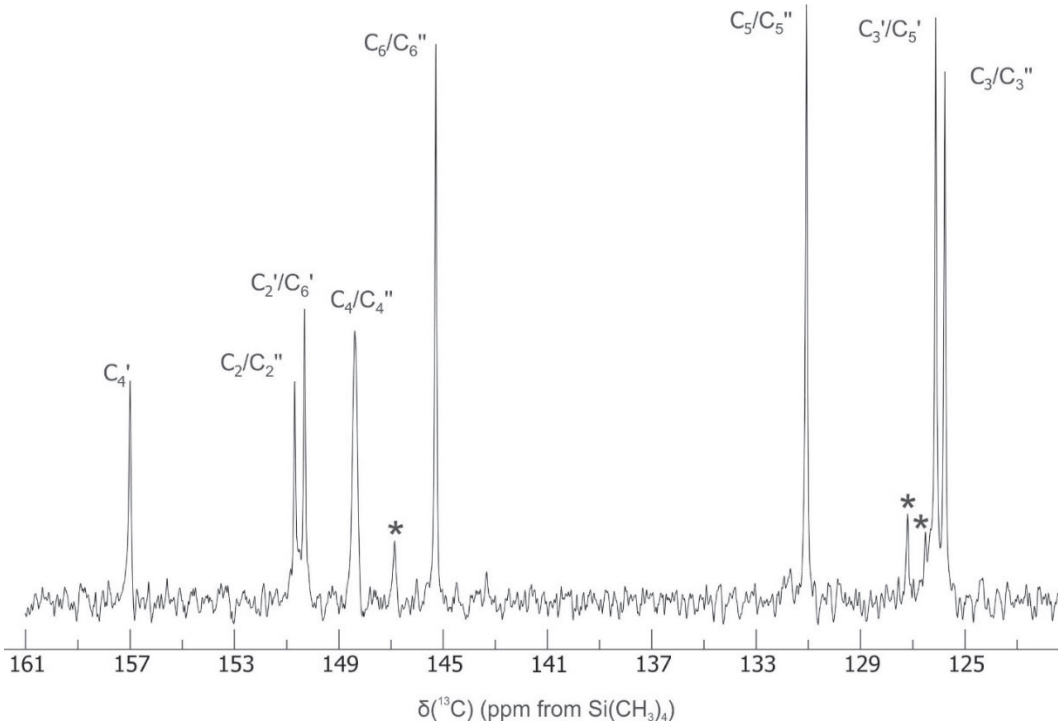

Figure 5.13. $^{13}C\{^{1}H\}$ NMR spectrum of $[WF_5(terpy)][SbF_6]$ at –35 °C in SO_2. Asterisks (*) denote traces of $[Hterpy]^+$.

The ^{19}F NMR spectrum of $2WF_6(py)$ + terpy reveals that the $[WF_5(terpy)][WF_7]$ salt is produced with resonances at 148.8 ppm assigned to $[WF_7]^-$ and 141.9 ppm assigned to $[WF_5(terpy)]^+$ (Figure 5.12). After 24 h, however, the cation was no longer observed, suggesting the formation of a tungsten (V) fluoride species or insoluble tungsten (VI) species, possibly because of the presence of pyridine, with numerous tungsten oxide fluoride resonances also appearing. An attempt to replicate the results by dissolving the $[WF_5(terpy)][WF_7]$ salt in pyridine resulted in the complete disappearance of the cation, supporting the formation of tungsten (V) fluoride or insoluble tungsten (VI) species, and produces a trace amount of $WF_6(py)_2$ (114.5 ppm) (Figure 5.13). However, it should be noted that both spectra do not represent the bulk material due to the presence of undissolved solids.

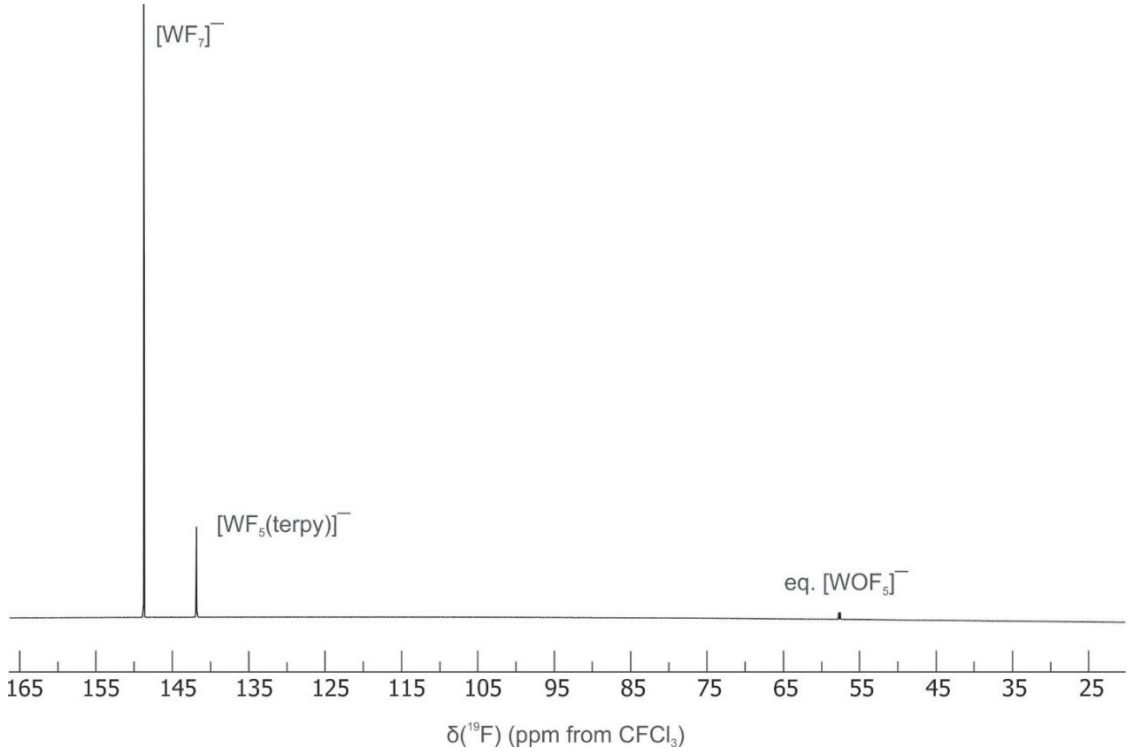

Figure 5.12. ^{19}F NMR spectrum of $2WF_6(py)$ + terpy at 22 °C in SO_2.

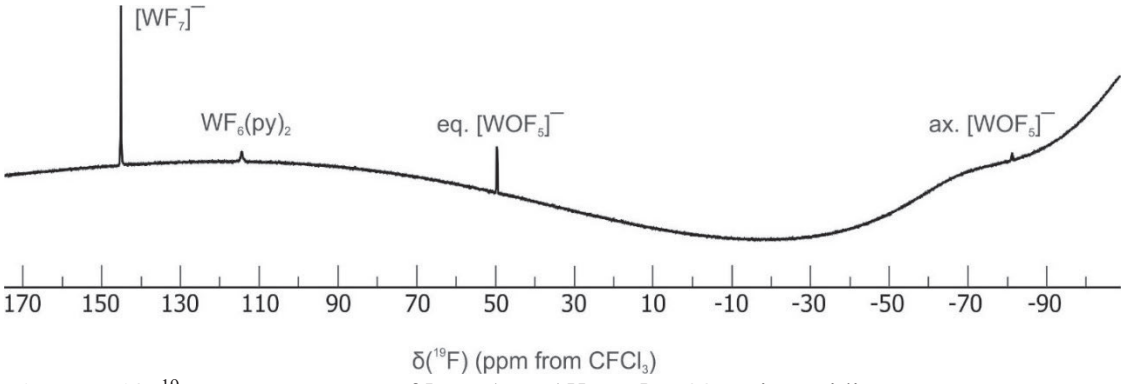

Figure 5.13. ^{19}F NMR spectrum of $[WF_5(terpy)][WF_7]$ at 22 °C in pyridine.

5.2.5. Computational Analysis

Natural-bond-order analyses were performed, providing natural-population-analysis (NPA) charges and Wiberg bond indices (WBIs) for $[WF_5(terpy)]^+$ (Table 5.5-5.6).[27] Similar to what has been seen in $[WF_5(py)_3]^+$, there is a large degree of electron

donation from the ligand, stabilizing the electron-poor metal centre with the cumulative NPA charges of the terpy ligand accounting for nearly all of the overall charge of the complex (+0.89). Indeed, further similarities with the tris(pyridine) complex were observed with both the charges on the metal centre (2.47 vs. 2.48, respectively) and average charge of the fluorine atoms (–0.47 vs –0.48) being essentially the same. However, donation is not uniform in the terpy ligand with the central nitrogen possessing a charge of –0.51 and the two other nitrogen atoms possessing a charge of –0.42. This further parallels the observed disparity between the W–N bond lengths observed within the crystal structure. The WBIs of the W–F bonds of the terpy complex (W–F: 0.73-0.76) were found to be slightly smaller than those observed in the $[WF_5(L–L)]^+$ (L–L = phen, bipy) complexes and are comparable to those in $[WF_5(py)_3]^+$. The W–N bonds are roughly ½ of the strength of those of the W–F bonds (W–N/W–F: 0.51-0.60), indicating a significant covalent contribution to the dative W–N bonding.

Table 5.5. Natural-Population-Analysis Charges and Wiberg Valences[a] of Select Cationic Fluoridotungsten(VI) Complexes[b]

	WF_6[c]	$[WF_5(terpy)]^+$	$[WF_5(phen)]^+$ [d]	$[WF_5(bipy)]^+$ [d]	$[WF_5(py)_3]^+$ [e]
W1	2.69[4.81]	2.47[5.04]	2.59[4.90]	2.59[4.90]	2.48[5.02]
F1	0.45[1.01]	–0.49[0.93]	–0.42[1.04]	–0.42[1.04]	–0.48[0.95]
F2	0.45[1.01]	–0.45[0.93]	–0.45[0.99]	–0.45[1.00]	–0.51[0.90]
F3	0.45[1.01]	–0.48[0.98]	–0.45[1.00]	–0.45[1.00]	–0.47[0.97]
F4	0.45[1.01]	–0.45[0.93]	–0.45[0.99]	–0.45[1.00]	–0.47[0.95]
F5	0.45[1.01]	–0.48[0.98]	–0.45[0.99]	–0.46[0.99]	–0.47[0.94]
F6	0.45[1.01]				
N1		–0.42[3.39]	–0.48[3.36]	–0.48[3.36]	–0.46[3.38]
N2		–0.51[3.37]	–0.48[3.36]	–0.48[3.36]	–0.46[3.38]
N3		–0.42[3.39]			–0.45[3.40]
Σ(L)[f]		0.89	0.62	0.62	0.91

[a] Given in square brackets. [b] Calculated at the B3LYP/aVTZ level of theory. Values are given for one half of the bipy and phen ligands as the two halves are related by C_s, C_2, or higher symmetry. Atom labeling for N, C is as in Figure 1 with H atoms connected to their respective carbon. [c] Ref. 28. [d] Ref. 16. [e] Ref. 18. [f] Total NPA charge of the pyridine, bipy, or phen ligands.

Table 5.6. Wiberg Bond Indices of Various Select Fluoridotungsten(VI) Complexes[a]

	WF_6[b]	$[WF_5(terpy)]^+$	$[WF_5(phen)]^+$ [c]	$[WF_5(bipy)]^+$ [c]	$[WF_5(py)_3]^+$ [d]
W–F(1)	0.80	0.73	0.83	0.82	0.73
W–F(2)	0.80	0.76	0.79	0.79	0.69
W–F(3)	0.80	0.73	0.80	0.80	0.75
W–F(4)	0.80	0.76	0.79	0.79	0.74
W–F(5)	0.80	0.73	0.79	0.79	0.75
W–F(6)	0.80	N/A	N/A	N/A	N/A
W–N(1)		0.39	0.42	0.42	0.4-0.42
W–N(2)		0.44	0.42	0.42	
W–N(3)		0.39	N/A	N/A	
N–C		1.26-1.38	1.24-1.40	1.28-1.35	1.35
C–C		1.39-1.45 (1.07)[e]	1.17-1.51	1.40-1.43 (1.06)[e]	1.44-1.45
C–H		0.90-0.91	0.90-0.91	0.90-0.91	0.91

[a] Calculated at the B3LYP/aVTZ level of theory. [b] Ref. 28. [c] Ref. 16. [d] Ref. 18. [e] C_{py}–C_{py} bonds.

5.3. Conclusion

Tungsten hexafluoride is able to form a cationic adduct with 2,2′:6′,2′′-terpyridine via fluoride abstraction. Interactions between WF_6 and tridentate ligands have been explored. The $[WF_5(terpy)][X]$ (X = WF_7, SbF_6) salts were isolated and characterized by Raman spectroscopy, showing the main stretching bands of free terpyridine shifted to a higher frequency, reflecting ligand coordination. The ^{19}F NMR spectra of the $[WF_5(terpy)][WF_7]$ salt showed a singlet at 145 ppm for the pentafluoride cation at ambient temperature and shifting to 139 ppm at –60 °C, with both chemical shifts being dramatically lower than those for other $[WF_5(L–L)]^+$ (L–L = phen, bipy) and $[WF_5(L)_3]^+$ (L = py) species. X-ray crystallography revealed that the terpy ligand is able to stabilize the electron-poor metal center compound crystallized in the $P\overline{1}$ space group and co-crystallized with 1 equiv. of SO_2. The salt was determined to adopt a bicapped trigonal prismatic geometry as verified by τ_8 geometry index calculations. The terpy ligand was determined to possess two distinct W–N bond lengths due to the capping bond lengths being longer than the one from the central pyridine ring, and also longer than those of other N-donor stabilized fluorido tungsten cations, *i.e.*, $[WF_5(L)]^+$ (L = phen, bipy) and $[WF_5(L')_3]^+$ (L' = py). Additionally,

the average W–F bond length was found to be larger than in other $[WF_5(L)]^+$ (L = phen, bipy) and $[WF_5(L')_3]+$ (L' = py) species, rivaling that of $WF_6(py)_2$. NBO analysis revealed that the terpy ligand accounts for most of the overall charge of the complex with the central nitrogen atom donating significantly more electron density. $WF_6(py)$ was explored as an alternative pathway to obtain the salt. While a trace amount of the cation was observed to form, after a day, the cation was no longer observed suggesting a conversion to a tungsten(V) species or insoluble tungsten(VI) species. The salt was also dissolved in pyridine and was observed to have an analogous ^{19}F spectrum, with a new resonance attributed to $WF_6(py)_2$ being formed.

5.4 References

1. Molski, M. J.; Seppelt, K. The Transition Metal Hexafluorides. *Dalton Trans.* **2009**, *18*, 3379–3383. DOI: 10.1039/b821121c

2. Lee, C.Y.; Yang, W.C. Study of chemical vapor deposition reaction between tungsten hexafluoride and silicon difluoride. *J. Mater. Chem.* **1999**, *9* (10)**,** 2445-2448. DOI: 10.1039/A906054E

3. Skaf, D.W.; Warner, A.W.; Dollahan, N.R.; Fargo, G.H. Microstructure and Properties of CVD Tungsten Carbide from Tungsten Hexafluoride and Dimethyl Ether. *Mater. Charact.*, **1994**, *33* (4), 393-402. DOI: 10.1016/1044-5803(94)90144-9.

4. Karimi, H.; Hadi, M. Effect of Sintering Techniques on the Structure and Dry Sliding Wear Behavior of WC-FeAl Composite. *Ceram. Int.* **2020**, *46* (11) part B, 18487-18497. DOI: 10.1016/j.ceramint.2020.04.154

5. Ammunition. https://www.britannica.com/technology/ammunition#ref260499 (accessed 2024-05-15).

6. Furberg, A.; Arvidsson, R.; Molander, S. Dissipation of Tungsten and Environmental Release of Nanoparticles from Tire Studs: A Swedish Case Study. *J. Cleaner Prod.* **2019**, *207* (10), 920-928. DOI: 10.1016/j.jclepro.2018.10.004

7. Moser, A.; Exadaktylos, A.; Radke, A. Removal of a Tungsten Carbide Ring from the Finger of a Pregnant Patient: A Case Report Involving 2 Emergency Departments and the Internet. *Emerg. Med. Case Rep.* **2016,** *2106*, 8164524. DOI: 10.1155/2016/8164524

8. Giese, S.; Seppelt, K. Structural Principles in Seven-Coordinate Subgroup Compounds: The Complex Anions MoF_7^-, WF_7^-, and $ReOF_6^-$. *Angew. Chem. Int. Ed. Engl.* **1994**, *33* (4), 461–463. DOI:10.1002/anie.199404611.

9. Adam, S.; Ellern, A.; Seppelt, K. Structural Principles of the Coordination Number Eight: WF_8^{2-}, ReF_8^{2-}, and XeF_8^{2-}. *Chem. Eur. J.* **1996**, *2* (4), 398–402, DOI: 10.1002/chem.19960020408

10. Blondel, C.; Cacciani, P.; Delsart, C.; Trainham, R. High-Resolution Determination of the Electron Affinity of Fluorine and Bromine Using Crossed Ion and Laser Beams. *Phys. Rev. A.* **1989**, *40* (7), 3698– 3701. DOI: 10.1103/PhysRevA.40.3698

11. Craciun, R.; Long, R. T.; Dixon, D. A.; Christe, K. O. Electron Affinities, Fluoride Affinities, and Heats of Formation of the Second Row Transition Metal Hexafluorides: MF_6 (M = Mo, Tc, Ru, Rh, Pd, Ag). *J. Phys. Chem. A.*, **2010,** *114* (28), 7571–7582. DOI: 10.1021/jp1022949

12. Craciun, R.; Picone, D.; Long, R. T.; Li, S.; Dixon, D. A.; Peterson, K. A.; Christe, K. O. Third Row Transition Metal Hexafluorides, Extraordinary Oxidizers, and Lewis Acids: Electron Affinities, Fluoride Affinities, and Heats of Formation of WF_6, ReF_6, OsF_6, IrF_6, PtF_6, and AuF_6. *Inorg. Chem.* **2010**, *49* (3), 1056–1070. DOI: 10.1021/ic901967h

13. Bartlett, N. The Oxidizing Properties of the Third Transition Series Hexafluorides and Related Compounds. *Angew. Chem. Int. Ed. Engl.* **1968**, *7* (6), 433–439. DOI: 10.1002/anie.196804331

14. Arnaudet, L.; Bougon, R.; Ban, B.; Lance, M.; Navaza, A.; Nierlich, M.; Vigner, J. 2,2'-Bipyridine Fluoro Complexes of Tungsten(VI): Preparation, Characterization and Crystal Structure of $[WF_4(bipy)_2]^{2+} \bullet 2[WF_7]^- \bullet WF_6$ and $[WF_4(bipy)_2]^{2+} \bullet 2[WF_7]^- \bullet CH_3CN$; Preparation and Characterization of WF_6 bipy. *J. Fluorine Chem.* **1994**, *67* (1), 17-25. DOI: 10.1016/0022-1139(93)02926-6

15. Levason, W.; Monzittu, F. M.; Reid, G.; Zhang, W. Neutral and Cationic Tungsten(VI) Fluoride Complexes with Tertiary Phosphine and Arsine Coordination, *Chem. Commun.* **2018**, *54* (83), 11681–11684. DOI: 10.1039/C8CC05598J

16. Turnbull, D.; Wetmore, S. D., Gerken, M. Stabilization of $[WF_5]^+$ by Bidentate N-Donor Ligands. *Angew. Chem.* **2019**, *58* (37), 13169-13172. DOI: 10.1002/ange.201906600

17. Arnaudet, L.; Bougon, R.; Buu, B.; Lance, M.; Nierlich, M.; Thuéry, P.; Vigner, J. Characterization of the Adducts WF_6•py and WF_6•2py (py = pyridine): Crystal Structure of WF_6•2py. *J. Fluorine Chem.* **1995**, *71* (1), 123–129. DOI: 10.1016/0022-1139(94)03160-2

18. Turnbull, D.; Hazendonk, P.; Wetmore, S. D.; Gerken, M. Stabilisation of $[WF_5]^+$ and WF_4 by Pyridine: Facile Access to $[WF_5(NC_5H_5)_3]^+$ and $WF_5(NC_5H_5)_2$. *Chem. - Eur. J.* **2020**, *26* (30), 6879-6886. DOI: 10.1002/chem.202000424

19. Turnbull, D.; Wetmore, S. D.; Gerken, M. Stabilisation of $[W^VF_4]^+$ by N- and P-Donor Ligands: Second-Order Jahn-Teller Effects in Octacoordinate d^1 Complexes. *Chem. - Eur. J.* **2021**, *27* (44), 11335-11343. DOI: 10.1002/chem.202100863

20. Wang, M.; Weyhermüller, T.; England, J.; Weighardt, K. Molecular and Electronic Structures of Six-Coordinate "Low-Valent" $[M(Mebpy)_3]^0$ (M = Ti, V, Cr, Mo) and $[M(tpy)_2]^0$ (M = Ti, V, Cr), and Seven-Coordinate $[MoF(Mebpy)_3](PF_6)$ and $[MX(tpy)_2](PF_6)$ (M = Mo, X = Cl and M = W, X = F). *Inorg. Chem.* **2013**, *52* (21), 12763-12776. DOI: 10.1021/ic402

21. Bondi, A. van der Waals Volumes and Radii *J. Phys. Chem.* **1964**, *68* (3), 441–451 DOI: 10.1021/j100785a001

22. Turnbull, D.; Kostiuk, N.; Wetmore, S. D.; Gerken, M. Syntheses, Characterization, and Computational Studies of Tungsten Hexafluoride Adducts with Pyridine and Its Derivatives. J. Fluorine Chem. 2018, 215, 1–9. DOI: 10.1016/j.jfluchem.2018.08.007
23. Arnaudet, L.; Bougon, R.; Buu, B.; Lance, M.; Nierlich, M.; Thuéry, P.; Vigner, J. Characterization of the adducts WF_6•py and WF_6•2py (py = pyridine): crystal structure of WF_6•2py. *J. Fluorine Chem.* **1995**, *71* (1), 123–129. DOI: 10.1016/0022-1139(94)03160-2

24. Arnaudet, L.; Bougon, R.; Ban, B.; Lance, M.; Navaza, A.; Nierlich, M.; Vigner, J. 2,2'-Bipyridine Fluoro Complexes of Tungsten(VI): Preparation, Characterization and Crystal Structure of $[WF_4(bipy)_2]^{2+}$ • $2[WF_7]^-$ • WF_6 and $[WF_4(bipy)_2]^{2+}$ • $2[WF_7]^-$ • CH_3CN; Preparation and Characterization of WF_6 bipy. *J. Fluorine Chem.* **1994**, *67* (1), 17-25. DOI: 10.1016/0022-1139(93)02926-6

25. Claassen, H. H.; Selig, H. Raman Spectra of 5d Transition Metal Hexafluorides in the Vapor State. *Isr. J. Chem.* **1969**, *7* (4), 499–504. DOI: 10.1002/ijch.196900066

26. Pazderski, L.; Pawlak, T.; Sitkowski, J.; Kozerski, L.; Szlyk, E. *Magn. Reson. Chem.* **2011**, *49*, 237–241

27. O'Donnell, F. Unpublished Work.

28. Turnbull, Lewis-Acid Behaviour of Neutral and Cationic Fluoridotungsten(V) and (VI) Complexes, Ph.D. Thesis, University of Lethbridge, Lethbridge, AB, **2020**.

Chapter 6 – Conclusions and Future Work

6.1 Conclusions

The Lewis-acid behavior of WF_6 was investigated and expanded to mixed ligand systems, phosphine oxides, and tridentate ligands, showing different reactivities ranging from ligand scrambling, deoxofluorination and ligand-induced autoionization.

Exploration of neutral WF_6 adducted with two different types of Lewis bases was explored using both pyridine and trimethylphosphine in order to assess whether the presence of two different ligands will distort the usually observed bicapped trigonal prism geometry. The crystal structure of $WF_6(py)\{P(CH_3)_3\}$ was obtained, showing that the bicapped trigonal prismatic geometry seen in both $WF_6(py)_2$ and $WF_6\{P(CH_3)_3\}_2$ was retained, and allowing for comparisons of both the W–F bond lengths and B–W–B bond angles. The adduct itself, however, could not be isolated as a pure compound as multinuclear NMR spectroscopy at both ambient and low temperatures indicates the presence of side reactions alongside the formation of $WF_6(py)\{P(CH_3)_3\}$. Nevertheless, based on DFT calculations, most of the Raman bands of the isolated solid could be correlated to the predicted vibrational bands of the mixed adduct. Additionally, DFT studies further revealed that while pyridine is a stronger base, the trimethylphosphine ligand is capable of forming a more covalent dative bond, thus allowing for more electron density to be donated to the metal center.

In Chapter 4, the reactivity of WF_6 towards phosphine oxides was investigated utilizing $OP(C_2H_5)_3$ and $OP(C_6H_5)_3$ as ligands. Instead of the targeted Lewis acid-base adduct, deoxofluorination of the phosphine oxides was observed at ambient and low

temperatures yielding F_2PR_3 and $[FPR_3]^+$ as well as WOF_4. The latter product captures the unreacted phosphine oxide ligand to form WOF_4OPR_3 or accepts a fluoride to form fluorido oxido tungstenate anions. Maintaining the reaction at –80 °C was unsuccessful at preventing deoxofluorination based on observations by multinuclear NMR spectroscopy. In the reaction of WF_6 with $OP(C_2H_5)_3$ at –80 °C, evidence for the new 1 : 2 adduct $WOF_4\{OP(C_2H_5)_3\}_2$ was obtained by ^{19}F NMR spectroscopy. This proposed adduct would only be the first 1 : 2 adduct of WOF_4 with O-donors, with the analogous adducts with pyridine-based ligands forming the precedence.

Finally, the ability of WF_6 to undergo ligand-induced autoionization was exploited to generate the first octa-coordinate $[WF_5]^+$ species stabilized by a neutral tridentate ligand. The reaction of 2,2′:6′,2′′-terpyridine (terpy) with 2 equivalents of WF_6 was shown to form $[WF_5(terpy)][WF_7]$, with the anion capable of being displaced by $[SbF_6]^-$. X-ray crystallography analysis of $[WF_5(terpy)][WF_7]\bullet SO_2$ revealed a bicapped trigonal prismatic geometry as verified by τ_8 geometry index calculations. The nitrogen atoms of the outer rings of the terpy ligand are capping the trigonal prism, while the central nitrogen forms one of the vertices of the prism. This geometry is in contrast with the structure of other octacoordinated ligand-stabilized fluorido tungsten(VI) cations, *i.e.*, $[WF_4(bipy)_2]^{2+}$ (trigonal dodecahedron), $[WF_5(bipy)]^+$ (monocapped octahedron or 3 : 4 polyhedron). The average W–F bond lengths were found to be larger than other $[WF_5(L)]^+$ (L = phen, bipy) and $[WF_5(L')_3]$+ (L' = py) species as were the capping W–N bond lengths. The ^{19}F NMR spectrum revealed that the resonance of the cation is much lower in frequency than other $[WF_5(L–L)]^+$ (L–L = phen, bipy) and $[WF_5(L)_3]^+$ (L = py) species. Meanwhile, ^1H and ^{13}C NMR spectroscopy showed higher chemical shifts compared to the free ligand and reveal

that the C4' and H4' atoms of bound terpy shifting drastically compared to the other resonances. NBO analysis revealed that the central nitrogen atom donates significantly more electron density than the capping nitrogens and that the ligand accounts for most of the overall charge of the complex.

6.2. Future Work

The formation of $[WF_5(terpy)][X]$ ($X = WF_7$, SbF_6) salts open the door for further exploration of both tridentate and higher-denticity ligands. Further exploration of tridentate ligands could be investigated with 1,4,7-trimethyl-1,4,7-triazacyclononane (Me_3TACN) (Figure 6.1), which has previously been adducted to tungsten oxide fluorides or complexes with tungsten in both low and high oxidation states.[1] Successful coordination would result in the first tungsten(VI) fluoride complex with an aza-crown ether. The salt would be of considerable interest due to the potential impact of the rigid cyclic ligand on the coordination geometry as well as the reactivity of the complex. Utilizing two equivalents of WF_6, as was done with terpy, could allow for fluoride abstraction/autoionization to take place to generate the desired salt (Eq. 6.1). Additionally, exploration of tetradentate ligands could be investigated with the use of 2,2′:6′,2′′:6′′,2′′′-quaterpyridine (qupy). Stabilization of the dication may indeed be possible due to the increased donation of the electron density of the quaterpyridine ligand (Eq. 6.2). However, additional fluoride abstraction was not observed when an additional equivalent of WF_6 was used in the synthesis of $[WF_5(terpy)][WF_7]$. Thus, a stronger fluoride abstracting agent such as trimethylsilyl triflate may need to be employed to abstract additional fluorides.

$$2WF_6 + Me_3TACN \rightarrow [WF_5(Me_3TACN)][WF_7] \qquad \text{(Eq. 6.1)}$$

$3WF_6 + qupy \rightarrow [WF_4(qupy)][WF_7]_2$ (Eq. 6.2)

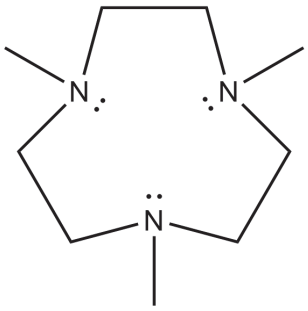

Figure 6.1. Lewis structure of 1,4,7-trimethyl-1,4,7-triazacyclononane (Me_3TACN).

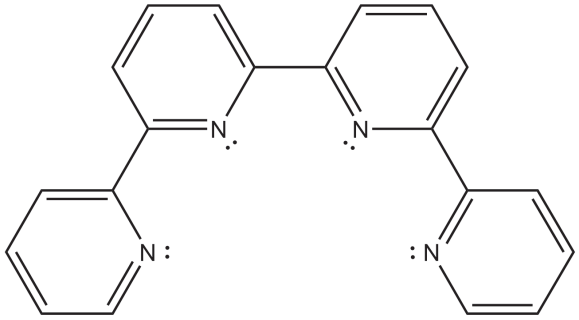

Figure 6.2. Lewis structure of 2,2′:6′,2′′:6′′,2′′′-quaterpyridine (qupy).

Based on the proposed formation of $WOF_4\{OP(C_2H_5)_3\}_2$ as evidenced by multinuclear NMR spectroscopy, this 1 : 2 adduct should be isolated and fully characterized by Raman and NMR spectroscopy, as well as X-ray crystallography. This can be achieved by first synthesizing $WOF_4\{OP(C_2H_5)_3\}$ utilizing a method similar to Levason *et al.,* then by adding an equimolar amount of $OP(C_2H_5)_3$ (Eq. 6.3-4).[(2)] Should the quantitative formation of the 1 : 2 adduct fail, excess $OP(C_2H_5)_3$ can be employed in an attempt to push

the equilibrium to favor the bis-adduct. Should this be successful, synthesis of $WOF_4\{OP(C_6H_5)_3\}_2$ could then be explored, prepared in the manners explained above.

$$WOF4(NCCH3) + OP(C_2H_5)_3 \rightarrow WOF_4\{OP(C_2H_5)_3\} \quad \text{(Eq. 6.3)}$$

$$WOF_4\{OP(C_2H_5)_3\} + XOP(C_2H_5)_3 \rightarrow WOF_4\{OP(C_2H_5)_3\}_2 \quad (X = 1, \text{excess}) \text{(Eq.6.4)}$$

Finally, Schrobilgen *et al.* were able to identify $(WOF_4)_nFXeF$ (n = 1-3) via NMR spectroscopy at lower temperatures with the crystal structure of $(WOF_4)_2FXeF$ being obtained in 2021.[3-4] This presents the possibility that other $(WOF_4)_nL$ species can exist at low temperatures, with their crystal structure possibly being elucidated. To test this hypothesis, 2 equivalents of WOF_4 would be reacted with 1 equivalent of $OP(C_2H_5)_3$ in CH_2Cl_2 solvent to generate $(WOF_4)_2\{OP(C_2H_5)_3\}$ (Eq. 6.5), with an alternative route being to react WOF_4 with $WOF_4\{OP(C_2H_5)_3\}$. The use of unadducted WOF_4 is essential as the acetonitrile employed in the synthesis of $WOF_4(NCCH_3)$ is not predicted to be displaced in these reactions. Should the synthesis of $(WOF_4)_2\{OP(C_2H_5)_3\}$ be achieved, further expansion on the $(WOF_4)_nL$ series could conducted with $OS(CH_3)_2$ to explore other oxygen-based donors, pyridine and acetonitrile for nitrogen bases, $P(CH_3)_3$ for phosphorus, and other phosphine oxides as possible avenues.[2,5]

$$4WOF_4 + 2OP(C_2H_5)_3 \rightarrow 2(WOF_4)_2\{OP(C_2H_5)_3\} \quad \text{(Eq.6.5)}$$

$$4WOF_4 + 4WOF_4\{OP(C_2H_5)_3\} \rightarrow 4(WOF_4)_2\{OP(C_2H_5)_3\} \quad \text{(Eq.6.6)}$$

6.3. References

1. Backes-Dahmann, G.; Wieghardt, K. Monomeric Complexes of Tungsten (0-VI) Containing the Ligand N,N',N"-Trimethyl-1,4,7-Triazacyclononane and Their Electrochemical Properties. Preparation of $[L_2W_2O_5](PF_6)_2$ and Identification of Its Mixed-Valence Tungsten (VI)/Tungsten(v) Complex. *Inorg. Chem.*, **1985**, *24*, 4049–4054. DOI: 10.1021/ic00218a019.

2. Levason, W.; Reid, G.; Zhang, W. Coordination Complexes of the Tungsten(VI) Oxide Fluorides WOF_4 and WO_2F_2 with Neutral Oxygen- and Nitrogen-donor Ligands. *J. Fluorine Chem.* **2016**, *184*, 50–57. DOI: 10.1016/j.jfluchem.2016.02.003

3. Holloway, J. H.; Schrobilgen, G. Fluorine-19 and Xenon-129 NMR Studies of the XeF_2•nWOF_4 and XeF_2•$MoOF_4$ (n = 1-4) Adducts: Examples of Nonlabile Xenon-Fluorine-Metal Bridges in Solution. *J. Inorg. Chem.* **1980**, *19* (9), 2632–2640. DOI: 10.1021/ic50211a031

4. Schneider, L. N.; Krauel, E.-V. T, Deutsch, C.; Urbahns, K.; Bischof, T.; Maibom, K. A. M., Landmann, J.; Keppner, F.; Kerpen, C.; Hailmann, M.; Zapf, L.; Knuplez, T.; Bertermann, R.; Ignat'ev, N. V., Finze, M. *Chem. Eur. J.* **2021**, *27*, 10973–10978.

5. Arnaudet, L.; Bougon, R.; Ban, B.; Charpin, P.; Isabey, J.; Lance, M.; Nierlich, M.; Vigner, J. Preparation, Characterization, and Crystal Structure of the Adducts WOF_4•nC_5H_5N (n = 1, 2). *Inorg. Chem.* **1989**, *28* (2), 257–262. DOI: 10.1021/ic00301a020.